ÇUKUROVA UNIVERSITY
INSTITUTE OF NATURAL AND APPLIED SCIENCES

PhD. THESIS

Hüseyin TOPAKLI

SUSY SEARCH AT CMS IN MET PLUS JETS TOPOLOGIES AT $\sqrt{s}$=14 TeV AND RESPONSE COMPARISON OF THE CMS CALORIMETERS TO PIONS BETWEEN MONTE CARLO AND TEST BEAM

DEPARTMENT OF PHYSICS

ADANA, 2010

ÇUKUROVA UNIVERSITY

INSTITUTE OF NATURAL AND APPLIED SCIENCES

SUSY SEARCH AT CMS IN MET PLUS JETS TOPOLOGIES AT $\sqrt{s}$=14 TeV AND RESPONSE COMPARISON OF THE CMS CALORIMETERS TO PIONS BETWEEN MONTE CARLO AND TEST BEAM

Hüseyin TOPAKLI

PhD THESIS

DEPARTMENT OF PHYSICS

We certify that the thesis titled above was reviewed and approved for the award of degree of the Doctor of Philosophy by the board of jury on 25/02/2010.

.....	.....	.....
Prof.Dr. Ayşe POLATÖZ	Prof.Dr. Gülsen ÖNENGÜT	Prof.Dr. Eda EŞKUT
SUPERVISOR	MEMBER	MEMBER
.....	.....	
Assoc.Prof.Dr. Ali HAVARE	Assoc.Prof.Dr. Mustafa TOPAKSU	
MEMBER	MEMBER	

This PhD Thesis is performed in Department of Physics of Institute of Natural and Applied Sciences of Cukurova University
Registration Number:

Prof.Dr. İlhami YEĞİNGİL
Director
Institute of Basic and Applied Sciences

Not: The usage of the presented specific declarations, tables, figures and photographs either in this thesis or in any other reference without citation is subject to "The Law of Arts and Intellectual Products" numbered 5846 of Turkish Republic.

ABSTRACT

PhD. THESIS

SUSY SEARCH AT CMS IN MET PLUS JETS TOPOLOGIES AT $\sqrt{s}$=14 TeV AND RESPONSE COMPARISON OF THE CMS CALORIMETERS TO PIONS BETWEEN MONTE CARLO AND TEST BEAM

Hüseyin TOPAKLI

ÇUKUROVA UNIVERSITY
INSTITUTE OF NATURAL AND APPLIED SCIENCES
DEPARTMENT OF PHYSICS

Supervisor :Prof.Dr. Ayşe POLATÖZ
Year: 2010, Pages: 97
Jury :Prof.Dr. Ayşe POLATÖZ
:Prof.Dr. Gülsen ÖNENGÜT
:Prof.Dr. Eda EŞKUT
:Assoc.Prof.Dr. Ali HAVARE
:Assoc.Prof.Dr. Mustafa TOPAKSU

Standard Model (SM) of Particle Physics has some shortcomings. Supersymmetry, (SUSY) is one of the newest and robust models to overcome shortcomings of the SM. SUSY which introduces a super partner to each of the SM particles explains problems of SM. However, these super partner particles have not been detected yet by the particle detectors in the experiments. Therefore, SUSY must be a broken symmetry and it needs to be tested by the experiments. Compact Muon Solenoid (CMS) experiment of the Large Hadron Collider (LHC) will try to detect the SUSY particles that might be seen in high energy scale such as 1 TeV or more. In this thesis, one of the SUSY search channels, multijets plus missing transverse energy (MET) is explained. Multijets are generated at the end of the hadronic decays and MET is coming from particles which are very weakly interacting with the detector materials such as neutrino and muon. While testing the SUSY theory, we must have enough information about the detector behavior in order to distinguish the signal sources. To understand the detector response, Test Beam (TB) of 2006 results and Monte Carlo studies were compared. ECAL plus HCAL calorimeter energy responses were compared to single particles between Monte-Carlo (MC) and TB. Single pion particles were used for this study in different beam energy ranges for TB and MC.

Key Words: SM, SUSY, CMS, ECAL, HCAL

ÖZ

DOKTORA TEZİ

$\sqrt{s}$ = 14 TeV'DE CMS'DE KAYIP ENERJİ VE JETLER TOPOLOJİSİNDE SÜSİ ARAŞTIRMASI VE CMS KALORİMETRELERİNİN PİONLARA YANITININ MONTE CARLO VE DEMET TESTİ İLE KIYASLANMASI

Hüseyin TOPAKLI

ÇUKUROVA ÜNİVERSİTESİ
FEN BİLİMLERİ ENSTİTÜSÜ
FİZİK ANABİLİM DALI

Danışman : Prof.Dr. Ayşe POLATÖZ
Yıl: 2010, Sayfa: 97
Jüri : Prof.Dr. Ayşe POLATÖZ
:Prof.Dr. Gülsen ÖNENGÜT
:Prof.Dr. Eda EŞKUT
:Doç.Dr. Ali HAVARE
:Doç.Dr. Mustafa TOPAKSU

Parçacık Fiziğinin Standard Model'inde (SM) bazı eksiklikler vardır. Süpersimetri (SÜSİ) en yeni ve güvenilir modellerden biri olup, SM'nin eksikliklerinin üstesinden gelmektedir. SÜSİ, SM'deki her parçacığa bir süper eş atayarak SM'nin problemlerini açıklamaktadır. Bununla birlikte, bu süper eş parçacıklar deneylerdeki parçacık detektörlerinde henüz varlanamamışlardır. Bu nedenle SÜSİ kırılmış bir simetri olmalıdır ve deneyler tarafından test edilmelidir. Sıkıştırılmış Müon Solenoid (CMS) deneyi Büyük Hadron Çarpıştırıcı (BHÇ) deneylerinden biri olup SÜSİ parçacıklarını varlamaya çalışacaktır ki bu parçacıklar yüksek enerji ölçeklerinde 1 TeV veya daha yüksek enerjilerde görünebilirler. Bu tezde SÜSİ araştırma kanallarından biri olan çoklu-jet ve kayıp enine enerjili (MET) durumları çalışılmıştır. Çoklu jetler hadronik bozunumlar sonucunda oluşurlar ve kayıp enine enerji de detektörle çok zayıf etkileşen müon, nötrino gibi parçacıklardan dolayı oluşur. SÜSİ teorisini test ederken sinyal ile fon etkisini ayırt edebilmek için detektörün davranışı hakkında yeterince bilgi sahibi olmalıyız. Detektör tepkisini anlamak icin test hüzmesi ile benzeşimden elde edilen sonuçlar karşılaştırılmıştır. Elektromanyetik ve hadronik kalorimetrelerinin tekli pionlara enerji tepkileri, test hüzmesinden ve benzeşimden elde edilen sonuçlar kullanılarak kıyaslanmıştır. Bu çalışmada test hüzmesinde ve benzeşimde tekli pionlar için farklı hüzme enerjileri kullanılmıştır.

Anahtar Kelimeler: SM, SÜSİ, CMS, ECAL, HCAL

ACKNOWLEDGMENTS

I am heartily thankful to my supervisor, Prof.Dr. Ayşe Polatöz, whose encouragement, guidance and support. I am thankful for her patience and confidence in my study.

I am also grateful to our group adviser, Prof.Dr. Gülsen Önengüt for her encouragement and infinite support during my studies. I also would like to thank to our high energy group members, Prof.Dr. Eda Eşkut, Prof.Dr. Aysel Kayış Topaksu and Assoc. Prof.Dr. İsa Dumanoğlu.

I also would like to thank all the LHC Physics Center staff at Fermilab for their support. I am grateful to Dan Green and Jim Freeman, without them I would not have had the chance to work at the fruitful research atmosphere at Fermilab. Thank you all for letting me participate so intensively.

I would like to record my gratitude to Prof. A. Anwar Bhatti for his supervision, advice, and guidance from the early stage of this research as well as giving me extraordinary experiences during the work.

I am indebted to Shuichi Kunori who has been teaching and guiding me through every step of the research that I have done at Fermilab.

I gratefully acknowledge Gheorghe Lungu for his valuable advice and contribution to this thesis.

I also would like to thank all the people sharing time with me at Fermilab and CERN. Especially I would like to thank Selcuk Cihangir for his beautiful heart and hospitality. A special thanks goes to my dear friend Pelin.

I owe gratitude to my other friends who have shown great understanding and hospitality at Fermilab Taylan, Efe, Stefan, Ashish, Seema, Cosmin, Suvadeep..

Words fail for me to express my appreciation to my wife Seher, whose dediation, love and persistent confidence in me, has taken the load off my shoulder. My little lovely son, İbrahim, welcome to our life.

Most of all, I am deeply grateful to my dear mother, father, brother and sister for their understanding and unique support on my passion for physics.

Finally, I would like to thank everybody who was important to the successful realization of thesis, as well as expressing my apology that I could not mention personally one by one.

CONTENTS **PAGE**

ABSTRACT I

ÖZ II

ACKNOWLEDGMENTS III

CONTENTS IV

LIST OF TABLES VI

LIST OF FIGURES VII

ABBREVIATIONS X

1. INTRODUCTION 1
   1.1. A Short History of Particle Physics 1
   1.2. Fundamental Particles and Interactions 3
   1.3. Electroweak Interactions 4
   1.4. The Strong Interaction and QCD 6
   1.5. Successes and Shortcomings of the Standard Model 7

2. SUPERSYMMETRY 9
   2.1. Chiral Superfields 10
   2.2. Vector Superfields 12
   2.3. SUSY Lagrangian 14
   2.4. The Theoretical MSSM Frame 14
   2.5. The Particles of the MSSM 16
   2.6. The mSUGRA Framework 20
   2.7. Test Points for mSUGRA at CMS 21
   2.8. Decays of Supersymmetric Particles 22
      2.8.1. Decays of Neutralinos and Charginos 22
      2.8.2. Slepton Decays 24
      2.8.3. Squark Decays 25
      2.8.4. Gluino Decays 25
   2.9. Signals at Hadron Colliders 26

3. THE LHC AND THE CMS DETECTOR 28
   3.1. The Large Hadron Collider 28
   3.2. Compact Muon Solenoid 29
      3.2.1. The Inner Tracker 32
      3.2.2. Electromagnetic Calorimeter (ECAL) 34
      3.2.3. Hadronic Calorimeter (HCAL) 35
      3.2.4. Muon System 38
   3.3. The CMS Magnet-Superconducting Solenoid 39
   3.4. Triggers 40

4. RESPONSE COMPARISON OF THE CMS CALORIMETERS TO PIONS BETWEEN MONTE CARLO AND TEST BEAM 42
4.1. Introduction 42
4.2. Test Beam Setup, Beam Clean-up and Particle Identification 42
4.3. Local Clustering and Monte Carlo Data Sets 45
4.4. Energy Deposition in Calorimeters 46
4.5. Optimization of Energy Reconstruction and Response of Calorimeters . . 47

5. ESTIMATION OF QCD AND $t\bar{t}$ BACKGROUND TO SUSY 53
5.1. Jets and Missing Transverse Energy 53
5.2. Used Samples and Initial Kinematic Selections 56
5.3. Rejection of Beam Related and Cosmic Backgrounds 57
5.4. Rejection of QCD Backgrounds 59
5.5. Result 62

6. DETERMINATION OF INVISIBLE Z BOSON+JETS BACKGROUND TO HADRONIC SUSY SEARCH 66
6.1. Estimation of Z+Jets Background 66
6.2. Overview of the Procedure 66
6.3. Samples and Event Selection 68
6.3.1. Muon Sources and Selection 68
6.3.2. Event Selection 71
6.4. Results of the Estimating Procedure 73
6.5. Statistical Uncertainty 74
6.6. Systematic Uncertainties 76
6.7. Result 77

7. CONCLUSION 79

REFERENCES 81

CURRICULUM VITAE 85

LIST OF TABLES **PAGE**

Table 1.1. Fundamental forces and gauge bosons. 5

Table 2.1. Chiral supermultiplets in the MSSM. 20
Table 2.2. Gauge supermultiplets in the MSSM. 20
Table 2.3. mSUGRA parameter values for the test points at CMS. 22

Table 5.1. Used QCD samples in SUSY search analysis in the jet+MET final state. 57
Table 5.2. The definition of event selection used in SUSY search analysis in the jets+MET. 62
Table 5.3. Cumulative selection efficiency for LM1 and QCD samples at each selection step. 65
Table 5.4. Number of events passed all cuts at 1 fb^{-1}. 65

Table 6.1. Summary of the PYTHIA samples used in the analysis. 69
Table 6.2. Summary of the ALPGEN samples used in the analysis. 70
Table 6.3. The definition of the event selection used in the SUSY search analysis in the jets+E_T^{miss} final state 73
Table 6.4. The definition of the loose event selection used in the present analysis. For the combined $Z \rightarrow \mu\mu$+jets ALPGEN sample, the third column shows the cumulative efficiency at each selection step, while the fourth column shows the expected number of events for an integrated luminosity L=1 fb^{-1} 75
Table 6.5. The numbers of events in PYTHIA and in ALPGEN samples with different jet multiplicities ($\geq$1jet, $\geq$ 2jets, and $\geq$3 jets) and for different E_T^{miss} regions ($\geq$ 200 GeV and 100$\rightarrow$200 GeV) 76

LIST OF FIGURES **PAGE**

Figure 1.1. Elementary particles with the gauge bosons in the Standard Model. . . 5

Figure 2.1. Comparison of Z^0 precision measurements with the SM and the MSSM 15

Figure 2.2. Expected relation between M_W and M_{top} in the SM and the MSSM . . . 16

Figure 2.3. Position of the test points in the m_0 versus $m_{1/2}$ plane. 23

Figure 2.4. Feynman diagrams for neutralino and chargino decay chains 24

Figure 2.5. Feynman diagrams for gluino decay chains 26

Figure 3.1. A satellite view of CERN LHC collider 29

Figure 3.2. LHC collision 30

Figure 3.3. LHC collider 31

Figure 3.4. A perspective view of the CMS detector. 32

Figure 3.5. CMS view 33

Figure 3.6. Layout of the CMS electromagnetic calorimeter. 35

Figure 3.7. Longitudinal view of the CMS detector showing the locations of the HB, HE, HO and HF calorimeters. 36

Figure 3.8. Layout of the CMS muon system 38

Figure 3.9. The energy over mass ratio E/M, for several detector magnets 40

Figure 3.10.Schematic view of the CMS trigger system. 41

Figure 4.1. The CERN H2 beam line and the experimental setup. 42

Figure 4.2. EB, HB, HE and HO on the rotatable table. The white line represents the beam. 44

Figure 4.3. Energy deposition in ECAL and HCAL for 50 GeV pion beam for TB. . 46

Figure 4.4. Energy deposition in ECAL and HCAL for 50 GeV pion beam for MC. 47

Figure 4.5. Scatter plot of the 20 GeV incident pion beam data for raw and corrected data. 49

Figure 4.6. Total raw and corrected energy deposition in ECAL+HCAL system for 50 GeV incident pion beams for MC. 49

Figure 4.7. Energy response of calorimeter before and after the energy corrections for Test Beam and MC data. 50

Figure 4.8. Energy resolution for MC and TB data before and after corrections. . . 51
Figure 4.9. Energy Response of ECAL, HCAL and ECAL+HCAL to pions with and without B and Tracker. 52

Figure 5.1. SUSY particle decays in p-p collisions 54
Figure 5.2. Missing Transverse Energy (MET) and corrected MET distributions for QCD, $t\bar{t}$, Z+Jets and LM1 samples at 1 fb^{-1} luminosity. 54
Figure 5.3. Jet Multiplicity and p_T for QCD, $t\bar{t}$, Z+jets and LM1 events at 1 fb^{-1} luminosity. 55
Figure 5.4. MET versus MHT Distribution for $Z(->\mu\mu)$+Jets samples. 56
Figure 5.5. EMFs in mSUGRA LM1 sample 58
Figure 5.6. EMFs in QCD samples 59
Figure 5.7. Event Electromagnetic Fraction in mSUGRA LM1 and QCD samples. . 59
Figure 5.8. Event Charged Fraction in mSUGRA LM1 and QCD samples. 60
Figure 5.9. Angular Cut 61
Figure 5.10.Angular Cut 61
Figure 5.11.Corrected MET and MHT distributions for signal, QCD and $t\bar{t}$ samples. 63
Figure 5.12.MET and MHT distributions in signal (LM1), QCD and $t\bar{t}$ samples. . . 64

Figure 6.1. Global Muon quality variables 71
Figure 6.2. Mass, P_T and E_T^{miss} distributions in $Z->\mu\mu$+jets samples from di-muon mass window. 74
Figure 6.3. E_T^{miss} distribution for events with $\geq$3 jets and passing the R-cuts for the PYTHIA $Z \rightarrow \mu\mu$+jets sample and for the ALPGEN sample. 75
Figure 6.4. E_T^{miss} distribution (circles) from $Z \rightarrow \mu\mu$+jets ALPGEN events passing the loose event selection at 1 fb^{-1} luminosity. Also it is shown the fitted exponential $f^{CR}(MET)$ (line) and the extrapolation of this function into the region SR (squares). 76

Figure 6.5. Estimation of number of $Z \rightarrow \mu\mu$+jets events passing the loose event selection from 10,000 pseudo-experiments (histo) corresponding to an integrated luminosity of 1 fb^{-1}. It is also shown the expectation (blue) from the $Z \rightarrow \mu\mu$+jets ALPGEN sample. The box (yellow) represents the uncertainty on the estimate (red). 77
Figure 6.6. The estimated number of $Z \rightarrow \mu\mu$+jets events, N_{μ}^{SR}, passing the loose event selection in the signal rigion SR, as a function of the integrated luminosity. 78

ABBREVIATIONS

BSM	:	Beyond Standard Model
CERN	:	Conceil Europeenne pour la Recherche Nucleaire
CMS	:	Compact Muon Solenoid
ECAL	:	Electromagnetic Calorimeter
GUT	:	Grand Unified Theory
HCAL	:	Hadronic Calorimeter
HO	:	Hadronic Outer
LHC	:	Large Hadron Collider
LHEP	:	Low High Energy Parameterization
LSP	:	Lightest Supersymmetric Particle
MC	:	Monte Carlo
MET	:	Missing Transverse Energy
MSSM	:	Minimal Supersymmetric Model
mSUGRA	:	minimal Super Gravity
QCD	:	Quantum ChromoDynamics
QED	:	Quantum ElectroDynamics
QFT	:	Quantum Field Theory
QGSP	:	Quark Gluon String Precompound
SLAC	:	Stanford Linear Accelerator Center
SM	:	Standard Model
SUSY	:	SUperSymmetrY
TB	:	Test Beam

1. INTRODUCTION

Particle physics, as an extraordinary discipline, find out to the answers to the basic questions of the universe. It has been trying to explain the physical world as basically as possible by identifying the most basic building blocks of nature and understanding the basic forces that act on between them. A particle physicist wonders what it‘s all made of and what makes this work. In time, physicist‘s knowledge has been improved by the experiments which have probed deeper and deeper into different levels of substructure. During the 20^{th} century, physicists made great works in this field. Many new physics theories were proposed in this century. Supersymmetry (SUSY) was proposed in 1970s and so far, there is no experimental evidence for SUSY. The Large Hadron Collider (LHC) which is the world‘s largest and highest energy particle accelerator will test the SUSY theory of the high energy physics.

In this thesis, SUSY theory will be explained shortly in chapter 2, general overview of LHC and Compact Muon Solenoid (CMS) detector will be given in chapter 3, in chapter 4, comparison of CMS barrel calorimeter energy response to single pions between Monte Carlo and Test Beam 2006 is discussed, estimation of backgrounds to SUSY search at CMS detector of the LHC experiments will be presented in chapters 5 and 6.

1.1. A Short History of Particle Physics

Greek philosophers Leucippos and Democritus who proposed that everything on earth was made of indivisible entities, - ”the atomos”, the Greek word for indivisible in 500 B.C. This hypothesis reduces the great variety of macroscopic phenomena to a small number of fundamental structures and their interactions. The Democritus‘s idea remained unsupported till 1802 when Dalton proposed the atomic theory which considered chemical elements to be composed of atoms. A periodic table was made in 1869 which predicted the existence of additional elements by Mendeleev. It helped Dalton‘s idea. The theory of atoms appear as a first important step towards understanding of nature. By 1900 there were over 80 known elements which rise to supposition that atoms are made of smaller, ’sub-atomic’ constituents. One might say that the modern particle physics began with

J.J.Thomson when he discovered the electron in 1897, which verified the idea of atomic substructure. During the next several decays chemists and physicists worked to figure out the structure of the atom. The work of Max Planck, Niels Bohr, Werner Heisenberg, Erwin Schrödinder and others signed the birth of quantum mechanics, a new set of physical rules to describe the behaviour of particles at the microscopic scale. In 1911, Rutherford proved that atoms consist of a compact positively charged nucleus and a cloud of negative charge from electrons. Later, with the discovery of protons (1919) and neutrons (1932), it became clear that the nucleus is composed of neutrons and protons. Consequently by the early 1930's, physicist had succeeded in developing and understanding that ordinary matter consists of three particles: protons, neutrons and electrons. However, the theory caused new problems. One of the problems was compactness of nucleus. Confining several positive charges into a small region (1 fm=10^{-15} m) results in a strong boost to the electrostatic force. If any nuclei are to be stable then protons must be bound together by a powerful force, enough to overcome this repulsion. This force was called the 'strong' force (Thomson, 1897; Bohr, 1913; Rutherford, 1911; Chadwick, 1932).

Paul Dirac unified the theory of relativity and quantum mechanics into a single theory called 'quantum field theory' (QFT) in 1927. The existence of 'antimatter' particles was predicted also by Paul Dirac. The discovery of the anti-electron (positron) in 1933 was a victory of Dirac's theory and the structure of nature was much more complicated. In 1930, the observation of radioactive decay of atomic nuclei which produces a proton, an electron and an anti-neutrino, a new species of particles was accomplished. This proces can not be explained by electromagnetic or strong interactions, and so requires a new type of process called 'weak' interactions. Thus by the mid-1930s the overall picture was appearing that the description of particle physics needed a quantum field theory incorporating electromagnetic, strong and weak interactions. The strong interaction is transmitted via the exchange of a particle called 'pion' between the proton and the neutron was postulated by Yukawa in 1934. This particle in cosmic rays was searched by Anderson and Nedder meyer, but they found a different particle called the muon (μ). The muon is a particle with the same quantum numbers as the electron, but with a heavier mass. Finally, Cecil Powell discovered the pion in cosmic ray experiments at Bristol in 1947. During the 1940s and 1950s, an amazing variety of particles were discovered in scattering ex-

periments. Tau particle was discovered in Stanford Linear Accelerator Center (SLAC) by Martin L. Perl and his colleagues in the 1975. The existence of powerful particle accelerators and detectors showed us the only reasonable path to learn about the core of the matter at the smallest scale. These particles were classified according to their mass, leptons (light weight), mesons (medium weight) and baryons (heavy weight). Leptons are electron, muon, tau and the neutrinos. The hadrons (mesons and baryons) were classified by Murray Gell-Mann in 1961. Gell-Mann and Zweig proposed the 'quark model' according to which hadrons were composed of three fundamental constituents called 'quarks', which were of three types shown by up, down, and strange (u,d,s) in $1960-64$. Mesons are made of a quark and an antiquark pair and baryons are comprised of three quarks. A fourth quark was discovered (at SLAC and Brookhaven National Laboratory (BNL)) in 1974 and called 'charm' and the quark model derived as a fundamental theory of particle physics. This was because of the fact that the structure and characteristics of all known hadrons could be explained in terms of quarks. The last family of quarks, the 'bottom' and the 'top' quarks were discovered in 1977 and 1995, respectively. A new theoretical framework was being developed to explain the interactions between quarks called Quantum Chromodynamics (QCD) in 1970. During the 1970s, Glashow, Salam and Weinberg unified the electromagnetic and weak interactions into the electroweak theory, which, together with Quantum Chromodynamics, forms the Standard Model (SM) of particle physics. However, gravity, the fourth fundamental force of nature, is not included in the theoretical framework of the SM (Dirac,1927; Fermi,1934; Feynman, 1949; Glashow, 1961; Gell-Mann, 1964; Salam, 1969).

1.2. Fundamental Particles and Interactions

There are two classes of fundamental particles that shape our universe: fermions are matter particles which have half-integer spin and bosons which have integer spin are force carrier particles between fermions. The fermions are also classified into leptons and quarks. There are six flavors of leptons: the electron (e), the muon (μ), the tau (τ), and their corresponding neutrinos $(\nu_e,\ \nu_\mu,\ \nu_\tau)$. The charged leptons interact through the electromagnetic and weak forces, while the neutrinos which are neutral interact with only via

weak force. The neutrinos were assumed to be massless in SM, but experimentally their masses have been constrained to be quite small. There are also six flavors of quarks: up (u), down (d), charm (c), strange (s), top (t) and bottom (b). They have fractional electric charges either $+\frac{2}{3}e$ or $-\frac{1}{3}e$ where e is the charge of the electron. In addition, quarks also have an internal degree of freedom called color (color was proposed to eliminate Pauli exclusion principle violations within hadrons), which might be take three possible states: red, blue and green. In strong interactions, color plays a role similar to the role of electric charge in electromagnetic interactions. Quarks interact due to the strong force as well as the electromagnetic and weak forces. The strong interaction binds the quarks into a spectrum of particles called hadrons, such as nucleons: proton (uud) and neutron (udd). The fermions interact with each other by the three forces in the SM: strong, electromagnetic and weak forces. The gauge bosons are the mediators of the forces between different particles. An interaction between two particles is viewed as a process in which these two particles exchange a virtual gauge boson (some quantized state of the interacting field). The term 'gauge' boson arises from the fact that the Standard Model is a gauge theory, in which the interactions are described by an invariance under 'gauge' transformations. The photon is the quanta of the electromagnetic (EM) forces. The weak force has three quanta, W^+, W^- and Z^0. Eight gluons (g) are the quanta of the strong forces. Thus, there are 12 force carrying particles in the SM (L.Alvarez-Guame, et.al., 2004). The main properties of the forces and their force carriers are summarized in the Table 1.1. The Graviton is not included in the Standard Model. The fundamental particles and force carriers in the Standard Model are shown in Figure 1.1.

1.3. Electroweak Interactions

The theory of quantum electrodynamics (QED) describes the electromagnetic interactions. All particles which carry electric charge may interact with each other via the exchange of photons in the theory. The interaction is long range and falls of like $\frac{1}{r^2}$ because photon is massless. Interaction length is very short in the weak interaction and it acts between any of the leptons and quarks. Weak interaction is responsible for the ra-

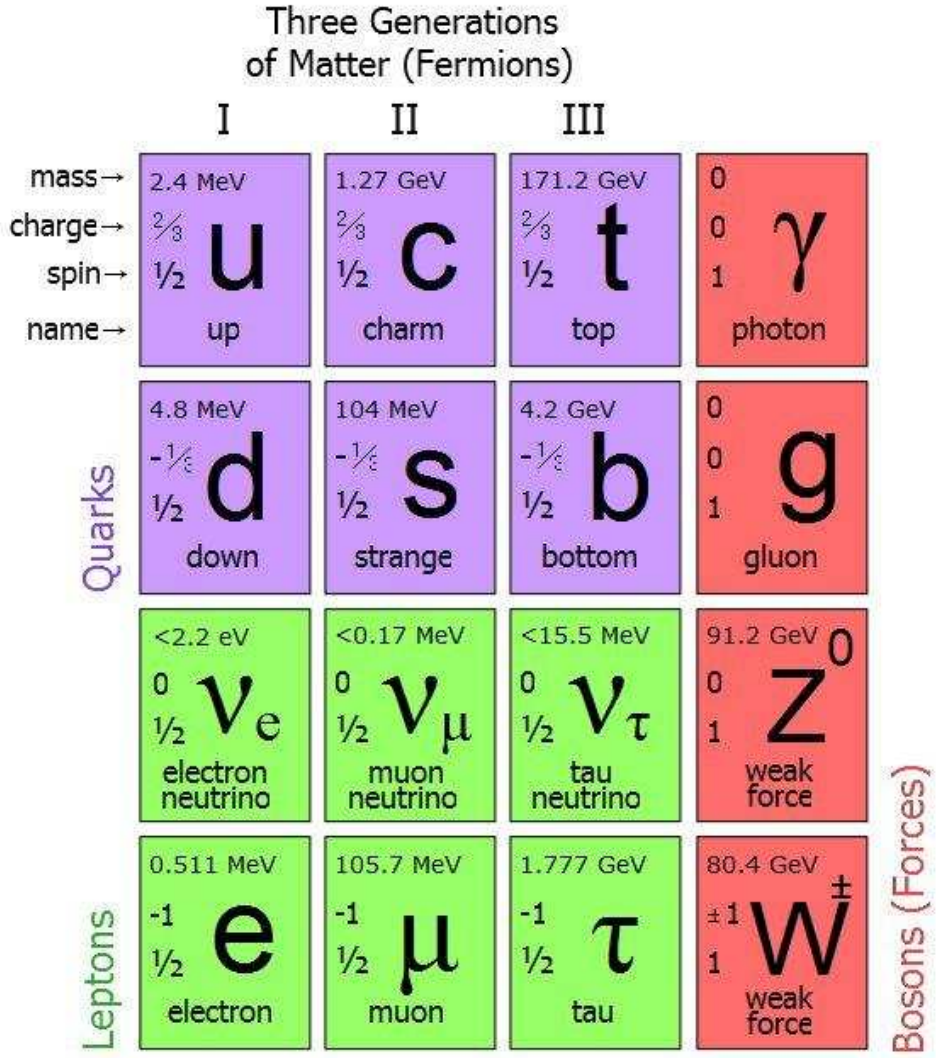


Figure 1.1. Elementary particles with the gauge bosons in the Standard Model.

Table 1.1. Fundamental forces and gauge bosons.

Force	Gauge boson	Charge	Spin	Mass(GeV/c^2)	Range
Strong	Gluon (g)	0	1	0	10^{-15}m
EM	Photon (γ)	0	1	0	∞
Weak	$W^{\pm}$	$\pm$	1	80.423 ± 0.039	10^{-18}m
	Z^0	0	1	91.188 ± 0.002	
Gravity	Graviton (G)	0	2	0	∞

dioactive β-decay of nuclei. This interaction is mediated by three massive gauge bosons, $W^{\pm}$ or Z^0, and therefore it has a short range. At low energies (of the order of muon or electron mass energy), its strength is approximately four orders of magnitude smaller than the strength of the electromagnetic force so it is called "weak". EM and weak interactions have been combined in the Glashow-Salam-Weinberg (GSW) model, and is known as 'Electroweak' force in the SM.

1.4. The Strong Interaction and QCD

Quantum Choromodynamics (QCD) describes the strong interaction. The 'color' charge is responsible for this interaction. Particles with non zero color charge can interact with each other via the exchange of gluons. The strong interaction has a short-range force which is responsible for confining the quarks into hadrons. There are three important ways between QCD and QED.

1. There is one kind of charge in QED but there are three kinds of color charge in QCD.

2. Photons are uncharged in QED and so they cannot couple to each other while gluons carry color charge in QCD (one unit each of color and anticolor) and they interact directly with each other through strong force.

This self-interaction between gluons brings the third and major difference between the QED and QCD. In QED, an electric charge polarizes the vacuum due to the virtual electron-positron pairs which surround it. The charge density is higher near the charge and results in an effective coupling constant given by

$$\alpha_E = \frac{\alpha_\mu}{1 - \frac{\alpha(\mu)}{3\times\pi}\ln(\frac{Q^2}{\mu^2})} \tag{1.1}$$

where Q is related to the energy of the probe and μ is lower cutoff energy. In QCD, a quark is surrounded by not only virtual quark-antiquark pairs, but by virtual gluon pairs as well. The virtual gluon pairs decrease the effective strong coupling constant near the quarks, whereas quark-antiquark pairs increase the effective coupling. The gluon pairs effect dominates and α_s is decreased near the quarks. The strong coupling constant has

the form:

$$\alpha_s(Q^2) = \frac{12 \times \pi}{33 - 2n_f \ln(\frac{Q^2}{\Lambda^2})} \tag{1.2}$$

where n_f is the number of quark flavors, Λ is QCD scaling parameter, and Q is momentum transfer during the interaction. At lower energies (large distances), the strong coupling constant grows rapidly and becomes large which explains why quarks always confine themselves in the color neutral combinations of mesons or baryons. This phenomenon of confinement of quarks in a hadron is called color-confinement. At large interaction energies typical of modern high-energy experiments (E>10 GeV i.e. short distances), α_s approaches zero and so quarks (essentially bound up in hadrons) behave as if they were free particles. This is known as "asymptotic freedom". This is the reason that perturbative methods can be used for high momentum transfer QCD calculations. However, at lower energies, the coupling strength becomes large enough that perturbative theory breaks down. Even in high-energy collisions, the quarks do not remain free for very long. Within a time scale typical of strong interactions (10^{-24} s), quark-antiquark pairs are pulled out of the vacuum which bind with the quarks from the hard scattering to form composite particles. This process is referred to as fragmentation or hadronization. Hence, in high energy collisions of hadrons, although it is the quarks and gluons which are fundamental participants in the interaction, only the composite hadrons are available to the experimenters. Because of conservation of energy and momentum, the hadrons which are produced form a collimated jet of hadronic particles along the direction of the original quark (Kumar, 2005).

1.5. Successes and Shortcomings of the Standard Model

The Standard Model of particle physics is a well tested theory with a huge amount of data over an energy range from a fraction of an electronvolt to about 1 TeV. Its predictions are consistent with the data within 0.1%. However, SM does not give an answer to some important physics questions without the introduction of some new physics. The electroweak theory was verified by the discovery of W and Z bosons. Masses of W and Z bosons were experimentally tested by the Underground Area 1 (UA1) and UA2 experi-

ments at CERN in 1980s. Also, the electroweak theory was tested at Tevatron to the 10^{-3} level. Another example of the success of the SM is the top quark and tau neutrino which were predicted by the SM and were discovered in 1995 and 2000, respectively. There are some problems of the SM. Graviton, gauge boson of the Gravity, is not included in the Standard Model. Neutrinos are massless particles in the SM but neutrino experiments strongly suggest that neutrinos have mass. In order to explain the mass problem Higgs mechanism is added to the theory. Particles receive their masses from the scalar Higgs fields. When the neutral component of the Higgs boson gets a vacuum expectation value, the $SU(2)_L \times U(1)_Y$ gauge symmetry is broken, giving the mass to W and Z gauge bosons. The chiral symmetry forbidding fermion masses is broken at the same time allowing the fermions to become massive (Dawson, 1997). The number of free parameters in SM is quite large and there is no explanation why there are exactly three families. The Higgs mechanism give masses to the particles but it leads to the hierarchy problem, which arises from the huge differences in energy scales of the various interactions: the QCD scale is of the order of 1 GeV ($\sim M_{Meson}$); the electroweak scale is of 100 GeV ($\sim M_{W,Z}$); the scale of grand unification (GUT) is $\sim 10^{16}$ GeV; while the Plancks mass scale is $\sim 10^{19}$ GeV (Kumar, 2005). The Standard Model of particles does not explain very well how the universe works because of the above problems. The SM is more likely just an approximation of the truth. In order to find explanations to the above questions, many new theories have been developed beyond the SM such as Grand Unified Theories (GUT), SUSY theories, etc. The CMS experiment of the LHC experiments will test the SUSY theory of the new physics.

2. SUPERSYMMETRY

Supersymmetry (SUSY) is a symmetry between fermions and bosons. A fermion can be transformed into a boson and a boson into a fermion under the supersymmetry generator operator Q. Each particle of Standard Model has a super partner which differs by $1/2$ unit in spin.

$$Q|BOSON>=|FERMION>, Q|FERMION>=|BOSON> \tag{2.1}$$

The simplest choice of SUSY generators is a 2-component (Weyl) spinor Q and its conjugate $\bar{Q}$. Since these generators are fermionic, their algebra can most easily be written in terms of anti-commutators. From now on I will follow the paper of Manuel Drees (Drees, 1996):

$$\{Q_\alpha, Q_\beta\} = \{\bar{Q}_{\dot{\alpha}}, \bar{Q}_{\dot{\beta}}\} = 0; \tag{2.2}$$

$$\{Q_\alpha, \bar{Q}_{\dot{\beta}}\} = 2\sigma^\mu_{\alpha\dot{\beta}} P_\mu; \quad [Q_\alpha, P_\mu] = 0 \tag{2.3}$$

Here the indices α and β of Q and $\dot{\alpha}$, $\dot{\beta}$ of $\bar{Q}$ take values 1 or 2, $\sigma^\mu = (1, \sigma_i)$ being the Pauli matrices, and P_μ is the translation generator. For a compact description of SUSY transformations, it will prove convenient to introduce "fermionic coordinates" $\theta, \dot{\theta}$. These are anti-commuting, "Grassmann" variables:

$$\{\theta, \theta\} = \{\theta, \bar{\theta}\} = \{\bar{\theta}, \bar{\theta}\} = 0 \tag{2.4}$$

A "finite" SUSY transformation can then be written as $exp[i(\theta Q + \bar{Q}\bar{\theta} - x_\mu P^\mu)]$; this is to be compared with a non-abelian gauge transformation $exp(i\varphi_a T^a)$, with T^a being the group generators. Of course, the objects on which these SUSY transformations act must then also depend on θ and $\bar{\theta}$. This leads to the introduction of *superfields*, which can be understood to be functions of θ and $\bar{\theta}$ as well as the spacetime coordinates x_μ. Since θ and $\bar{\theta}$ are also two-component spinors, one can even argue that SUSY doubles the dimension of spacetime, the new dimensions being fermionic. For most purposes it is sufficient to consider infinitesimal SUSY transformations. These can be written as

$$\delta_S(\alpha, \bar{\alpha})\Phi(x, \theta, \bar{\theta}) = [\alpha\frac{\partial}{\partial\theta} + \bar{\alpha}\frac{\partial}{\partial\bar{\theta}} - i(\alpha\sigma_\mu\bar{\theta} - \theta\sigma_\mu\bar{\alpha})\frac{\partial}{\partial x_\mu}]\Phi(x, \theta, \bar{\theta}) \tag{2.5}$$

where Φ is a superfield and α, $\bar{\alpha}$ are again Grassmann variables. This corresponds to the following explicit representation of the SUSY generators:

$$Q_\alpha = \frac{\partial}{\partial\theta^\alpha} - i\sigma^\mu_{\alpha\dot{\beta}}\bar{\theta}^{\dot{\beta}}\partial_\mu; \quad \bar{Q}_{\dot{\alpha}} = -\frac{\partial}{\partial\bar{\theta}^{\dot{\alpha}}} + i\theta^\beta\sigma^\mu_{\theta\dot{\alpha}}\partial_\mu; \tag{2.6}$$

It will prove convenient to introduce SUSY-covariant derivatives, which anti-commute with the SUSY transformation:

$$D_\alpha = \frac{\partial}{\partial\theta^\alpha} + i\sigma^\mu_{\alpha\dot{\beta}}\bar{\theta}^{\dot{\beta}}\partial_\mu; \quad \bar{D}_{\dot{\alpha}} = -\frac{\partial}{\partial\bar{\theta}^{\dot{\alpha}}} - i\theta^\beta\sigma^\mu_{\theta\dot{\alpha}}\partial_\mu; \tag{2.7}$$

Note that equations 2.5-2.7 imply that α and θ have mass dimension $-1/2$, while Q and D have mass dimension $+1/2$. Equations 2.5 and 2.7 have been written in a form that treats θ and $\bar{\theta}$ on equal footing. It is often more convenient to use "chiral" representations, where θ and $\bar{\theta}$ are treated slightly differently: L-representation:

$$\begin{aligned}
&\delta_S\Phi_L = (\alpha\frac{\partial}{\partial\theta} + \bar{\alpha}\frac{\partial}{\partial\bar{\theta}} + 2i\theta\sigma^\mu\bar{\alpha}\partial_\mu)\Phi_L; \\
&D_L = \frac{\partial}{\partial\theta} + 2i\sigma^\mu\bar{\theta}\partial_\mu; \quad \bar{D}_L = -\frac{\partial}{\partial\dot{\bar{\theta}}}
\end{aligned} \tag{2.8}$$

R-representation:

$$\begin{aligned}
&\delta_S\Phi_R = (\alpha\frac{\partial}{\partial\theta} + \bar{\alpha}\frac{\partial}{\partial\bar{\theta}} - 2i\theta\sigma^\mu\bar{\theta}\partial_\mu)\Phi_R; \\
&\bar{D}_R = -\frac{\partial}{\partial\bar{\theta}} - 2i\theta\sigma^\mu\partial_\mu; \quad D_R = \frac{\partial}{\partial\dot{\theta}}
\end{aligned} \tag{2.9}$$

Clearly, $\bar{D}$ (D) has a particulary simple form in the L (R) representation. The following identity allows to switch between representations:

$$\Phi(x,\theta,\bar{\theta}) = \Phi_L(x_\mu + i\theta\sigma_\mu\bar{\theta},\theta,\bar{\theta}) = \Phi_R(x_\mu - i\theta\sigma_\mu\bar{\theta},\theta,\bar{\theta}) \tag{2.10}$$

So far everything has been written for arbitrary superfields Φ. However, we will only need two kinds of special superfields, which are *irreducible* representations of the SUSY algebra; Chiral and Vector superfields (Drees, 1996).

2.1. Chiral Superfields

The first kind of superfield we will need are *chiral superfields*. This name is derived from the fact that the SM fermions are chiral, that is, their left- and right-handed

components transfer differently under $SU(2)_L \times U(1)_Y$. We therefore need superfields with only two physical fermionic degrees of freedom, which can then describe the left- or right-handed component of an SM fermion. Of course, the same superfields will also contain bosonic partners, the *sfermions*. The simplest way to construct such superfields is to require either

$$\bar{D}\Phi_L \equiv 0 \tag{2.11}$$

or

$$D\Phi_R \equiv 0. \tag{2.12}$$

where Φ_L is left- and Φ_R is right-chiral. Clearly these conditions are most easily implemented using the chiral representations of the SUSY generators and SUSY covariant derivatives. For example, equation 2.8 shows that in the L-representation, equation 2.11 simply implies that Φ_L is independent of $\bar{\theta}$, i.e. Φ_L only depends on x and θ. Recalling that θ is an anticommuting Grassmann variable, equation 2.4, we can then expand Φ_L as:

$$\Phi_L(x,\theta) = \phi(x) + \sqrt{2}\theta^\alpha \psi_\alpha(x) + \theta^\alpha \theta^\beta \varepsilon_{\alpha\beta} F(x), \tag{2.13}$$

where summation over identical upper and lower indices is understood, and $\varepsilon_{\alpha\beta}$ is the anti-symmetric tensor in two dimensions. Recall that θ has mass dimension $-1/2$. Assigning the usual mass dimension $+1$ to the scalar field ϕ then gives the usual mass dimension $+3/2$ for the fermionic field ψ, and the unusual mass dimension $+2$ for the scalar field F; the superfield Φ itself has mass dimension $+1$. The expansion (2.13) is exact, since θ only has two components, and equation 2.4 implies that the square of any one component vanishes; hence there cannot be any terms with three or more factors of θ. The fields ϕ and F are complex scalars, while ψ is a Weyl spinor. At first glance, Φ_L seems to contain four bosonic degrees of freedom and only two fermionic ones; however, we will see later on that not all bosonic fields represent physical (propagating) degrees of freedom. The expression for Φ_R in the R-representation is very similar; one merely has to replace θ by $\bar{\theta}$. Applying the explicit form 2.8 of the SUSY transformation to the left-chiral superfield 2.13 gives:

$$\begin{aligned} \delta_S \Phi_L &= \sqrt{2}\alpha^\alpha \psi_\alpha + 2\alpha^\alpha \theta^\theta \varepsilon_{\alpha\beta} F + 2i\theta^\alpha \sigma^\mu_{\alpha\dot{\beta}} \bar{\alpha}^{\dot{\beta}} \partial_\mu \phi + 2\sqrt{2} i \theta^\alpha \sigma^\mu_{\alpha\dot{\beta}} \bar{\alpha}^{\dot{\beta}} \theta^\beta \partial_\mu \psi_\beta \\ &\equiv \delta_S \phi + \sqrt{2}\theta \delta_S \psi + \theta\theta \delta_S F \end{aligned} \tag{2.14}$$

The first two terms of the first line of equation 2.14 come from the application of the $\frac{\partial}{\partial\theta}$ part of δ_S, while the last two terms come from the ∂_μ part; note that the ∂_μ part applied to the last term in equation 2.13 vanishes, since it contains three factors of θ. The second line of equation 2.14 is just the statement that the SUSY algebra should close, i.e. a SUSY transformation applied to a left-chiral superfield should again give a left-chiral superfield. It is easy to see that this is true, since the first line of equation 2.14 does not contain any terms $\propto \bar{\theta}$, so an expansion as in equation 2.13 must be applicable to it. Explicitly, we have (Drees, 1996):

$$\delta_S\phi = \sqrt{2}\alpha\psi \qquad \text{(boson} \rightarrow \text{fermion)} \tag{2.15}$$

$$\delta_S\psi = \sqrt{2}\alpha F + i\sqrt{2}\sigma^\mu\bar{\alpha}\partial_\mu\phi \qquad \text{(fermion} \rightarrow \text{boson)} \tag{2.16}$$

$$\delta_S F = -i\sqrt{2}\partial_\mu\psi\sigma^\mu\bar{\alpha} \qquad \text{(F} \rightarrow \text{total derivative)} \tag{2.17}$$

2.2 Vector Superfields

The chiral superfields introduced in the previous subsection can describe spin-0 bosons and spin-1/2 fermions, e.g. the Higgs boson and the quarks and leptons of the SM. However, we also have to describe the spin-1 gauge bosons of the SM. To this end one introduces *vector superfields* V. They are constrained to be self-conjugate:

$$V(x,\theta,\bar{\theta}) \equiv V^\dagger(x,\theta,\bar{\theta}) \tag{2.18}$$

This leads to the following representation of V in component form:

$$\begin{aligned} V(x,\theta,\bar{\theta}) &= (1+\frac{1}{4}\theta\theta\overline{\theta\theta}\partial_\mu\partial^\mu)C(x) + (i\theta + \frac{1}{2}\theta\theta\sigma^\mu\overline{\theta}\partial_\mu)\chi(x) + \frac{i}{2}\theta\theta[M(x)+iN(x)] \\ &+ (-i\overline{\theta} + \frac{1}{2}\overline{\theta\theta}\sigma^\mu\theta\partial_\mu)\overline{\chi}(x) - \frac{i}{2}\overline{\theta\theta}[M(x)-iN(x)] \\ &- \theta\sigma_\mu\overline{\theta}A^\mu(x) + i\theta\theta\overline{\theta\lambda}(x) - i\overline{\theta\theta}\theta\lambda(x) + \frac{1}{2}\theta\theta\overline{\theta\theta}D(x) \end{aligned} \tag{2.19}$$

Here, C, M, N and D are real scalars, χ and λ are Weyl spinors, and A^μ is a vector field. If A^μ is to describe a gauge boson, V must transform as an adjoint representation of the gauge group. The general form of 2.19 is rather unwieldy. Fortunately, we now have many more gauge degrees of freedom than in nonsupersymmetric theories, since now

the gauge parameters are themselves superfields. A general non-abelian supersymmetric gauge transformation acting on V can be described by

$$e^{gV} \rightarrow e^{-ig\Lambda^\dagger} e^{gV} e^{ig\Lambda} \tag{2.20}$$

where $\lambda(x,\theta,\overline{\theta})$ is a chiral superfield and g is the gauge coupling. In the case of an abelian gauge symmetry, this transformation rule can be written more simply as

$$V \rightarrow V + i(\Lambda - \Lambda^\dagger) \qquad \text{(abelian case)} \tag{2.21}$$

Remembering that a chiral superfield contains four scalar (bosonic) degrees of freedom as well as one Weyl spinor, it is quite easy to see that one can use the transformation 2.20 or 2.21 to choose

$$\chi(x) = C(x) = M(x) = N(x) \equiv 0. \tag{2.22}$$

This is called "Wess-Zumino" (W-Z) gauge; it is in some sense the SUSY analog of the unitary gauge in "ordinary" field theory, since it removes many unphysical degrees of freedom. Notice, however, that we have only used three of the four bosonic degrees of freedom in λ. We therefore still have the "ordinary" gauge freedom, e.g. according to $A_\mu(x) \rightarrow A_\mu(x) + \partial_\mu \varphi(x)$ for an abelian theory. In other words, the W-Z gauge can be used in combination with any of the usual gauges. However, the choice 2.22 is sufficient by itself to remove the first two lines of equation 2.19 leading to a much more compact expression for V. Assigning the usual mass dimension +1 to A^μ gives the canonical mass dimension +3/2 for the fermionic field λ, while the field D has the unusual mass dimension +2, just like F-component of the chiral superfield (2.13). Notice also that the superfield V itself has no mass dimension. Applying a SUSY transformation to equation 2.19 obviously gives a lengthier expression than in case of chiral superfields. Here only the important result

$$\delta_S D = -\alpha\sigma^\mu \partial_\mu \overline{\lambda} + \overline{\alpha}\sigma^\mu \partial_\mu \lambda \tag{2.23}$$

which shows that the D component of a vector superfield transforms into a total derivative (Drees, 1996).

2.3. SUSY Lagrangian

The particles are combined into *superfields*, which contains fields differing by one-half unit of spin. The simplest example, the scalar superfield, contains a complex scalar, S, and two component Majorana fermion, ψ. (A Majorana fermion, ψ, is one which is equal to its charge conjugate, $\psi^c = \psi$. A familiar example is a Majorana neutrino). The supersymmetry completely specifies the allowed interactions. In this simple case, the Lagrangian is

$$\begin{aligned} \mathcal{L} &= -\partial_\mu S^* \partial^\mu S - \mathrm{i}\overline{\psi}\,\overline{\sigma}^\mu \partial_\mu \psi - \frac{1}{2} m(\psi\psi - \overline{\psi}\overline{\psi}) \\ &\quad -cS\psi\psi - c^* S^* \overline{\psi}\overline{\psi} - |mS + cS^2|^2 \,, \end{aligned} \tag{2.24}$$

(where σ is a 2×2 Pauli matrix, c is an arbitrary coupling constant and m is mass terms). This Lagrangian is invariant (up to a total derivative) under transformations which take the scalar into the fermion and *vice versa*. Since the scalar and fermion interactions have the same coupling, the cancelation of quadratic divergences occurs automatically. One thing that is immediately obvious is that this Lagrangian contains both a scalar and a fermion of *equal* mass. Supersymmetry connects particles of different spin, but with all other characteristic are the same.

- Particles in a superfield have the same masses and quantum numbers and differ by $1/2$ unit of spin in a theory with unbroken supersymmetry.

It is clear that, **supersymmetry must be a broken symmetry**. There is no scalar particle, for example, there is no selectron with mass 511 keV. In fact, there are no candidate supersymmetric scalar partners for any of the fermions in the experimentally observed spectrum. Supersymmetric theories are easily constructed according to the rules of supersymmetry (Dawson, 1997). One of them is Minimal Supersymmetric (MSSM) version of the Standard Model.

2.4. The Theoretical MSSM Frame

The Minimal Supersymmetric Standard Model (MSSM) is basically a supersymmetrization of the Standard Model as indicated by the name. Particularly, ”minimal”

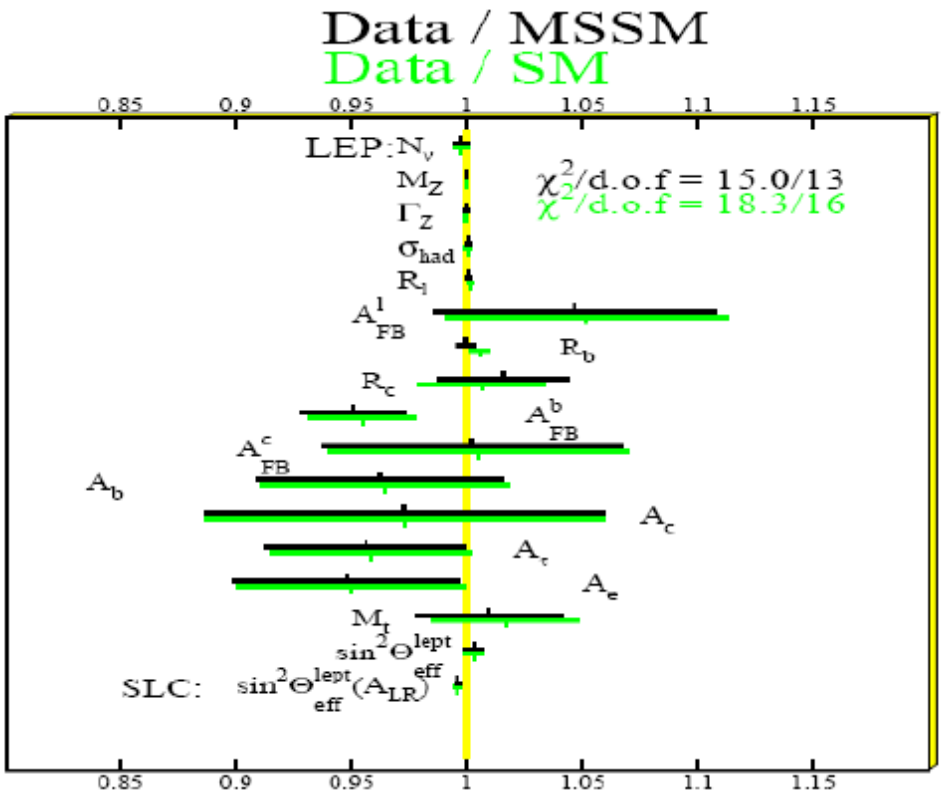


Figure 2.1. Comparison of Z^0 precision measurements with the SM and the MSSM with tanβ=1.6 and very heavy SUSY particles (Hollik, 1998)

means that keep the number of superfields and interactions as small as possible in the model. This model is usually believed to be the most studied theoretical framework because;

- it is fairly close to the SM;
- it explains the hierarchy problem of SM;
- it allows to discovery many new particles.

The coherence of the different electroweak measurements with the SM and MSSM shown in Figure 2.1 and 2.2. The biggest inconsistency appearin the measurements of the $W^{\pm}$ mass and the top mass and shown in Figure 2.2. Today's data shows that, mass of M_W=80.39 $\pm$ 0.06 GeV and mass of M_{top}=174$\pm$ 5 GeV, which perfectly agree with both models. One might thus conclude that the expected small improvements of the electroweak measurements will not allow to distinguish between the SM and the MSSM (Dittmar, 1999).

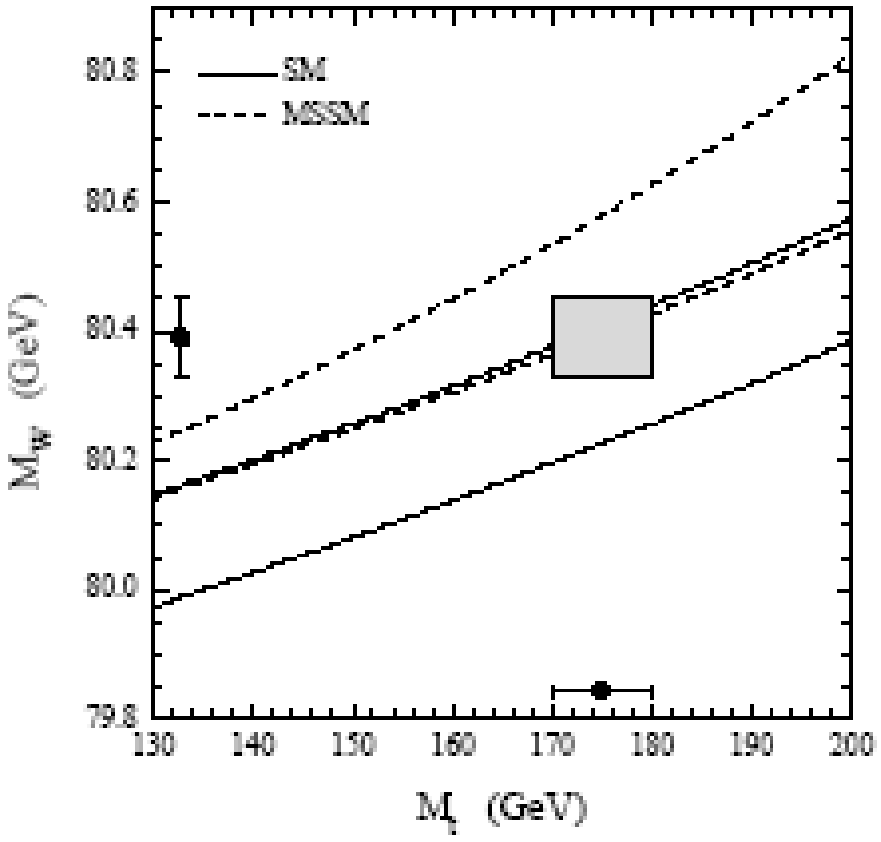


Figure 2.2. Expected relation between M_W and M_{top} in the SM and the MSSM; the bounds are from the non observation of Higgs or SUSY particles at LEPII (Hollik, 1998)

2.5. The Particles of the MSSM

In a Minimal Supersymmetric Standard Model, each of the Standard Model particles is in a chiral or gauge supermultiplet, and must have a superpartner with spin differing by $1/2$ unit. The first step in understanding the inspiring phenomenological results of this assumption is to decide exactly how the SM particles fit into supermultiplets, and to give them proper names. A fateful observation is here that only chiral supermultiplets can include fermions whose left-handed parts transform differently under the gauge group then their right-handed parts. All of the SM fermions (the known quarks and leptons) have this feature, so they must be members of chiral supermultiplets. The names of the $spin-0$ partners of the quarks and leptons are renamed by prefixing an "s", for scalar. Thus, usually they are called *squarks* and *sleptons* or sometimes *sfermions*. The left-handed and

right-handed quarks and leptons are separate two-component Weyl fermions with different gauge transformation properties in the SM, so each must have its own complex scalar partner. The symbols for the squarks and sleptons are the same as for the corresponding fermion, but with a tilde $\widetilde{()}$ used to indicate the superpartner of a SM particle. For example, the superpartners of the left-handed and right-handed parts of the electron Dirac field are called left- and right-handed selectrons, and are indicated by $\widetilde{e_L}$ and $\widetilde{e_R}$. A similar way applies for smuons and staus: $\widetilde{\mu}_L$, $\widetilde{\mu}_R$, $\widetilde{\tau}_L$, $\widetilde{\tau}_R$. The SM neutrinos are always left-handed, so the sneutrinos are indicated generically by $\widetilde{\nu}$, with a possible subscript indicating which lepton flavor they carry: $\widetilde{\nu}_e$, $\widetilde{\nu}_\mu$, $\widetilde{\nu}_\tau$. Finally, a complete list of the squarks is $\widetilde{q}_L$, $\widetilde{q}_R$ with $q = u,d,s,c,b,t$. The gauge interactions of each of these squark and slepton fields are the same as for the corresponding SM fermions; for instance, the left-handed squarks $\widetilde{u}_L$ and $\widetilde{d}_L$ couple to the W boson, while $\widetilde{u}_R$ and $\widetilde{d}_R$ do not. The Higgs scalar boson has spin 0 and it must reside in a chiral supermultiplet. Actually, it generates that just one chiral supermultiplet is not enough. One reason for this is that if there were only one Higgs chiral supermultiplet, the electroweak gauge symmetry would suffer a gauge anomaly, and would be inconsistent as a quantum theory. This is because the conditions for cancelation of gauge anomalies include $Tr[T_3^2 Y] = Tr[Y^3] = 0$, where T_3 and Y are the third component of weak isospin and the weak hypercharge, respectively, in a normalization where the ordinary electric charge is $Q_{EM} = T_3 + Y$. The traces run over all of the left-handed Weyl fermionic degrees of freedom in the theory. In the SM, these conditions are already satisfied, somewhat miraculously, by the known quarks and leptons. Now, a fermionic partner of a Higgs chiral supermultiplet must be a weak isodoublet with weak hypercharge $Y = 1/2$ or $Y = -1/2$. In either case alone, such a fermion will make a non-zero contribution to the traces and spoil the anomaly cancelation. This can be avoided if there are two Higgs supermultiplets, one with each of $Y = \pm 1/2$, so that the total contribution to the anomaly traces from the two fermionic members of the Higgs chiral supermultiplets vanishes by cancelation. These are also necessary for another completely different reason: because of the structure of supersymmetric theories, only a $Y = 1/2$ Higgs chiral supermultiplet can have the Yukawa couplings necessary to give masses to charge $+2/3$ up-type quarks (up, charm, top), and only a $Y = -1/2$ Higgs can have the Yukawa couplings to give masses to charge $-1/3$ down type quarks

(down, strange, bottom) and to the charged leptons. We will call the $SU(2)_L$-doublet complex scalar fields with $Y = 1/2$ and $Y = -1/2$ by the names H_u and H_d, respectively. The weak isospin components of H_u with $T_3 = (1/2\ \ -1/2)$ have electric charges $1,0$ respectively and denoted $(H_u^+\ H_u^0)$. Similarly, the $SU(2)_L$-doublet complex scalar H_d has $T_3 = (1/2\ -1/2)$ components $(H_d^0\ H_d^-)$. The neutral scalar that corresponds to the physical SM Higgs boson is in a linear combination of H_u^0 and H_d^0. The generic nomenclature for a spin-$1/2$ superpartner is to append "$-ino$" to the name of the SM particle, so the fermionic partners of the Higgs scalars are called higgsinos. They are denoted by $\widetilde{H}_u$, $\widetilde{H}_d$ for the $SU(2)_L$-doublet left-handed Weyl spinor fields, with weak isospin components $\widetilde{H}_u^+$, $\widetilde{H}_u^0$ and $\widetilde{H}_d^0$, $\widetilde{H}_d^-$. We have now found all of the chiral supermultiplets of the MSSM. They are summarized in Table 2.1, classified according to their transformation properties under the SM gauge group $SU(3)_C \times SU(2)_L \times U(1)_Y$, which combines u_L, d_L and ν, e_L degrees of freedom into $SU(2)_L$ doublets. All chiral supermultiplets are defined in terms of left-handed Weyl spinors, so that the *conjugates* of the right-handed quarks and leptons (and their superpartners) appear in Table 2.1. It is also useful to have a symbol for each of the chiral supermultiplets as a whole; these are indicated in the second column of Table 2.1. Thus, for example, Q stands for the $SU(2)_L$-doublet chiral supermultiplet containing $\widetilde{u_L}$, u_L (with weak isospin component $T_3 = 1/2$), and $\widetilde{d_L}$, d_L (with T_3=-1/2), while $\bar{u}$ stands for the $SU(2)_L$-singlet supermultiplet containing $\widetilde{u}_R^*$, $u_R^\dagger$. There are three families for each of the quark and lepton supermultiplets, Table 2.1. lists the first family representatives. A family index i =1,2,3 can be affixed to the chiral supermultiplet names $(Q_\mathrm{i},\ \overline{u_\mathrm{i}}\ ..)$ when needed, for example $(\bar{e}_1,\ \bar{e}_2,\ \bar{e}_3) = (\bar{e},\ \bar{\mu},\ \bar{\tau})$. The bar on $\bar{u}$, $\bar{d}$, $\bar{e}$ fields is part of the name, and does not denote any kind of conjugation. The Higgs chiral supermultiplet H_d (containing H_d^0, H_d^- $\widetilde{H}_d^0$, $\widetilde{H}_d^-$) has exactly the same SM gauge quantum numbers as the left-handed sleptons and leptons L_i, for example $(\widetilde{\nu},\ \widetilde{e}_L,\ \nu,\ e_L)$.

The vector bosons of the SM clearly must reside in gauge supermultiplets. Their fermionic superpartners are generically referred to as gauginos. The $SU(3)_C$ color gauge interactions of QCD are mediated by the gluon, whose spin$-1/2$ color-octet supersymmetric partner is the gluino. As usual, a tilde is used to denote the supersymmetric partner of a SM state, so the symbols for the gluon and gluino are g and $\widetilde{g}$ respectively. The electroweak gauge symmetry $SU(2)_L \times U(1)_Y$ is associated with spin-1 gauge bosons W^+,

W^0, W^- and B^0, with spin$-1/2$ superpartners $\widetilde{W}^+$, $\widetilde{W}^0$, $\widetilde{W}^-$ and $\widetilde{B}^0$, called winos and bino. After electroweak symmetry breaking, the W^0 and B^0 gauge eigenstates mix to give mass eigenstates Z^0 and γ. The corresponding gauge mixtures of $\widetilde{W}^0$ and $\widetilde{B}^0$ are called zino $\widetilde{Z}^0$ and photino $(\widetilde{\gamma})$; if supersymmetry were unbroken, they would be mass eigenstates with masses m_Z and 0. Table 2.2 summarizes the gauge supermultiplets of a minimal supersymmetric extension of the Standard Model. The chiral and gauge supermultiplets in Tables 2.1 and 2.2 make up the particle content of the Minimal Supersymmetric Standard Model. The most obvious and interesting feature of this theory is that none of the superpartners of the SM particles has been discovered as of this writing. If supersymmetry were unbroken, then there would have to be selectrons $\widetilde{e}_L$ and $\widetilde{e}_R$ with masses exactly equal to $m_e = 0.511$ MeV. A similar statement applies to each of the other sleptons and squarks, and there would also have to be a massless gluino and photino. These particles would have been extraordinarily easy to detect long ago. Clearly, therefore, supersymmetry is a broken symmetry in the vacuum state chosen by Nature.

It is known that none of the fields of the MSSM can develop nonzero vacuum expectation value (V.E.V) to break SUSY without spoiling gauge invariance. In the most common scenarios SUSY breaking occurs in the hidden sector and propagates to the visible sector via messengers. There are several known mechanisms to mediate SUSY breaking from hidden to visible sector: gravity mediation (SUGRA), gauge mediation (GMSB), anomaly mediation (AMSB), and gaugino mediation (inoMSB). In SUGRA scenario the hidden sector communicates with visible one via gravity, leading to the SUSY breaking scale $M_{SUSY} \sim m_{3/2}$, where $m_{3/2}$ is the gravitino mass. Scalar masses m_{ij}, gaugino masses M_a and trilinear couplings are proportional to $m_{3/2}$ but can be non-universal in general. In this case one should properly address flavor and CP problem. In minimal SUGRA (mSUGRA) scenario the universality hypothesis of equal boundary conditions at the GUT scale greatly reduces the number of parameters (Belyaev, 2004). Starting from the MSSM, the so called minimal model, theoretical counting results in more than hundred free parameters. So many free parameters do not offer a good guidance for experimentalist, who prefer to use additional assumptions to constrain the parameter space. The simplest approach is the so called minimal Super Gravity (mSUGRA) model with only five parameters.

Table 2.1. Chiral supermultiplets in the MSSM (Martin, 2006).

Names		spin 0	spin 1/2	$SU(3)_C$, $SU(2)_L$, $U(1)_Y$
squarks, quarks	Q	$(\widetilde{u}_L\ \widetilde{d}_L)$	$(u_L\ d_L)$	$(\mathbf{3},\ \mathbf{2},\ \frac{1}{6})$
($\times$3families)	$\overline{u}$	$\widetilde{u}_R^*$	$u_R^\dagger$	$(\overline{\mathbf{3}},\ \mathbf{1},\ -\frac{2}{3})$
	$\overline{d}$	$\widetilde{d}_R^*$	$d_R^\dagger$	$(\overline{\mathbf{3}},\ \mathbf{1},\ \frac{1}{3})$
sleptons, leptons	L	$(\widetilde{\nu}\ \ \widetilde{e}_L)$	$(\nu\ \ e_L)$	$(\mathbf{1},\ \mathbf{2},\ -\frac{1}{2})$
($\times$3families)	$\overline{e}$	$\widetilde{e}_R^*$	$e_R^\dagger$	$(\mathbf{1},\ \mathbf{1},\ 1)$
Higgs, higgsinos	H_u	$(H_u^+\ \ H_u^0)$	$(\widetilde{H}_u^+\ \ \widetilde{H}_u^0)$	$(\mathbf{1},\ \mathbf{2},\ +\frac{1}{2})$
	H_d	$(H_d^0\ \ H_d^-)$	$(\widetilde{H}_d^0\ \ \widetilde{H}_d^-)$	$(\mathbf{1},\ \mathbf{2},\ -\frac{1}{2})$

Table 2.2. Gauge supermultiplets in the MSSM (Martin, 2006).

Names	spin 1/2	spin 1	$SU(3)_C$, $SU(2)_L$, $U(1)_Y$
gluino, gluon	$\widetilde{g}$	g	$(\mathbf{8},\ \mathbf{1},\ 0)$
winos, W bosons	$\widetilde{W}^\pm\ \ \widetilde{W}^0$	$W^\pm\ \ W^0$	$(\mathbf{1},\ \mathbf{3},\ 0)$
bino, B boson	$\widetilde{B}^0$	B^0	$(\mathbf{1},\ \mathbf{1},\ 0)$

2.6. The mSUGRA Framework

mSUGRA is derived from Super gravity with minimal super potential and K*ä*hler potential, which guarantees universality of gaugino and scalar masses and of trilinear couplings at a high scale (The CMS Collaboration, 2007). The mSUGRA model of supersymmetry is determined by 5 free parameters defined at the Grand Unification (GUT) scale. The free parameters are:

1. the common scalar mass at GUT scale, m_0,
2. the common gaugino mass at GUT scale, $m_{1/2}$,
3. the common trilinear coupling at the GUT scale, A_0,
4. the sign of the Higgsino mixing parameter, $sign(\mu)$,
5. the ratio of the Higgs vacuum expectation values, $\tan\beta$.

mSUGRA searches are based on the R parity conservation. R parity can be defined as a multiplicative quantum number such that all particles of the SM have R parity +1, while their SUSY partners have -1. R parity can be written as,

$$R \equiv (-1)^{3(B-L)+2S} \tag{2.25}$$

where S is the spin of the particle, B is the Baryon number and L is the Lepton number of the particle. As a result of R parity conservation,

- SUSY partners can only be pair produced from SM particles.
- A theory with R parity conservation will have a lightest SUSY particle (LSP) which is stable.
- The LSP will interact very weakly with ordinary matter.
- A generic signal for R parity conserving SUSY theories is missing transverse energy from the non-observed LSP (Dawson, 1997).

Within the mSUGRA model, the masses of SUSY particles are strongly related to the $m_{1/2}$ and m_0 while the masses of the spin 1/2 SUSY particles are directly related to $m_{1/2}$ (Dittmar, 1999).

2.7. Test Points for mSUGRA at CMS

In order to include the significantly various experimental signatures, a set of mSUGRA test points have been specified and will be used in the subsequent analysis. 14 test points were defined and 10 of them are called low mass points but 9 (LM1 to LM9) test points were chosen to estimate the sensitivity to SUSY signals in the early period of the LHC. Then, some high mass test points (HM1 to HM4) were classified near the final reach of the LHC. The parameters of the test points are shown in Table 2.3 and Figure 2.3 shows their position in the (m_0, $m_{1/2}$) plane. The LM1 test point was chosen in this study.

Table 2.3. mSUGRA parameter values for the test points at CMS.

Point	m_0(GeV/c^2)	$m_{1/2}$(GeV/c^2)	$\tan\beta$	sgn(μ)	A_0
LM1	60	250	10	+	0
LM2	185	350	35	+	0
LM3	330	240	20	+	0
LM4	210	285	10	+	0
LM5	230	360	10	+	0
LM6	85	400	10	+	0
LM7	3000	230	10	+	0
LM8	500	300	10	+	-300
LM9	1450	175	50	+	0
LM10	3000	500	10	+	0
HM1	180	850	10	+	0
HM2	350	800	35	+	0
HM3	700	800	10	+	0
HM4	1350	600	10	+	0

2.8. Decays of Supersymmetric Particles

Before we can discuss signatures via which sparticle production could be detectable at colliders, we need to understand how sparticles decay (Tata, 1997). We will consider in turn the possible decays of neutralinos, charginos, sleptons, squarks and the gluino. If, as is most often assumed, the lightest neutralino $\widetilde{\chi}_1^0$ is the LSP, then all decay chains will end up with it in the final state (Martin, 2006).

2.8.1. Decays of Neutralinos and Charginos

According to the MSSM, neutralinos ($\widetilde{\chi}_i^0$ $(i = 1,2,3,4)$) and charginos ($\widetilde{\chi}_i^{\pm}$ $(i = 1,2)$) can either decay into lighter neutralinos and charginos and gauge or Higgs bosons

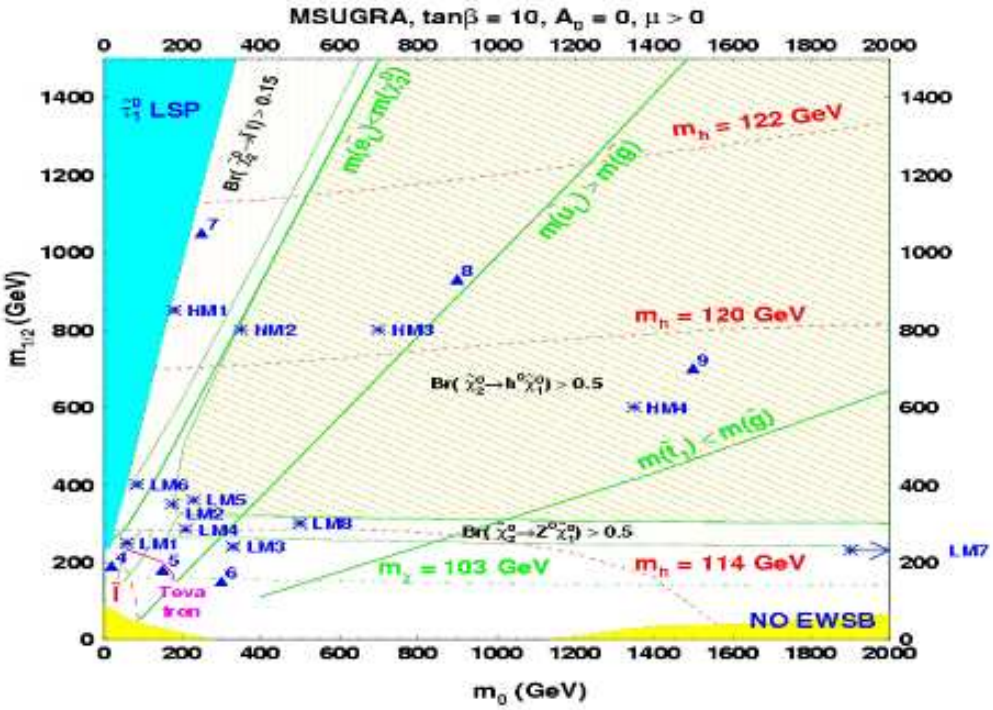


Figure 2.3. Position of the test points in the m_0 versus $m_{1/2}$ plane (The CMS Collaboration, 2007).

or into $f\bar{f}$ pairs if these decays are kinematically allowed (Tata, 1997). If sleptons or squarks are sufficiently light, a neutralino or chargino can therefore decay into lepton-slepton or quark+squark. To the extent that sleptons are probably lighter than squarks, the lepton+slepton final states are favored. A neutralino or chargino plus a Higgs scalar or an electroweak gauge boson, because they inherit the gaugino-higgsino-Higgs and $SU(2)_L$ gaugino-gaugino-vector boson couplings of their components. So, the possible two-body decay modes for neutralinos and charginos in the MSSM are:

$$\widetilde{\chi}_i^0 \to Z\widetilde{\chi}_j^0,\ W\widetilde{\chi}_j^{\mp},\ h^0\widetilde{\chi}_j^0,\ \ell\widetilde{\ell},\ \nu\widetilde{\nu}, \tag{2.26}$$

$$\widetilde{\chi}_i^{\pm} \to W\widetilde{\chi}_j^0,\ Z\widetilde{\chi}_1^{\pm},\ h^0\widetilde{\chi}_1^{\pm},\ \ell\widetilde{\nu},\ \nu\widetilde{l}, \tag{2.27}$$

where ν, l, q for neutrinos, charged leptons and quarks (Martin, 2006). If these two-body decay modes are kinematically forbidden, the charginos or neutralinos have three-body decays through the same gauge bosons, Higgs scalars, sleptons, and squarks that appeared in the two-body decays.

$$\widetilde{\chi}_i^0 \to ff\widetilde{\chi}_j^0,\ \widetilde{\chi}_i^0 \to ff'\widetilde{\chi}_j^{\pm},\ \widetilde{\chi}_i^{\pm} \to ff'\widetilde{\chi}_j^0,\ \widetilde{\chi}_2^{\pm} \to ff\widetilde{\chi}_1^{\pm}, \tag{2.28}$$

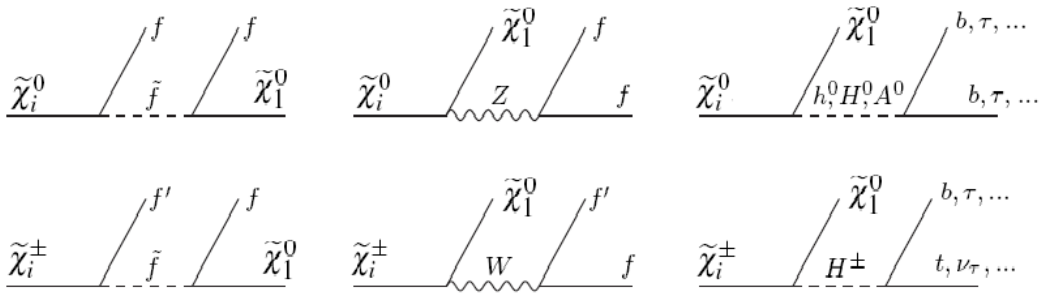


Figure 2.4. Feynman diagrams for neutralino and chargino decay chains with LSP in the final state (Martin, 2006).

In equation 2.28 f refers to a lepton or a quark. f and f' distinct members of the same $SU(2)_L$ multiplet (Martin, 2008). The Feynman diagrams for the neutralino and chargino decays with $\widetilde{\chi}_1^0$ in the final state that seem most likely to be important are shown in Figure 2.4. In many situations, the decays

$$\widetilde{\chi}_1^\pm \to \ell^\pm \nu \widetilde{\chi}_1^0, \quad \widetilde{\chi}_2^0 \to \ell^+ \ell^- \widetilde{\chi}_1^0 \tag{2.29}$$

can be particularly important for phenomenology, because the leptons in the final state often will result in clean signals. In other situations, decays without isolated leptons in the final state. Decays ended with jets and missing transverse energies.

$$\widetilde{\chi}_1^\pm \to jj\widetilde{\chi}_1^0, \quad \widetilde{\chi}_2^0 \to jj\widetilde{\chi}_1^0, \tag{2.30}$$

where j indicates a jet (Martin, 2006).

2.8.2. Slepton Decays

Sleptons can have two-body decays into a lepton and a chargino or neutralino, because of their gaugino admixture, as may be seen directly from the couplings. Therefore, the two-body decays

$$\widetilde{\ell} \to \ell \widetilde{\chi}_i^0, \quad \widetilde{\ell} \to \nu \widetilde{\chi}_i^\pm, \quad \widetilde{\nu} \to \nu \widetilde{\chi}_i^0, \quad \widetilde{\nu} \to \ell \widetilde{\chi}_i^\pm \tag{2.31}$$

can be of weak interaction strength. In particular, the direct decays

$$\widetilde{\ell} \to \ell \widetilde{\chi}_1^0 \quad \text{and} \quad \widetilde{\nu} \to \nu \widetilde{\chi}_1^0 \tag{2.32}$$

are always kinematically allowed if $\widetilde{\chi}_1^0$ is the LSP. However, if the sleptons are sufficiently heavy, then two-body decays can be important.

$$\widetilde{\ell} \to \ell\widetilde{\chi}_1^{\pm}, \quad \widetilde{\ell} \to \ell\widetilde{\chi}_2^0, \quad \widetilde{\nu} \to \nu\widetilde{\chi}_2^0 \text{ and } \quad \widetilde{\nu} \to \ell\widetilde{\chi}_1^{\pm} \tag{2.33}$$

The right-handed sleptons do not have a coupling to the $SU(2)_L$ gauginos, so they typically prefer the direct decay $\widetilde{\ell}_R \to \ell\widetilde{\chi}_1^0$, if $\widetilde{\chi}_1^0$ bino-like. In contrast, the left-handed sleptons may prefer to decay as in equation 2.33 rather than the direct decays to the LSP as in equation 2.32, if the former is kinematically open and if $\widetilde{\chi}_1^{\pm}$ and $\widetilde{\chi}_2^{\pm}$ are mostly wino (Martin, 2006).

2.8.3. Squark Decays

If the decay $\widetilde{q} \to q\widetilde{g}$ is kinematically allowed, it will always dominate, because the quark-squark-gluino vertex has QCD strength. Otherwise, the squarks can decay into a quark plus neutralino or chargino: $\widetilde{q} \to q\widetilde{\chi}_i^0$ or $q'\widetilde{\chi}_i^{\pm}$. The direct decay to the LSP $\widetilde{q} \to q\widetilde{\chi}_1^0$ is always kinematically favored, and for right-handed squarks it can dominate because $\widetilde{\chi}_1^0$ is mostly bino. However, the left-handed squarks may strongly prefer to decay into heavier charginos or neutralinos instead, for example $\widetilde{q} \to q\widetilde{\chi}_2^0$ or $q'\widetilde{\chi}_1^{\pm}$, because the relevant squark-quark-wino couplings are much bigger than the squark-quark-bino couplings (Martin, 2006).

2.8.4. Gluino Decays

Gluinos can only decay through below interactions because they have only strong interactions.

$$\widetilde{g} \to \overline{q}\widetilde{q}_{L,R}, \quad q\bar{\widetilde{q}}_{L,R} \tag{2.34}$$

where the squark may be real or virtual depending on squark and gluino masses. If $m_{\widetilde{g}} > m_{\widetilde{q}}$, $\widetilde{q}_L$ and $\widetilde{q}_R$ are produced in equal numbers in gluino decays. In this case, since $\widetilde{q}_R$ only decays to neutralinos, neutralino decays of the gluino dominate. If, as is more likely, $m_{\widetilde{g}} < m_{\widetilde{q}}$ the squarks in equation 2.34 is virtual and gluinos decay through three body decay

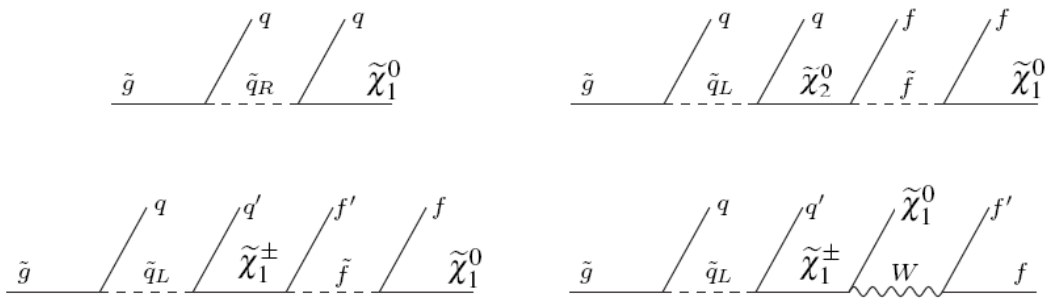


Figure 2.5. Feynman diagrams for gluino decay chains with LSP in the final state (Martin, 2006).

modes,

$$\widetilde{g} \to q\bar{q}\widetilde{\chi}_i^0, \quad q\overline{q'}\widetilde{\chi}_i^{\pm} \tag{2.35}$$

If $m_{\widetilde{g}} < m_{\widetilde{q}}$, gluinos now predominantly decay into charginos because of the large $SU(2)_L$ gauge coupling, and also into neutralino with the largest $SU(2)_L$ gaugino component. Some simplest gluino decays shown in Figure 2.5 (Tata, 1997).

2.9. Signals at Hadron Colliders

The effort to discovery supersymmetry should come to fruition at hadron colliders operating in the present and near future. The Collider Detector at Fermilab (CDF) and DZero detectors at Fermilab Tevatron $p\overline{p}$ collider with $\sqrt{s} = 1.96$ TeV are looking for evidence of sparticles and Higgs bosons. The CERN LHC will continue the search at $\sqrt{s} = 14$ TeV. If supersymmetry is the solution to the hierarchy problem the LHC almost certainly will find direct evidence for it. At hadron colliders, sparticles can be produced in pairs from parton collisions of electroweak strength:

$$q\overline{q} \to \widetilde{\chi}_i^+\widetilde{\chi}_j^-, \quad \widetilde{\chi}_i^0\widetilde{\chi}_j^0, \quad u\widetilde{d} \to \widetilde{\chi}_i^+\widetilde{\chi}_j^0, \quad d\widetilde{u} \to \widetilde{\chi}_i^-\widetilde{\chi}_j^0, \tag{2.36}$$

$$q\overline{q} \to \widetilde{\ell}_i^+\widetilde{\ell}_j^-, \quad \widetilde{\nu}_\ell\widetilde{\nu}_\ell^*, \quad u\widetilde{d} \to \widetilde{\ell}_L^+\widetilde{\nu}_\ell, \quad d\widetilde{u} \to \widetilde{\ell}_L^-\widetilde{\nu}_\ell^*, \tag{2.37}$$

and reactions of QCD strength:

$$\mathsf{gg} \to \widetilde{\mathsf{g}}\widetilde{\mathsf{g}}, \quad \widetilde{q}_i\widetilde{q}_j^*, \tag{2.38}$$

$$\mathsf{g}q \to \widetilde{\mathsf{g}}\widetilde{q}_i, \tag{2.39}$$

$$q\bar{q} \rightarrow \widetilde{\mathsf{gg}}, \quad \widetilde{q}_i\widetilde{q}_j^*, \tag{2.40}$$

$$qq \rightarrow \widetilde{q}_i\widetilde{q}_j, \tag{2.41}$$

The reactions (2.36) and (2.37) get contributions from electroweak vector bosons in the $s-$channel, and those in (2.36) also have $t-$channel squark-exchange contributions that are of lesser importance in most models. The process in $(2.38) - (2.41)$ get contributions from the $t-$exchange of an appropriate squark or gluino, and (2.38) and (2.40) also have gluon $s-$channel contributions (Martin, 2006). At the Tevatron collider, the chargino and neutralino production processes (mediated primarily by valence quark annihilation into virtual weak bosons) tend to have the larger cross-sections, unless the squarks or gluino are rather light (less than 300 GeV or so). In a typical model where $\widetilde{\chi}_1^{\pm}$ and $\widetilde{\chi}_2^0$ are mostly $SU(2)_L$ gauginos and $\widetilde{\chi}_1^0$ is mostly bino, the largest production cross-section in (2.36) belong to the $\widetilde{\chi}_1^+\widetilde{\chi}_1^-$ and $\widetilde{\chi}_1\widetilde{\chi}_2^0$ channels, because they have significant couplings to γ, Z and W bosons, respectively, and because of kinematics. At the LHC, the situation is typically reversed, with production of gluinos and squarks by gluon-gluon and gluon-quark fusion usually dominating, unless the gluino and squarks are heavier than 1 TeV or so.

The decays of the produced sparticles result in final states with two neutralino LSPs, which escape the detector. The LSPs carry away at least $2\mathrm{m}_{\widetilde{\chi}_1^0}$ of missing energy, but at hadron colliders only the component of the missing energy that is manifest in momenta transverse to the colliding beams (denoted E_T^{miss} or MET) is observable. So in general the observable signals for supersymmetry at hadron colliders are n leptons + m jets + E_T^{miss}, where either n or m might be 0. There are important Standard Model backgrounds to many of these signals, especially from processes involving production of W and Z bosons that decay to neutrinos, which provide the E_T^{miss}. Therefore it is important to identify specific signals for which backgrounds can be reduced (Martin, 2006).

3. THE LHC AND THE CMS DETECTOR

A general overview of the Large Hadron Collider (LHC) project will be presented and then Compact Muon Solenoid (CMS) experiment will be discussed in this chapter.

3.1. The Large Hadron Collider

The Large Hadron Collider is a two-ring-superconducting-hadron accelerator and collider installed in the existing 26.7 km tunnel that was constructed between 1984 and 1989 for the CERN LEP machine (Evans and Bryant, 2008). The LHC is the most powerful proton-proton accelerator machine for Particle Physics research and a satellite view of the LHC is shown in Figure 3.1. The radius of the LHC circle is approximately 4.3 km. The proton-proton beams will collide at $\sqrt{s} = 14$ TeV center of mass energy to discover new particles and to investigate new physics which can become visible on a mass scale of the order of 1 TeV. The design luminosity of the LHC is 10^{34} cm^{-2}s^{-1}. To deliver this luminosity, the time differences between two proton bunches is only 25 ns in other words the proton bunches will only be 7.5 m apart. There are 2835 proton-proton bunches per beam and around 10^{11} protons in each bunch (shown in Figure 3.2). Hence, it needs very fast readout electronics and trigger decisions. The LHC is built in the LEP collider tunnel which was built before with some developments which have been done to accelerate the protons in the tunnel. The protons will accelerate up to 50 MeV in a linear accelerator (Linac), a Booster up to 1.4 GeV, the PS up to 25 GeV and the SPS up to 450 GeV. Finally, protons will be injected into the LHC where they will reach to 7 TeV and then protons will collide at the detectors of LHC (shown in Figure 3.3). There are four detectors built in the LHC tunnel: A Toroidal LHC Apparatus (ATLAS), Large Hadron Collider beauty (LHCb), Compact Muon Solenoid (CMS) and A Large Ion Collider Experiment (ALICE).

The main goal of the LHC is to clarify the nature of electroweak symmetry breaking for which the Higgs mechanism is assumed to be responsible. The experimental study of the Higgs mechanism can also shed light on the mathematical consistency of the Standard Model at energy scales above about 1 TeV. Various alternatives to the Standard Model invoke new symmetries, new forces or constituents. Furthermore, there are high hopes

for discoveries that could pave the way toward a unified theory. These discoveries could take the form of SUSY or try extra dimensions, the latter often requiring modification of gravity at the TeV scale. Hence there are many compelling reasons to investigate the TeV energy scale. The LHC will also provide high-energy heavy-ion beams at energies over 30 times higher than at the previous accelerators, allowing us to further extend the study of QCD matter under extreme conditions of temperature, density, and parton momentum fraction (low-x).

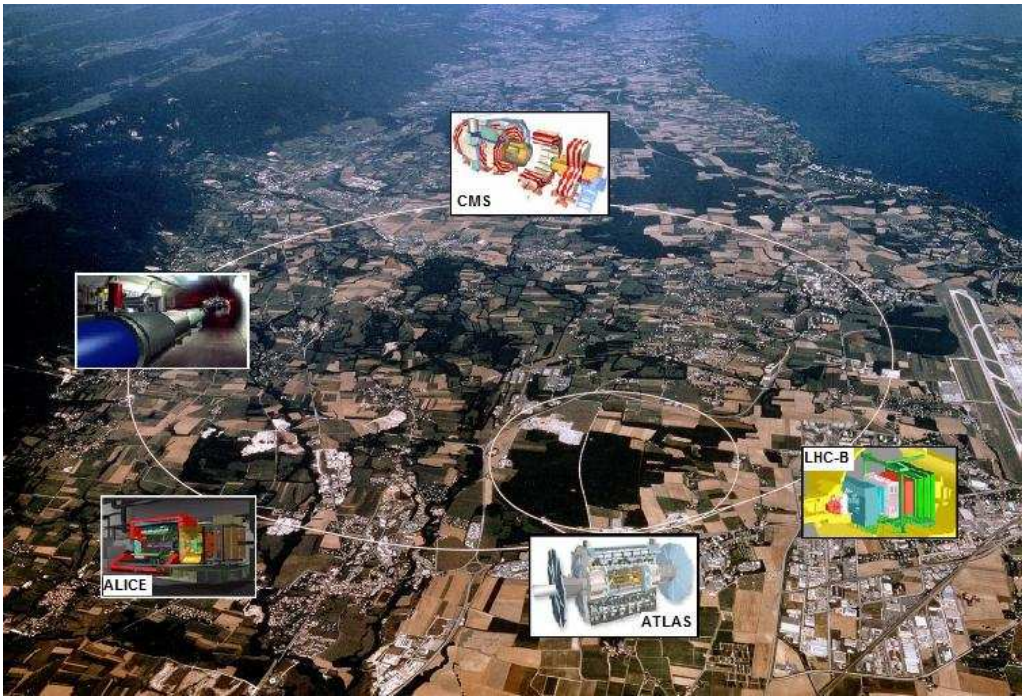


Figure 3.1. A satellite view of CERN LHC collider.

3.2. Compact Muon Solenoid

The Compact Muon Solenoid detector is compact because it is ”small” for its stupendous weight (12500 tons), muon for one of the particles it detects, and solenoid for the coil inside its huge superconducting magnet. There are two main goals of CMS detector one is to find the Higgs boson and the other one is to search for physics beyond the Standard Model which is generally considered to be SUSY. To attain these goals, it was designed to detect a wide range of particles and phenomena produced in high-energy collisions in the LHC. CMS was installed 100 meters underground close to the French vil-

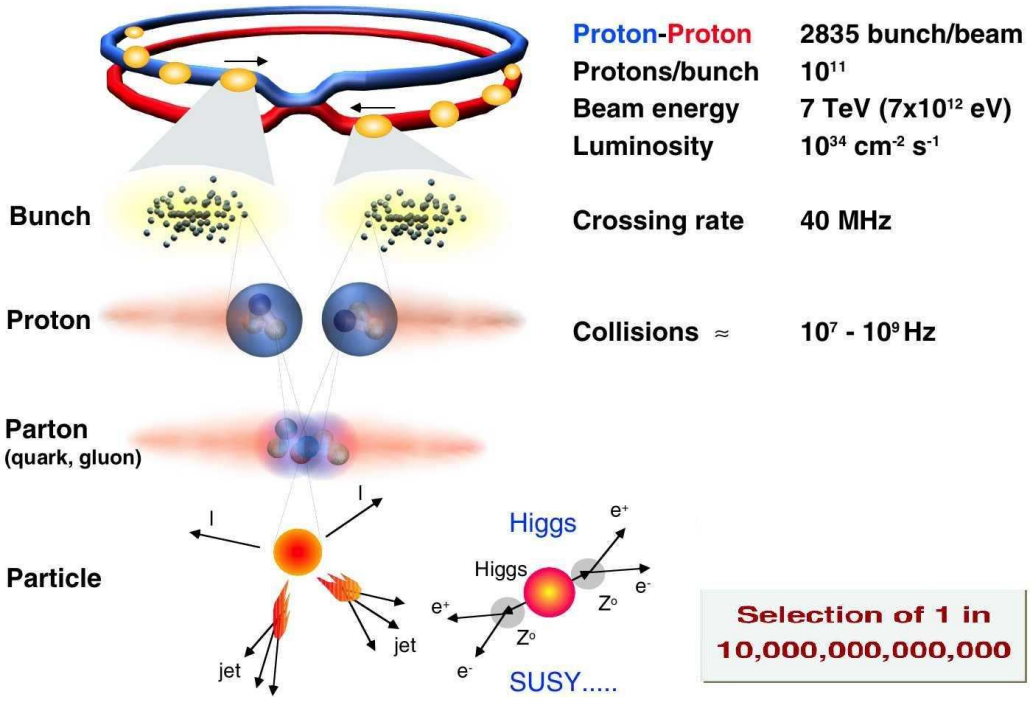


Figure 3.2. CERN LHC collision (Smith, 2008).

lage of Cessy, between Lake Geneva and the Jura mountains. Figure 3.4 shows the overall layout of the CMS detector. For the proton-proton collisions at $\sqrt{s} = 14$ TeV the total cross-section is expected to be roughly 100 mb. Observe an event rate approximately 10^9 inelastic events/s at the general-purpose detectors such a CMS at design luminosity. This causes a number of dreadful experimental challenges. This huge event rate must be reduced to about 100 events/s for storage and analysis by the online event selection process (trigger). One of the major problem for the design of the read-out and trigger systems is the short time between bunch crossings. An average of about 20 inelastic collisions will overlap on the event of interest at the design luminosity. This means that around 1000 charged particles will be produced from the interaction region every 25 ns. The particles of a collision under study may be confused with those from other collisions in the same bunch crossing. This problem clearly becomes more serious when a detector element and its electronic signal response time is more than 25 ns. Using high-granularity detectors with good time resolution can decrease the effect of this pile-up. To overcome this problem millions of detector channels are needed. The millions of detector electronic channels require very good synchronization. There are high radiation levels due to the large flux of particles coming from the interaction region, needing radiation-hard detectors and front-

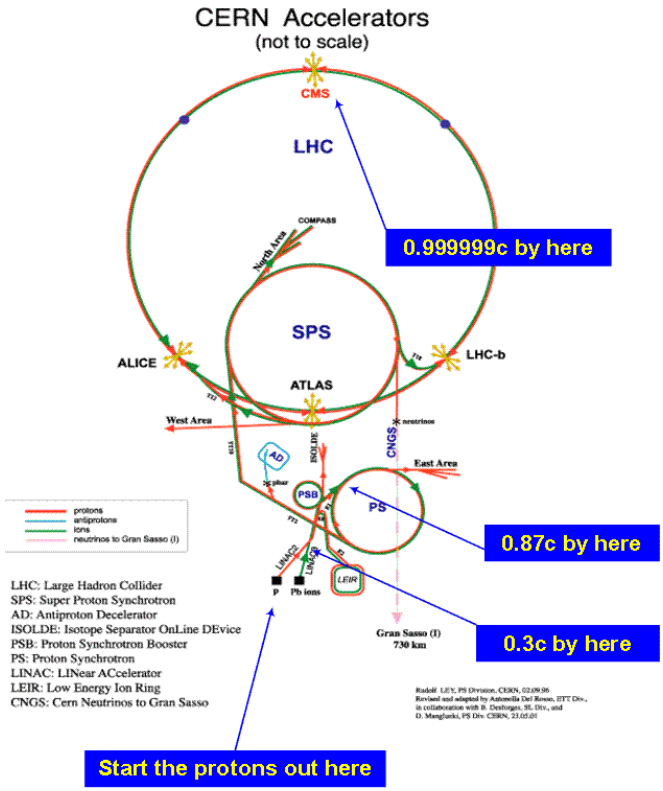


Figure 3.3. CERN LHC collider.

end electronics. CMS detector requirements for the goals of the LHC physics programme can be abstracted as follows:

- Good muon identification and momentum resolution over a wide range of momenta and angles, good dimuon mass resolution ($\approx 1\%$ at 100 GeV), and the ability to determine unambiguously the charge of muons with $p < 1$ TeV;

- Good charged particle momentum resolution and reconstruction efficiency in the inner tracker. Efficient triggering and offline tagging of τs and b-jets, requiring pixel detectors close to the interaction region;

- Good electromagnetic energy resolution, good di-photon and di-electron mass resolution (≈ 1 % at 100 GeV), wide geometric coverage, π^0 rejection, and efficient photon and lepton isolation at high luminosities;

- Good missing-transverse-energy and di-jet-mass resolution, requiring hadron calorimeters with a large hermetic geometric coverage and with fine lateral segmentation.

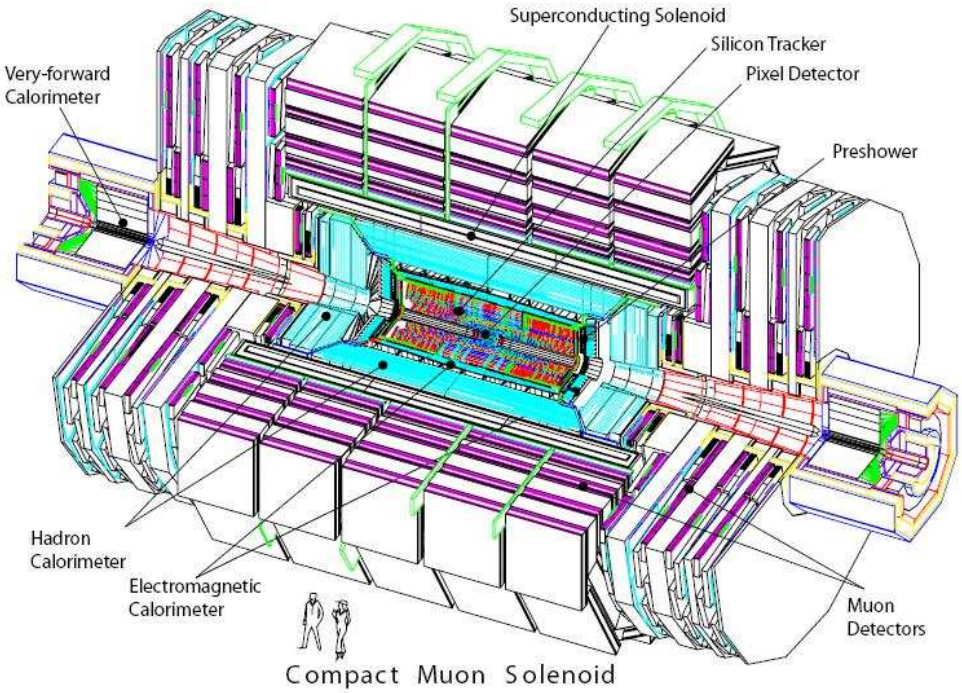


Figure 3.4. A perspective view of the CMS detector (The CMS Collaboration, 2008).

The coordinate system of the CMS is the y-axis pointing vertically upward, and the x-axis pointing radially inward toward the center of the LHC. Thus, the z-axis shows along the beam direction toward the Jura mountains from LHC Point 5. The azimuthal angle ϕ is measured from the x-axis in the x-y plane and the radial coordinate in this plane is indicated by r. The polar angle θ is measured from the z-axis. Pseudorapidity is defined as $\eta = -\ln\tan(\theta/2)$. Thus, the momentum and energy transverse to the beam direction, indicated by p_T and E_T , respectively, are computed from the x and y components. Missing Transverse Energy is the imbalance of energy measurement in the transverse plane (The CMS Collaboration, 2008).

3.2.1. The Inner Tracker

The aim of the inner tracker is to provide a precise and efficient measurement of the trajectories of the charged particles generated from the collisions. It covers the interaction point and length and diameter of the system are 5.8 and 2.5 m, respectively. A homogeneous magnetic field, 4 Tesla, over the full volume of the tracker is provided by

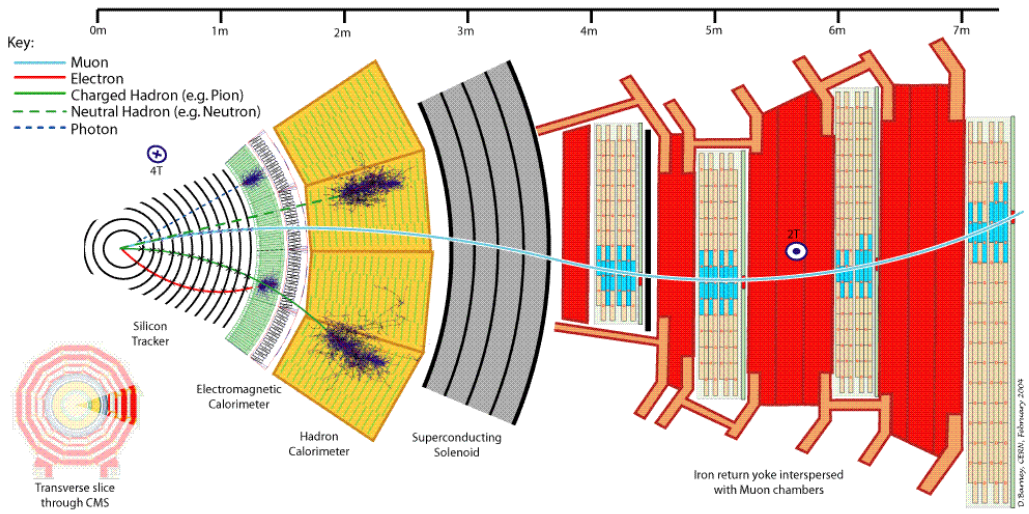


Figure 3.5. CMS View.

the CMS solenoid. A mean about 1000 particles from more than 20 overlapping proton-proton interactions crossing the tracker for every 25 ns at the design luminosity. Hence, tracker detector needs to be high granularity and fast response.

The CMS tracker consists of a pixel detector with three barrel layers at radii between 4.4 cm and 10.2 cm and a silicon strip tracker with 10 barrel detection layers extending out wards to a radius of 1.1 m. Each system is ended by end caps which include 2 disks in the pixel detector and 3 plus 9 disks in the strip tracker on each side of the barrel. Coverage of the tracker is up to a pseudorapidity of $|\eta| < 2.5$. The CMS tracker which has about 200 m^2 of active silicon area is the largest silicon tracker ever built. Tracker system of the CMS has 1440 pixel and 15148 strip detector modules.

The pixel system which is the part of the tracking system is the closest to the interaction region. It provides precise tracking points in $r-\phi$ and z plane and hence is responsible for a small impact parameter resolution that is important for good secondary vertex reconstruction. With a pixel size of 100×150 μm^2 emphasis has been put on accomplishing similar track resolution in both $r-\phi$ and z directions. Due to this a 3D vertex reconstruction is possible, which will be important for secondary vertices with low track multiplicity (The CMS Collaboration , 2008).

3.2.2. Electromagnetic Calorimeter (ECAL)

The Electromagnetic Calorimeter (ECAL) which consists of 61200 lead tungstate ($PbWO_4$) crystals mounted in the Electromagnetic Barrel (EB), ended by 7324 crystals in each of the two Electromagnetic endcaps (EE) is a hermetic homogeneous calorimeter of CMS. The properties of the $PbWO_4$ crystals make them an adequate selection for operation at LHC. The ECAL is a fine granularity and a compact calorimeter because the high density (8.28 g/cm^3), short radiation length (0.89 cm) and small Molière radius (2.2 cm). These kind of crystals has the scintillation decay time of the same order of magnitude as the LHC bunch crossing time: about 80% of the light is emitted in 25 ns. A preshower detector is placed in front of the endcap crystals. Avalanche photodiodes (APDs) are used as photodetectors in the barrel and vacuum phototriodes (VPTs) in the endcaps. The use of high density crystals has admitted the design of a calorimeter which is fast, has fine granularity and is radiation resistant. The EB of the ECAL covers the pseudorapidity range $|\eta| < 1.479$. The crystal cross-section corresponds to approximately 0.01740×0.0174 in η-ϕ space or 22×22 mm^2 at the front face of crystal, and 26×26 mm^2 at the rear face. The crystal length is 230 mm corresponding to 25.8 X_0. The barrel crystal volume is 8.14 m^3 and the weight is 67.4 t.

The EE covers the pseudorapidity from 1.479 to 3.0. The longitudinal distance between the interaction point and the outer surface of the EE is 315.4 cm. The crystals have a rear face surface area 30×30 mm^2, a front face surface area 28.62×28.62 mm^2 and a length of 220 mm (24.7 X_0). The EE crystal volume is 2.90 m^3 and the weight is 24.0 t.

The Preshower is a sampling calorimeter with two layers: lead radiators initiate electromagnetic showers from incoming photons/electrons whilst silicon strip sensors placed after each radiator measure the deposited energy and the transverse shower profiles. The total thickness of the Preshower is 20 cm. The principal aim of the CMS Preshower detector is to identify neutral pions in the endcaps within a fiducial region $1.653 < |\eta| < 2.6$. It also helps the identification of electrons against minimum ionizing particles, and improves the position determination of electrons and photons with high granularity. Figure 3.6 shows the layout of the CMS electromagnetic calorimeter (The

CMS Collaboration, 2008).

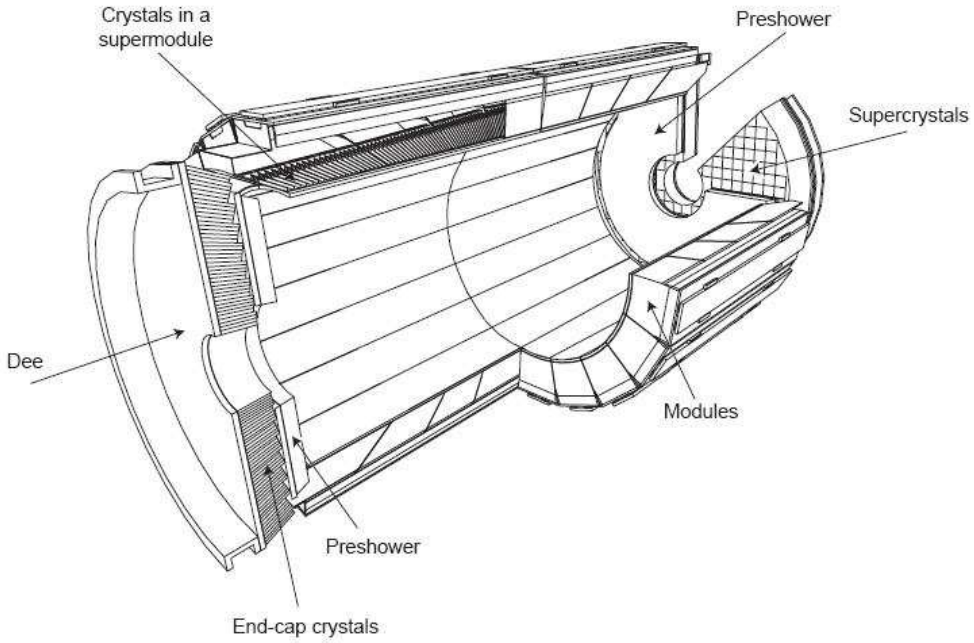


Figure 3.6. Layout of the CMS electromagnetic calorimeter (The CMS Collaboration, 2008).

3.2.3. Hadronic Calorimeter (HCAL)

The main goal of the hadron calorimeters is to observation of hadron jets and neutrinos or exotic particles due to measured energy imbalance in the calorimeters. The hadron calorimeter barrel (HB) and end caps (EB) are placed behind the tracker and the electromagnetic calorimeter as seen from the interaction point. The Hadron calorimeter barrel is radially constrained between the outer extension of the electromagnetic calorimeter (R=1.77 m) and the inner extension of the magnet coil (R=2.95 m). This restricts the total amount of material which can be put into absorb the hadronic shower. Therefore, an outer hadron calorimeter or tail catcher is positioned outside the solenoid complementing the barrel calorimeter. Beyond $|\eta|$=3, the forward hadron calorimeters placed at 11.2 m from the interaction point extend the pseudorapidity coverage down to $|\eta|$=5.2 using a Cherenkov-based, radiation-hard technology. Figure 3.7 shows the longitudinal view of the CMS detector. The dashed lines are at fixed $|\eta|$ values.

The **HB** consists of 36 identical azimuthal wedges which form the two half-barrels

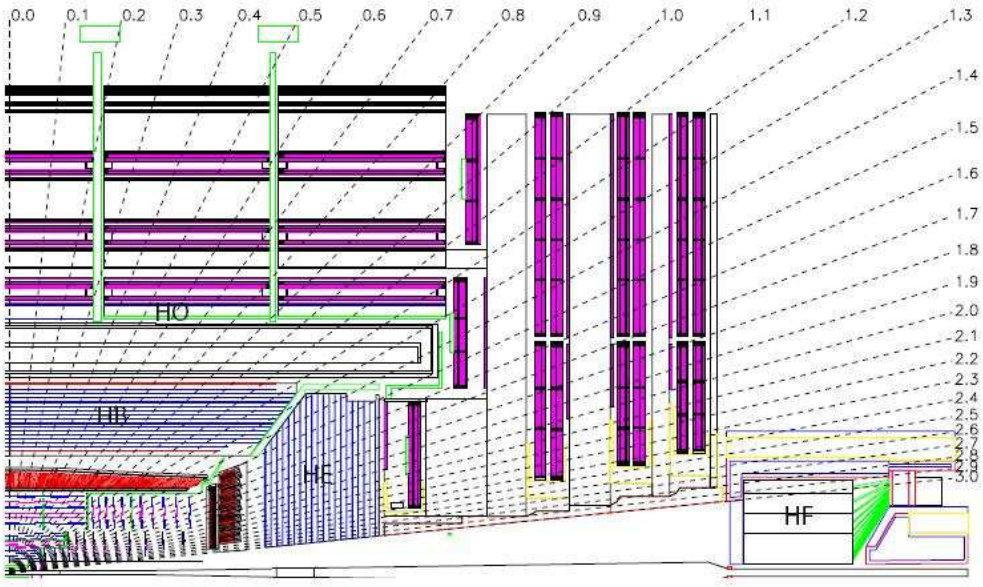


Figure 3.7. Longitudinal view of the CMS detector showing the locations of the HB, HE, HO and HF calorimeters (The CMS Collaboration, 2008).

(HB+ and HB−). The wedges are constructed out of flat brass absorber plates aligned parallel to the beam axis. Each wedge is segmented into four azimuthal angle (ϕ) sectors. The plates are bolted together in a staggered geometry resulting in a configuration that contains no projective dead material for the full radial extent of a wedge. The innermost and outermost plates are made of stainless steel for structural strength. The plastic scintillator is divided into 16 η sectors, resulting in a segmentation ($\Delta\eta$, $\Delta\phi$)=(0.087, 0.087). The wedges are themselves bolted together, in such a fashion as to minimize the crack between the wedges to less than 2 mm. The absorber consist of a 40 mm thick front steel plate, followed by eight 50.5 mm thick brass plates, six 56.5 mm thick brass plates, and a 75 mm thick steel back plate. The total absorber thickness at 90° is 5.82 interaction lengths (λ_I). The HB effective thickness increases with polar angle (θ) as $1/\sin\theta$, resulting in 10.6 λ_I at η=1.3. The active medium uses the well known tile and wavelength shifting fibre concept to bring out the light. The CMS hadron calorimeter consists of about 70000 tiles. In order to limit the number of individual elements to be handled, the tiles of a given ϕ layer are grouped into a single mechanical tray unit. The tray geometry has allowed for construction and testing of the scintillators remote from the experimental installation area.

The hadron calorimeter endcaps (**HE**) cover a substantial portion of the rapidity

range, $1.3<|\eta|<3$, a region containing about 34% of the particles produced in the final state. The high luminosity of the LHC (10^{34} cm^{-2}s^{-1}) requires HE to handle high (MHz) counting rates and have high radiation tolerance (10 MRad after 10 years of operation at design luminosity) at $\eta \simeq 3$. Since the calorimeter is inserted into the ends of a 4-T solenoidal magnet, the absorber must be made from a non-magnetic material. The endcaps are placed to the muon endcap yoke. The scintillation light is collected by wavelength shifting (WLS) fibres. The design minimizes dead zones because the absorber can be made as a solid piece without supporting structures while at the same time the light can be easily routed to the photodetectors. The ends of the fibres are machined with a diamond fly cutter and one end is covered with aluminium to increase the light collection. The other end is spliced to a clear fibre, which is terminated in an optical connector. The connector with the glued fibres is also machined by a diamond fly cutter. The scintillator is painted along the narrow edges and put into a frame to form a tray. The total number of tiles for both HE calorimeters is 20916 and the number of trays is 1368. The granularity of the calorimeters is $\Delta\eta \times \Delta\phi = 0.087 \times 0.087$ for $|\eta| < 1.6$ and $\Delta\eta \times \Delta\phi = 0.17 \times 0.17$ for $|\eta| \geq 1.6$.

The hadron outer calorimeter (**HO**) is extended outside the solenoid with a tail catcher. In the central pseudorapidity region, the combined stopping power of EB plus HB does not provide sufficient containment for hadron showers. The HO utilises the solenoid coil as an additional absorber equal to $1.4/\sin\theta$ interaction lengths and is used to identify late starting showers and to measure the shower energy deposited after HB.

The forward calorimeter (**HF**) will experience unprecedented particle fluxes. On average, 760 GeV per proton-proton interaction is deposited into the two forward calorimeters, compared to only 100 GeV for the rest of the detector. Moreover, this energy is not uniformly distributed but has a pronounced maximum at the highest rapidities. At $\eta = 5$ after an integrated luminosity of 5×10^5 pb^{-1} ($\approx$ 10 years of LHC operation), the HF will experience $\approx$ 10 MGy. The charged hadron rates will also be extremely high. Quartz fibres were chosen as the active medium for HF because it needs to be survived from harsh conditions (The CMS Collaboration, 2008).

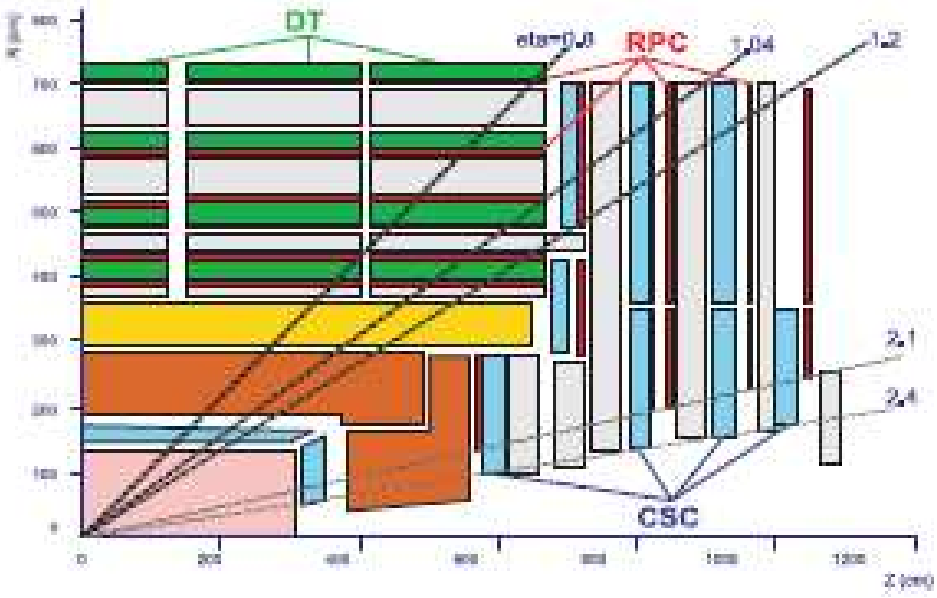


Figure 3.8. Layout of the CMS muon system (Liu. C, Neumeister. N, 2008).

3.2.4. Muon System

The CMS muon system is performed to have the capability of reconstructing the muon and charge of muons over all the kinematic range of the LHC. There are 3 types of gaseous particle detectors for muon identification in the CMS. Because of the shape of the solenoid magnet, the muon system was naturally built to have a cylindrical, barrel section and 2 planar endcap regions. Since the muon system is composed of about 25 000 m^2 of detection surface, the muon chambers had to be cheaper, credible, and robust. Schematic view of the muon system is shown in Figure 3.8. The barrel drift tube (DT) chambers cover the pseudo-rapidity region $|\eta| < 1.2$ and are organized into 4 segments distributed among the layers of the flux return plates. The first three stations each contains 8 chambers, in 2 groups of 4, which measure the muon coordinate in the $r-\phi$ bending plane, and 4 chambers which provide a measurement in the z direction, along the beam line. The fourth station does not contain the z-measuring planes. In this region, where the neutron-induced background is small, the muon rate is low, and the 4-T magnetic field is uniform.

The muon system uses cathode strip chambers (CSC) in the 2 endcap regions where

the muon rates and background levels are high and the magnetic field is large and non-uniform. Because of their quick response time, fine segmentation, and radiation resistance, the muons are detected by the CSCs between $|\eta|$ values of 0.9 and 2.4. CSCs have 4 stations in each endcap, with chambers positioned perpendicular to the beam line and distributed between the flux return plates. Each 6-layer of CSC provides reliable pattern recognition for rejection of non-muon backgrounds and efficient matching of hits to those in other stations and to the CMS inner tracker.

Because of the uncertainty in the possible background rates and in the ability of the muon system to measure the correct beam-crossing time when the LHC reaches full luminosity, a complementary, dedicated trigger system consisting of resistive plate chambers (RPC) was added in both the barrel and endcap regions. The RPCs support a fast, independent, and highly-segmented trigger with sharp p_T threshold over a large fraction of the rapidity range ($|\eta| < 1.6$) of the muon system. The RPCs are double-gap chambers, operated in avalanche mode to ensure good operation at high rates. They generate a fast response, with good time resolution but coarser position resolution than the DTs or CSCs. They also help to resolve ambiguities in attempting to make tracks from multiple hits in a chamber (The CMS Collaboration, 2008).

3.3. The CMS Magnet-Superconducting Solenoid

The length and diameter of the superconducting solenoid are 12.5 m and 6 m, respectively. It has been designed to reach a 4 T magnetic field with a stored energy of 2.6 GJ at full current. The flux is returned through a 10000 t yoke covering 5 wheels and 2 endcaps, consisting of three disks each. There is a large mechanical deformation (0.15%) during energizing due to the ratio between stored energy and cold mass being high (11.6 KJ/kg). Figure 3.9 shows the values of E/M as a function of stored energy for several detector magnets. The superconducting solenoid of CMS has three new properties of the superconducting solenoid with regard to previous detector magnets:

- Due to the number of ampere-turns required for generating a field of 4 T (41.7 MA-turn), the winding is composed of 4 layers, instead of the usual 1 or maximum 2 layers.

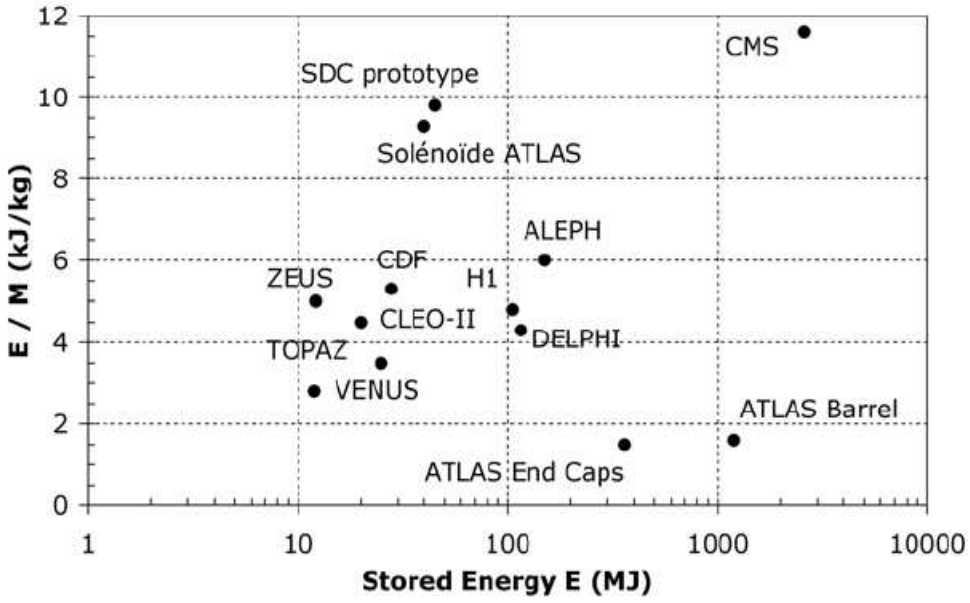


Figure 3.9. The energy over mass ratio E/M, for several detector magnets (The CMS Collaboration, 2008).

- The conductor, made from a Rutherford-type cable co-extruded with pure aluminium, is mechanically reinforced with an aluminium alloy;
- The dimensions of the solenoid are very large (6.3 m cold bore, 12.5 m length and 220 tons mass) (The CMS Collaboration, 2008).

3.4. Triggers

Proton-proton and heavy-ion collisions will occur at high interaction rates at the LHC. For protons the beam crossing interval is 25 ns, corresponding to a frequency of 40 MHz. Depending on luminosity, several collisions occur at each crossing of the proton bunches (approximately 20 simultaneous p-p collisions at the nominal design luminosity of 10^{34} cm^2s^{-1}). It is not possible to store and process the large amount of data which is produced due to high number of events, an extreme rate reduction has to be performed. This task is done by the trigger system, which is the start of the physics event selection process. There are two steps in CMS to reduce rate Level-1 Trigger (L1T) and High-Level Trigger (HLT), respectively. Figure 3.10 shows the schematic view of the CMS trigger system.

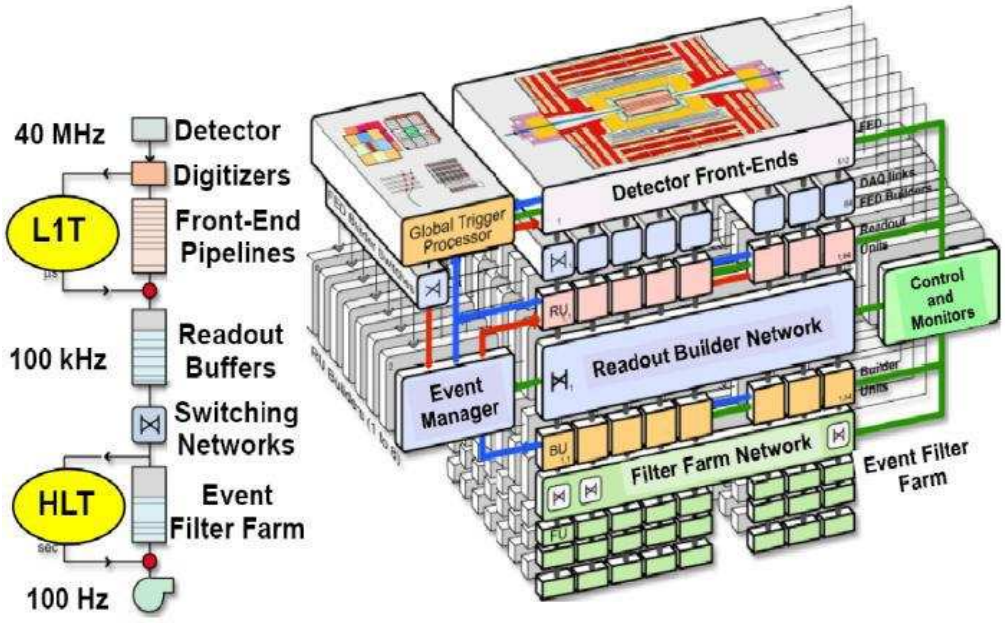


Figure 3.10. Schematic view of the CMS trigger system (Felcini, 2008).

The Level-1 Trigger is composed of custom-designed, mostly programmable electronics, whereas the HLT is a software system implemented in a filter farm of about one thousand commercial processors. The rate reduction capability is designed to be at least a factor of 10^6 for the combined L1 Trigger and HLT. The design out put rate limit of the L1 Trigger is 100 kHz, which translates in practice to a calculated maximal output rate of 30 kHz, assuming an approximate safety factor of three. The L1 Trigger uses coarsely portioned data from the calorimeters and the muon system, while holding the high-resolution data in pipelined memories in the front-end electronics. The HLT has access to the complete read-out data and can thus perform complex calculations similar to those made in the off-line analysis software if required for specially interesting events. The L1 Trigger has local, regional and global components. At the bottom end, the Local Triggers, also called Trigger Primitive Generators (TPG), are based on energy deposits in calorimeter trigger towers and track segments or hit patterns in muon chambers, respectively. Regional Triggers combine their information and use pattern logic to determine ranked and sorted trigger objects such as electron or muon candidates in limited spatial regions. The rank is determined as a function of energy or momentum and quality, which reflects the level of confidence attributed to the L1T parameter measurements, based on detailed knowledge of the detectors and trigger electronics (The CMS Collaboration, 2008).

4. RESPONSE COMPARISON OF THE CMS CALORIMETERS TO PIONS BETWEEN MONTE CARLO AND TEST BEAM

4.1. Introduction

In this chapter, comparison of energy response for CMS electromagnetic (EB) and hadronic barrel (HB) calorimeters to single pions from Test Beam 2006 (TB2006) data and Monte Carlo (MC) is discussed.

4.2. Test Beam Setup, Beam Clean-up and Particle Identification

The tests of the combined CMS electromagnetic barrel (EB) and hadronic barrel (HB) calorimeter system were performed at the H2 beam line at the CERN SPS. Figure 4.1 shows the H2 beam line and the experimental setup. The beam line is designed to operate in two different modes, high energy and very low energy (VLE) modes. In the high energy mode, different kinds of particles are created when 400 GeV/c protons from the Super Proton Synchrotron (SPS) strike a production target (T2) 590.9 m upstream of the calorimeters and momenta of particles range between 10 GeV/c to 350 GeV/c. In the very low energy mode, an additional target (T22) positioned at 97.0 m is used for particle generation and the momenta of particles are restricted to 1 to 9 GeV/c. In the high energy

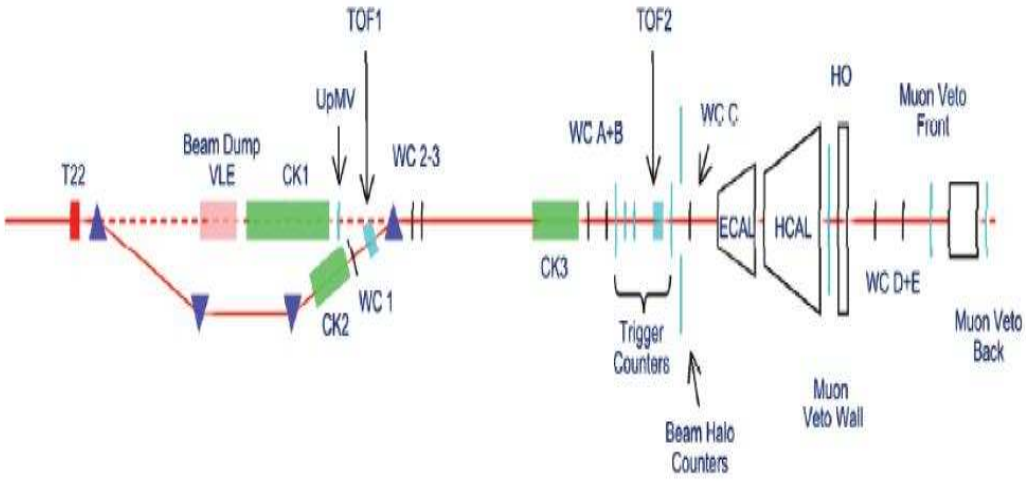


Figure 4.1. The CERN H2 beam line and the experimental setup (Akchurin et. al, 2007).

mode, the T22 target and the VLE beam dump were removed from the beam line. The maximum beneficial momentum of beam was 100 GeV/c for electrons and 350 GeV/c for hadrons. In the VLE mode, two Cherenkov counters (CK2 and CK3), two time-of-flight counters (TOF1 and TOF2) and muon counters (Muon Veto Wall, Muon Veto Front and Muon Veto Back) enabled us to positively tag electrons, charged pions and kaons, protons, antiprotons and muons. CK2 is a 1.85 m long Cherenkov counter filled with CO_2 and was used to identify electrons in the VLE mode. CK3 is also 1.85 m long and was filled with Freon134a.

Time-of-flight counters (TOF1 and TOF2) were separated by $\sim$55 m. Each scintillator plate measured 10×10 cm^2 in area and was 2 cm thick. Two trapezoidal shaped air-core light guides on either side of the plate funneled the scintillation light to two fast photomultiplier tubes (R5900). The analog pulses were discriminated by constant fraction discriminators and the time resolution was $\sim$300 ps. Protons were well-separated from pions (and kaons) up to 7 GeV/c with this time-of-flight system alone.

Energetic muons were tagged with Muon Veto Front (MVF) and Muon Veto Back (MVB) as well as the Muon Veto Wall (MVW) counters. MVF and MVB were large (80×80 cm^2) scintillation counters and were placed well behind the calorimeters. In order to filter out the soft muon component in the beam line, an 80 cm thick iron block was inserted in front of MVB. MVW consisted of 8 individual scintillation counters, each measuring 30×100 cm^2, placed closely behind the HB. These counters were positioned horizontally with a 2 cm overlap between them, hence covering a region of 226 cm in the vertical and 100 cm in the horizontal directions.

In addition to the afore-mentioned particle ID detectors, six delay-line chambers (WC1 through WC3 upstream and WCA through WCC downstream), four scintillation counters (S1 through S4) for triggering and four scintillation beam halo counters (BH1 through BH4) were used in the experiment. The spatial resolution afforded by the delay-line chambers was $\sim$350 μm in both x- and y-coordinates. The beam trigger typically consisted of the coincidence S1.S2.S4 which defined a 4×4 cm^2 area on the front face of the calorimeter. S4 counter was used to eliminate multi-particle events off-line since it gave a clean pulse height distribution of single and multiple particles in the beam. Four BH counters, each measuring 30×100 cm^2, were arranged such that the beam passed

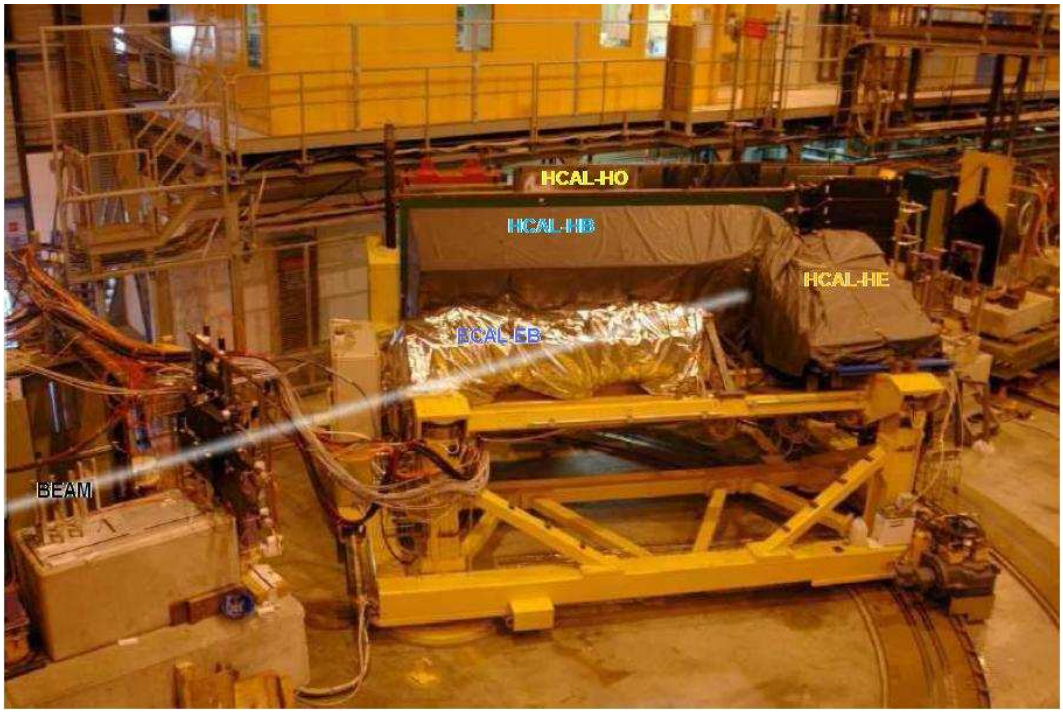


Figure 4.2. EB, HB, HE and HO on the rotatable table. The white line represents the beam.

through a 7×7 cm^2 opening. These counters were effective in vetoing the beam halo and large-angle particles that originated from interactions in the beam line.

The HCAL part of the calorimeter system consisted of two HB wedges (HB1 and HB2) corresponding to 8 segments covering 40 degrees in azimuth, and the Outer Barrel Calorimeter HO. The ECAL part used in the test beam is one of the 36 super modules, namely SM9. Both ECAL and HCAL detectors were equipped with the final CMS production electronics. The entire calorimeter system was placed on a rotatable table whose pivot mimics the interaction point at the LHC. The calorimeters were placed on the rotatable table and are shown in Figure 4.2.

To get a clean beam, only single-hit events in the scintillators S1,S2 and S4 were used in trigger. Moreover, beam halo events and wide-angle secondaries were removed using the beam halo counters (BH1-4). VMB was used in later analysis to tag the muons in the high energy beam. To identify the muons in the low energy beam configuration (VLE) VMB, VMF and the muon veto counters (VM1-8) were utilized. At low beam momentum, electron contamination in the pion beam was dominant. Therefore, in addition to CK2, which was dedicated to electron tagging at VLE, also CK3 was used to remove

the electrons in the pion beam since CK3 could identify pions down to 4 or 5 GeV/c, depending on the pressure setting used during the data taking. Protons/antiprotons and kaons in the pion beam were identified using time-of-flight counters and CK3. HCAL and ECAL rechits were used for energy reconstruction. A rechit is the energy in a cell of the calorimeter in units of GeV. Energy was collected in $\eta \times \phi = 4 \times 3$ towers for HB, while 3×2 towers were used for HO and 7×7 crystals were used for EB.

4.3. Local Clustering and Monte Carlo Data Sets

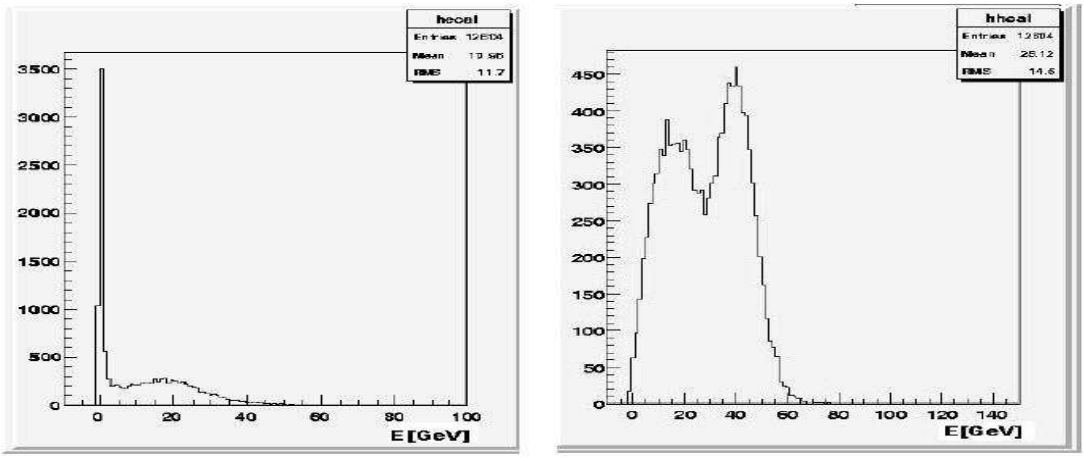
In order to make local clusters midpoint cone (MCone) algorithm was used. The midpoint cone algorithm also uses an iterative procedure to find stable cones (proto-jets) starting from the cones around objects with an E_T above a seed threshold. For every pair of proto-jets that are closer than the cone diameter, a midpoint is calculated as the direction of the combined momentum. These midpoints are then used as additional seeds to find more proto-jets. When all proto-jets are found, the splitting and merging procedure is applied, starting with the highest E_T proto-jet. If the proto-jet does not share objects with other proto-jets, it is defined as a jet and removed from the proto-jet list. Otherwise, the transverse energy shared with the highest E_T neighbor proto-jet is compared to the total transverse energy of this neighbor proto-jet. If the fraction is greater than f (typically 50%) the proto-jets are merged, otherwise the shared objects are individually assigned to the proto-jet that is closest in η, ϕ space. The procedure is repeated, again always starting with the highest E_T proto-jet, until no proto-jets are left. Algorithm parameters are a seed threshold, a cone radius, a threshold f on the shared energy fraction for jet merging, and a maximum number of proto-jets. The particles generated in a cone of radius R in the (η,ϕ) plane at the production vertex are clustered in a "generator" jet. "Calorimetric" jets are reconstructed in the calorimeters within a cone of radius R_{reco} in the $(\eta,\ \phi)$ plane. Radius of clusters are 0.07 and 0.15 for electromagnetic and hadronic calorimeters, respectively. Electromagnetic cluster radius is approximately covers to 7×7 crystals in EB and hadronic cluster radius is approximately covers to 3×3 hadronic towers. Hadronic towers also included HO.

Pythia based particle gun was used to generate particles and detector simulated with

GEometry ANd Tracking (GEANT). Single pions were generated at fix η and ϕ points. The generated pions strike tower 3 region and very tiny area so most of the incident beam energy deposited in one tower. Generated pions energy from 5 GeV to 300 GeV. Tracker and magnetic field are off while the generation of particle processes.

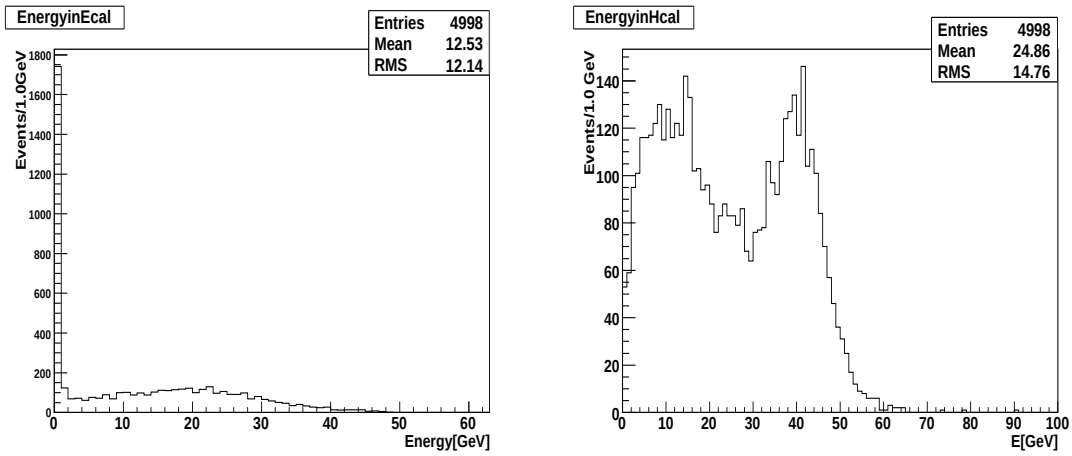
4.4. Energy Deposition in Calorimeters

The total energy in the barrel calorimeters (EB, HB, HO) of CMS detector is the sum from 7×7 crystals in EB and 3×3 hadronic towers in HB and HO for TB2006 studies. In the MC case size of EB and HB are the same for TB2006 but 3×2 hadronic towers used for HO. Figure 4.3 shows energy distributions in ECAL crystals and HCAL towers for incident beam energy was 50 GeV in the test beam. Energy deposition in ECAL crystals and HCAL towers are about 11 GeV and 28 GeV, respectively. Energy deposition in ECAL and HCAL for Monte Carlo studies was shown in Figure 4.4. In MC case, 12.5 GeV deposited in ECAL and 24.8 GeV deposited in HCAL calorimeters. Energy deposition in combined system is shown in Figure 4.5 for MC. Incident beam energy was 50 GeV and total energy in calorimeters was 37 GeV. All beam energy was not deposited in the CMS calorimeters.



(a) (b)

Figure 4.3. Energy deposition in ECAL (a) and HCAL (b) for 50 GeV pion beam for TB.



(a) (b)

Figure 4.4. Energy deposition in ECAL (a) and HCAL (b) for 50 GeV pion beam for MC.

4.5. Optimization of Energy Reconstruction and Response of Calorimeters

The intrinsic electron to hadron response (e/h) of a calorimeter is measure of its response to particles developing electromagnetic showers compared to particles developing non-electromagnetic ones and in compensating calorimeters e/h=1. Since CMS is non-compensating calorimeter, the e/h ratio for electromagnetic calorimeter and hadronic calorimeter is different from one and thus corrections have to be applied to obtain the true particle energy from the calorimeters.

Total energy was corrected and optimized using observed ECAL and HCAL energies and the known beam momentum using the test beam data which was taken in 2006. Correction and optimization procedure will be explained in three steps using the cluster energies. Thresholds, 0.8, 1.0 and 2.0 GeV for the EB, HB and HO clusters are applied on ECAL and HCAL energy clusters constructed from towers. If the cluster energy less than the threshold for that event the cluster energy set to zero.

The first correction is applied for the HB energy response using minimally ionizing events in the EB (E_{EB} <1 GeV). Pion to electron ratio (π/e) function is used to energy correction;

$$\pi/e = \frac{1+(e/h-1)f_0}{e/h} \tag{4.1}$$

where f_0 is the fraction of electromagnetic energy in a hadronic shower. 2 different f_0

functions were used for correction process, below 10 GeV $f_0 = 0.135log(E_{HB}) + 0.485$ and above 10 GeV $f_0 = 0.11log(E_{HB})$ and e/h is found to be 1.4. Thus HCAL cluster energy is corrected using equation 4.1. The next step is to correct the energy deposited in the EB using the event-by-event corrected energy values in HB. The corrected EB energy simply is the incident beam energy minus corrected energy in HB.

$$(\pi/e)_{EB} = \frac{E_{EB}}{P_0 - E^*_{HB}} \tag{4.2}$$

where E^*_{HB} is the corrected HB energy, $E_{HB}/(\pi/\mathrm{e})$. The cluster energy of ECAL is corrected using equation 4.3.

$$E^{Cor}_{EB} = \frac{E_{EB}}{(\pi/e)_{EB}} \tag{4.3}$$

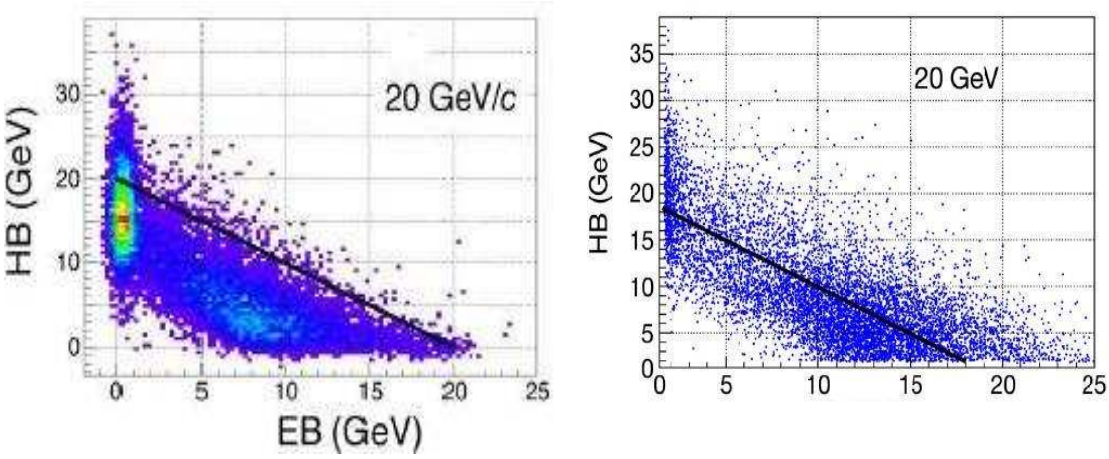
where $(\pi/e)_{EB} = 0.067\log(E_{EB}) + 0.46$.

After correcting the EB energies event-by-event, the π/e correction overestimates the total EB+HB energy values for events with large EB energy fractions, $Z \equiv E_{EB}/(E_{EB}+E_{HB}) > 70\%$. This is expected because these events correspond to the cases when a hadronic shower in the EB fluctuates largely to neutral particles. The final step in the correction parametrization is to linearize the total response of the EB+HB system by fitting the non-linear response to the correction function. This set of corrections has been determined to be insensitive to the pion beam momentum and 100 GeV/c data is a good representation for all other beam momentum data (HCAL/ECAL Collaboration, 2008).

$$< \frac{E^*_{EB} + E^*_{HB}}{Pb} >= 0.411Z^3 - 0.125Z^2 - 0.068Z + 1.00 \tag{4.4}$$

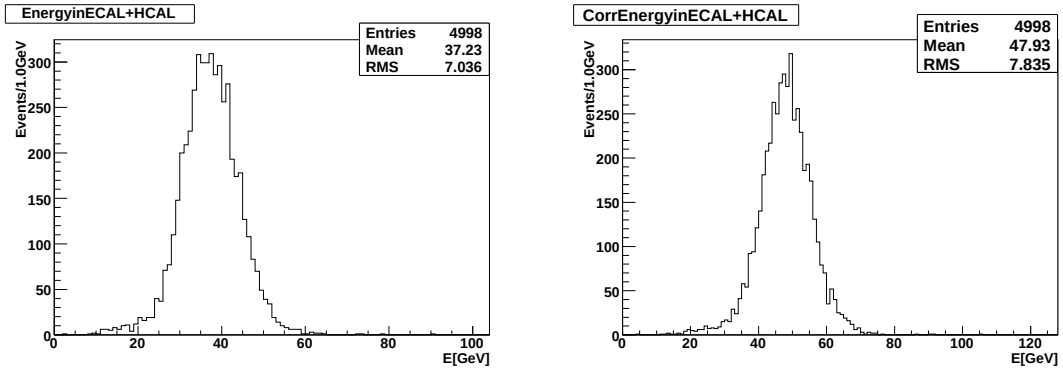
where Pb is the incident beam energy. The total energy is corrected using equation 4.4. Figure 4.5 shows energy scatter plot of the 20 GeV incident pion beam data before and after correction procedure. We used the same procedure to correct raw data from MC studies and raw and corrected energy distribution for the combined system (ECAL+HCAL) for 50 GeV pion beam was shown in Figure 4.6. For 50 GeV pion beam, total energy is increased 27% due to the energy correction function.

Energy response of calorimeter to pions with and without energy corrections were shown in the Figure 4.7. Energy resolution were shown in Figure 4.8 for TB2006 data and MC studies before and after corrections. In the simulation level, two different physics



(a) (b)

Figure 4.5. Scatter plot of the 20 GeV incident pion beam data for raw data (a) and corrected data (b) (HCAL/ECAL Collaboration, 2008).



(a) (b)

Figure 4.6. Total raw (a) and corrected (b) energy deposition in ECAL+HCAL system for 50 GeV pion beams for MC.

models were used. For low momentum, Low and High Energy Parameterization (LHEP) which is one of the simulation models was used for momentum range 5 GeV to 10 GeV, and after 10 GeV Quark Gluon String Precompound (QGSP) model was used. Pattern of energy response in Figure 4.7 has two different shapes because of the different physics models.

Energy response of calorimeters for the test beam data is higher than the energy response of calorimeters for Monte-Carlo data. This is because of the material between ECAL and HCAL in the test beam setup is different than the Monte-Carlo case or Geant is not simulating the detector very well.

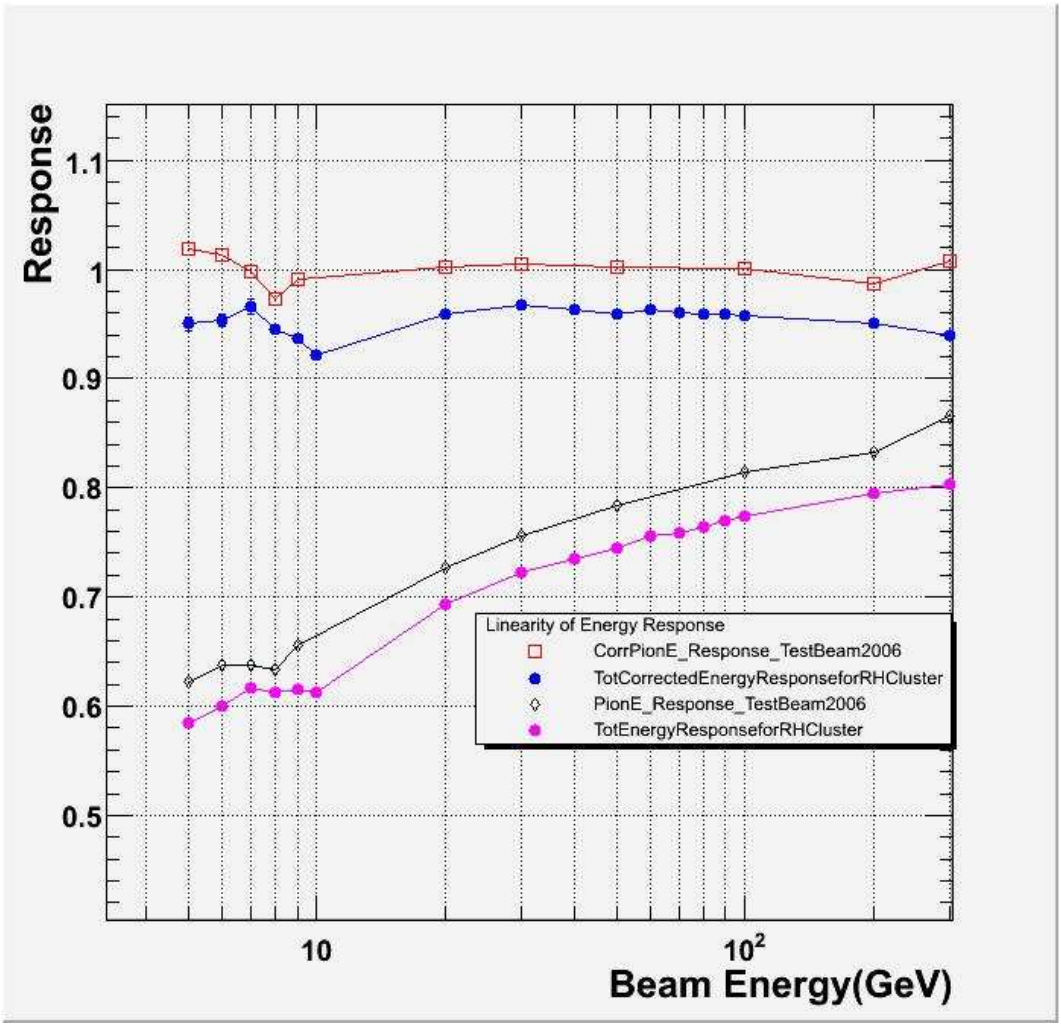
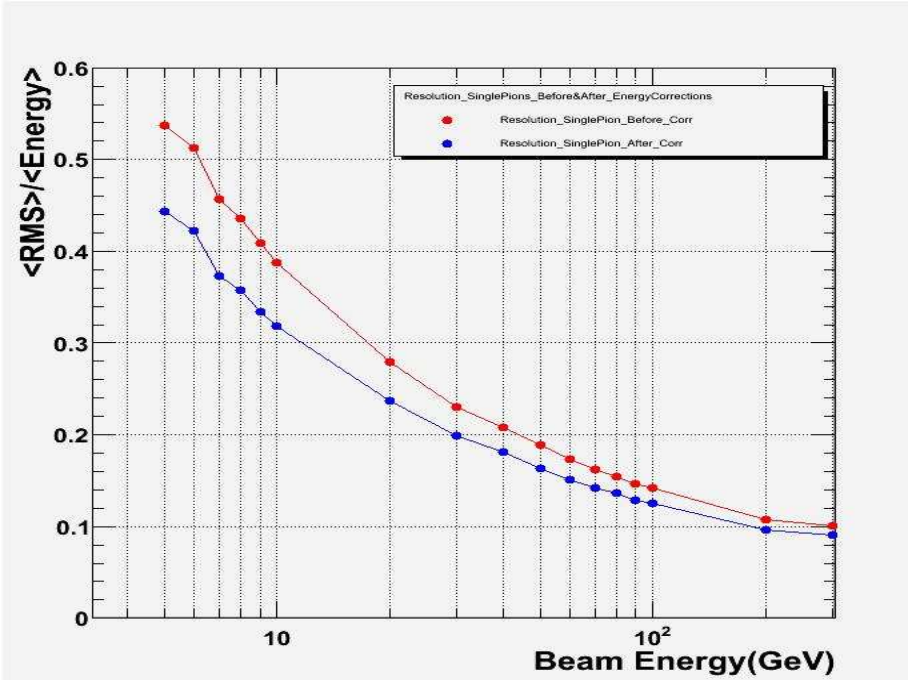
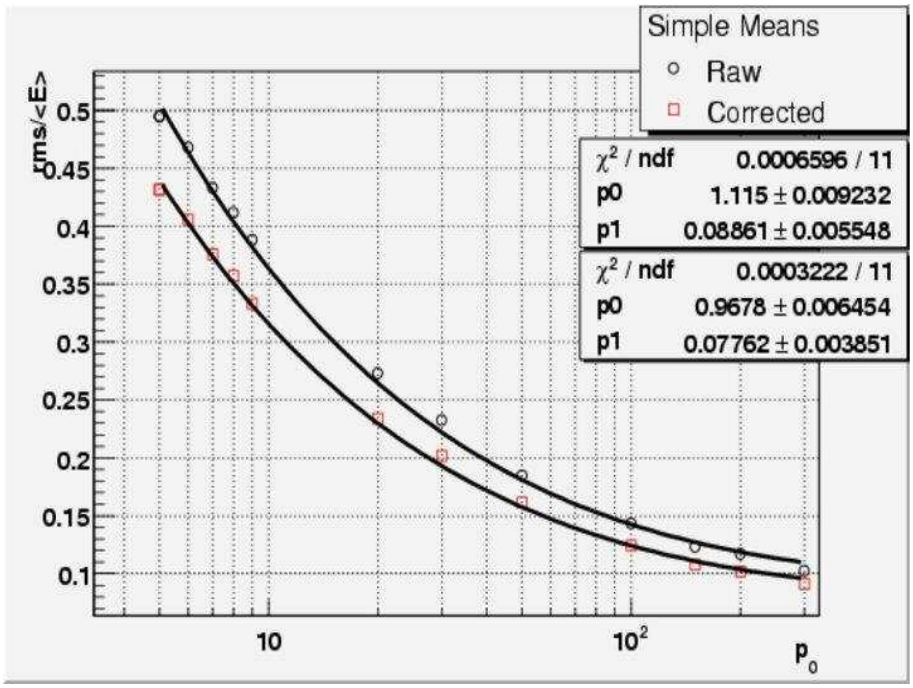


Figure 4.7. Energy response of calorimeter before and after the energy corrections for Test Beam and MC data.

In the test beam setup, magnetic field and tracker were off since in the Monte-Carlo magnetic field and tracker were also off till here. When the LHC starts both magnetic field and tracker have to be on, in order to see the effect of magnetic field and tracker on the response, this case was also studied. When magnetic field and tracker were on, energy response of the calorimeter to pions are shown in Figure 4.9. with the magnetic field and tracker on, the average response of HCAL decreases by 2% relative to without tracker and magnetic field.



(a)



(b)

Figure 4.8. Energy resolution of MC (a) and Test Beam (b) data before and after energy corrections.

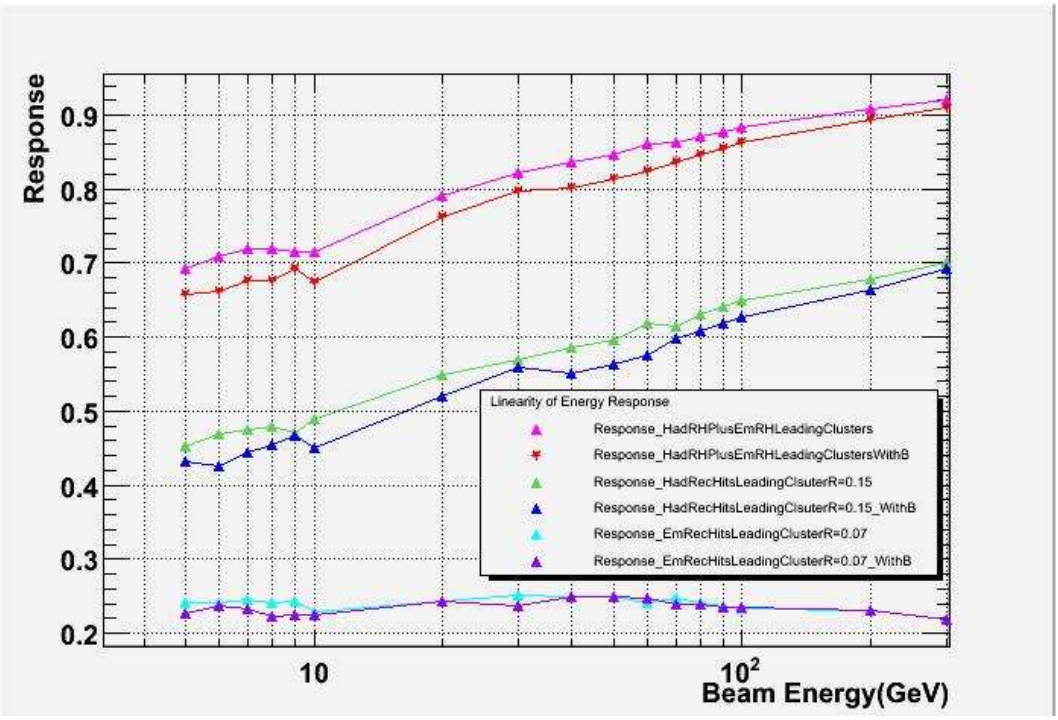


Figure 4.9. Energy Response of ECAL, HCAL and ECAL+HCAL to pions with and without B and Tracker.

5. ESTIMATION OF BACKGROUNDS

In the SUSY search main background comes from QCD, $Z \rightarrow (\nu\nu)$+jets, and $t\bar{t}$ productions. In this chapter the cuts used to reduce QCD and $t\bar{t}$ backgrounds to SUSY search for low mass 1 (LM1) test point at the CMS experiment will be explained.

5.1. Jets and Missing Transverse Energy

Jets are collimated spray of particles which are generated in the hadronization process of a gluon or quark into hadrons. The hadronization process produces a large number of colorless hadrons that appear in the detector as jets. They offer a connection between experimental results expressed in terms of hadron properties, and the theory, whose ingredients are quarks and gluons. A reconstruction processes is needed. By this process hadrons in the final states are grouped into jets and many jet algorithms have been proposed for this purpose such as midpoint cone, iterative cone, inclusive k_T (Angelini et al, 2004). Midpoint Cone (MCone) jet algorithm was used for the reconstruction process in the calorimeter level. We will use two types of jets: GenJets, or particle jets, are made from clusters of colorless stable Monte Carlo (MC) particles; CaloJets or jets which at the calorimeter level are made from clusters of energy deposits in projective calorimeter towers.

The **midpoint cone** algorithm which was designed to facilitate the splitting and merging of jets used in this analysis. The midpoint cone algorithm also uses an iterative procedure to find stable cones (proto-jets) starting from the cones around objects with an E_T above a seed threshold. The MCone algorithm was explained in the previous section.

The **Missing Transverse Energy** (MET) vector is calculated from the transverse vector sum over uncorrected, projective Calorimeter Towers:

$$\vec{E_T^{miss}} = -\sum_n (E_n \sin\theta_n \cos\phi_n \hat{\mathbf{i}} + E_n \sin\theta_n \sin\phi_n \hat{\mathbf{j}}) \tag{5.1}$$

where E_n is energy deposition in calorimeter towers, θ_n polar angle and ϕ_n azimuthal angle. The large missing transverse energy (MET) originates from the two LSPs in the final states of squark and gluino decays. The three or more hadronic jets result from the hadronic decays of the squark and/or gluinos. A typical cascade decay chain is shown in

Figure 5.1. In the final state the cascade decay chain, there is the lightest neutralino ($\tilde{\chi}_1^0$) which is the lightest SUSY particle (LSP), neutral and very weakly interacting. There is a huge imbalance in the transverse energy due to LSP will not leave any detectable signal in a detector. Figure 5.2 shows the MET distributions for SM backgrounds and SUSY signal sample which is LM1. The largest contribution come from the QCD events. Jet multiplicity and Pt distributions of jets without cuts for background events and signal events are shown at 1 fb^{-1} luminosity in Figure 5.3.

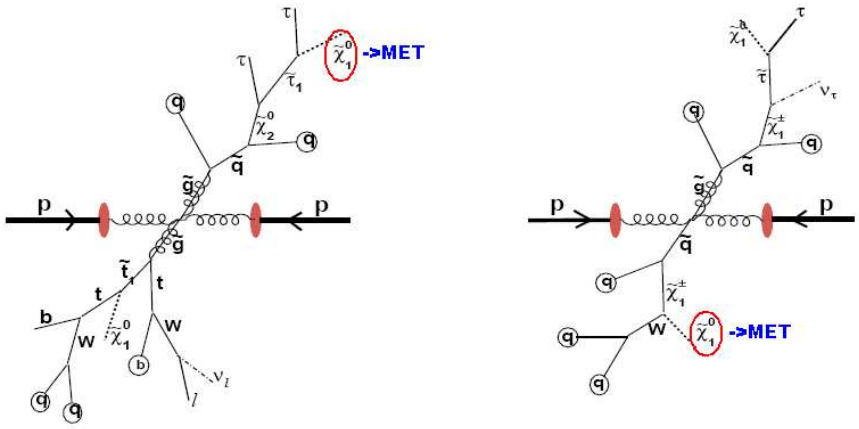
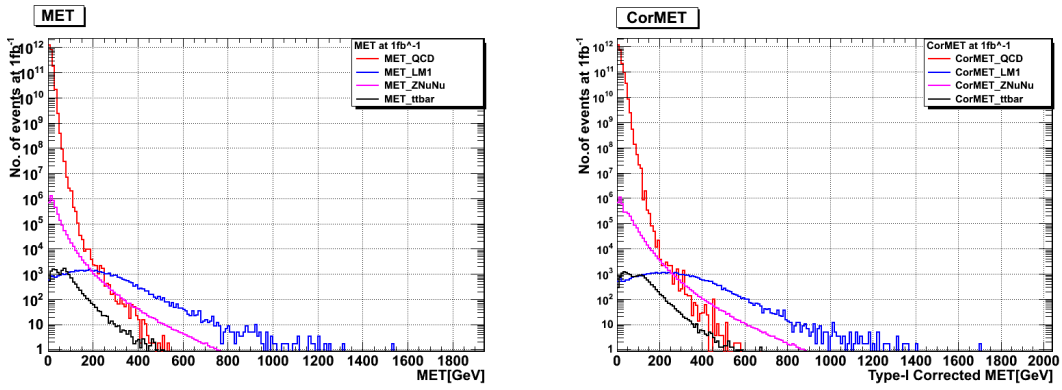


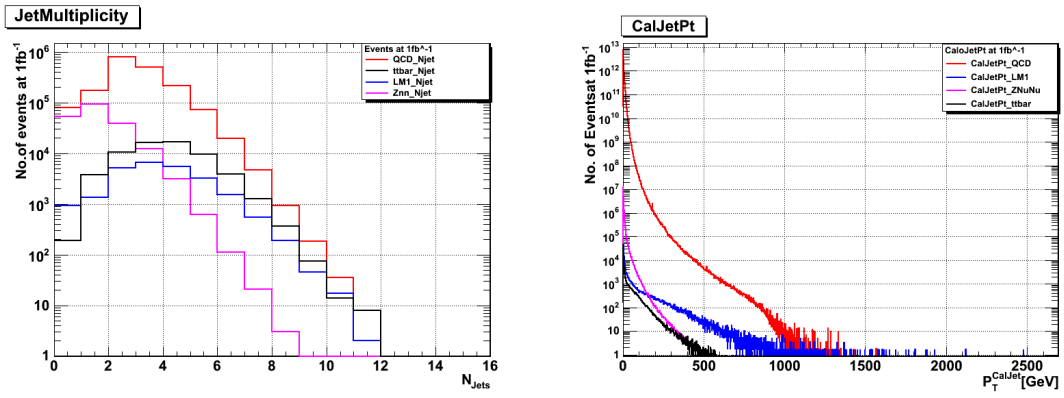
Figure 5.1. SUSY particle decays in p-p collisions (Sharma et al, 2009).



(a) (b)

Figure 5.2. Missing Transverse Energy (MET) in (a) and corrected MET in (b) distributions for QCD, $t\bar{t}$, Z+jets and LM1 events at 1 fb^{-1} luminosity.

The "raw" (uncorrected) E_T^{miss} may be corrected (due to jets, muons, etc.) and the resulting corrected E_T^{miss} object stored in the event. The calorimeter tower based E_T^{miss} is improved using the Type-I corrections. These corrections take the measured raw energy



(a) (b)

Figure 5.3. Jet multiplicity (a) and p_T distribution (b) for QCD, $t\bar{t}$, Z+jets and LM1 events at 1 fb^{-1} luminosity.

values and adjust them for the difference between the raw jet energy and the true jet energy, as defined by the Jet Energy Scale (JES) group. E_T^{miss} is corrected according to the following formula:

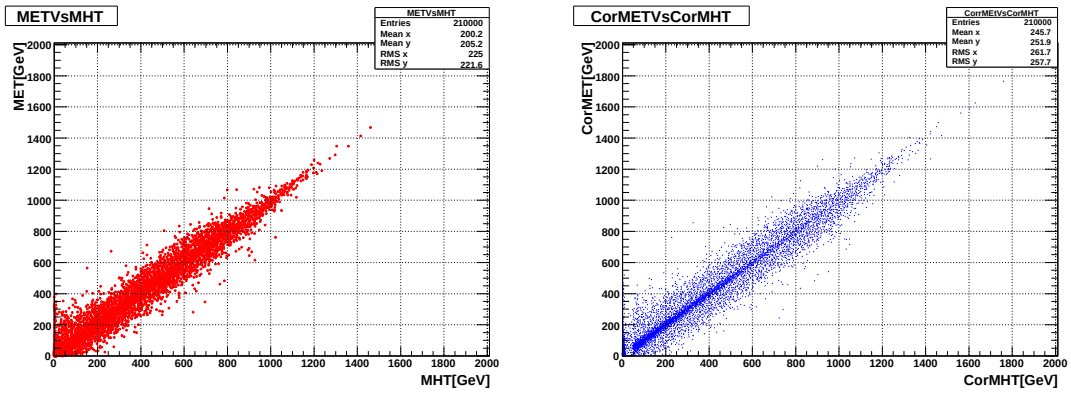
$$CorE_T^{miss} = E_T^{miss} - \sum_{i=1}^{N_{jets}} [p_{Ti}^{corr} - p_{Ti}^{raw}] \tag{5.2}$$

where the sum runs over all the jets with p_T^{raw} greater than jetPtThreshold and EMF less than jetEMFfraclimit. Default values of these two variables are 20 GeV and 0.9, respectively.

Calorimeter Jets are also corrected by the (JES) group. The purpose of the jet energy correction is to correlate the jet energy measured in the detector to the energy of the final state particle jet. Corrections to calorimeter reconstructed jets (CaloJets) as a function of jet E_T and eta (η) are available in CMS Soft Ware (CMSSW) framework. Monte Carlo Jet corrections take as an input a collection of Calojets and write as an output of corrected CaloJets. The MC jet correction was derived from the measurements of jet response is calculated by:

$$E_T^{CorrCaloJets}(\eta) = E_T^{GenJets}(\eta) \times \frac{E_T^{CaloJets}(\eta)}{E_T^{GenJets}(\eta)} \tag{5.3}$$

The Tevatron studies show that MET is very sensitive to detector effects such as dead/hot towers, therefore negative vector sum of momenta of jets (or missing transverse momentum) (MHT) can be used to reduce the detector effects. Correlation between MHT and



(a) (b)

Figure 5.4. MET versus MHT distribution (a) and corrected MET versus corrected MHT distribution (b) for $Z(->\!\!\!

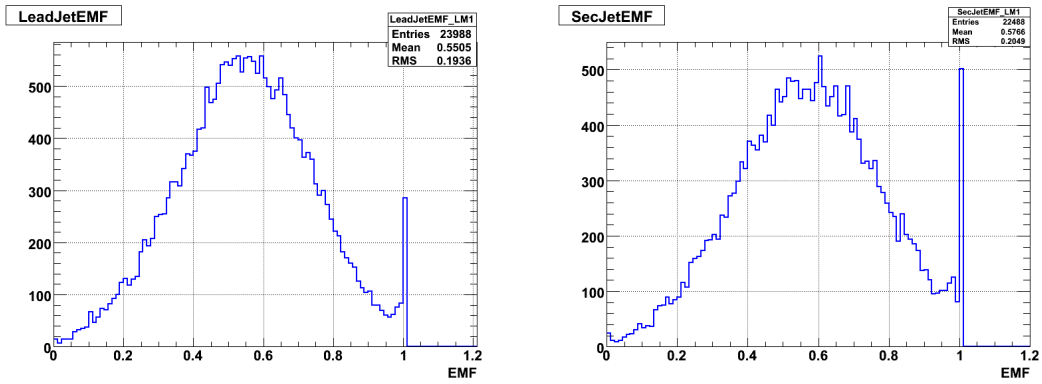
Table 5.1. Used QCD samples in SUSY search analysis in the jet+MET final state.

Sample	Used No.of Events	Cross Section (pb)
LM1	24999	42
$t\bar{t}$	62710	15
QCD(120$<\hat{p}_t<$170)	200000	$4.94E+05$
QCD(170$<\hat{p}_t<$230)	200000	$1.1E+05$
QCD(230$<\hat{p}_t<$300)	200000	$2.45E+04$
QCD(300$<\hat{p}_t<$380)	200000	$6.24E+03$
QCD(380$<\hat{p}_t<$470)	200000	$1.78E+03$
QCD(470$<\hat{p}_t<$600)	200000	$6.83E+02$
QCD(600$<\hat{p}_t<$800)	200000	$2.04E+02$
QCD(800$<\hat{p}_t<$1000)	200000	$3.51E+01$

These requirements are aimed to enrich the event sample with events having SUSY signature over QCD events and events coming from other SM processes. However, at LHC energies, a significant number of events produced from SM processes also satisfy these criteria.

5.3. Rejection of Beam Related and Cosmic Backgrounds

The energy deposited in the calorimeter from any source not originating from the interaction point contributes to the MET background. One of the important instrumental backgrounds to SUSY search process is due to the beam itself. The particles resulting from the interaction of beam particles with atoms of residual gas or due to beam losses around the beam core result in a large number of hadrons and muons which deposit energy in the calorimeter, mostly in the forward direction. On overlapping with the hard-scattering events in collision, these effects result in large MET. This type of background can be reduced on the basis of average Event Electromagnetic Fraction (EEMF) defined



(a) (b)

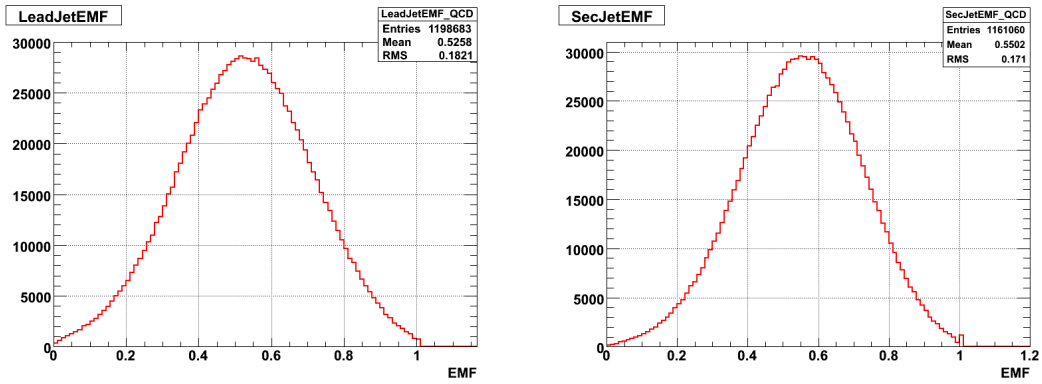
Figure 5.5. The EMF in mSUGRA LM1 sample for the leading jet (a) and for the second jet (b).

as:

$$EEMF = \frac{\sum_{j=1}^{N_{jet}} p_T^j \times EMF_j}{\sum_{j=1}^{N_{jet}} p_T^j} \tag{5.4}$$

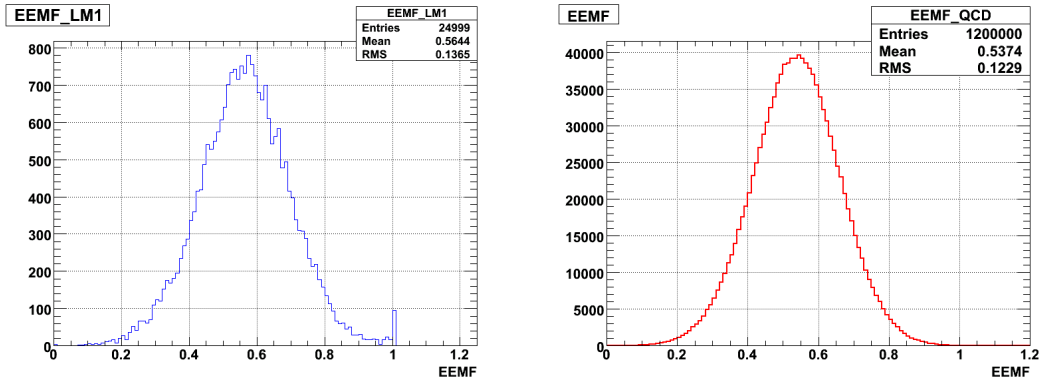
where EMF_j is the electromagnetic fraction and defined as $EMF = \frac{E^{Ecal}}{E^{Ecal+Hcal}}$ (energy measured by ECAL) of j^{th} jet and p_T^j is the sum of momenta of tracks in the vicinity of j^{th} jet. Average EMF between 0 and 1 for jets. Cosmic bremsstrahlung depositions of energy in either the Hadronic or Electromagnetic Calorimeter when clustered as jets will have EMF close to 0 or to 1. All hadronic depositions of energy resulting from beam halo events will have EMF close to 0. Electrons and photons that are also clustered as jets are expected to have EMF closer to 1. Due to these properties, the EMF of jet can be used as a "jet-quality" control variable. EMF distributions are shown in Figure 5.5 and 5.6 for first and second jets for QCD and LM1 samples. Figure 5.7 shows event electromagnetic fraction distributions for signal and QCD events.

The other contribution to fake MET is from Cosmic Ray events. However, these particles are not associated with primary interaction vertex. Therefore, they do not have the associated charged tracks originating from the primary vertex. The fact that a QCD jet contains nearly 65% of its energy from the charged particles created in the process of hadronization can be exploited to reduce the beam related and Cosmic ray back backgrounds. An average Event Charge Fraction (ECHF) is defined as the ratio of sum of p_T of all tracks associated with jets in an event to the ratio of the p_T of jet itself which is



(a) (b)

Figure 5.6. The EMF in QCD sample for the leading jet (a) and for the second jet (b).



(a) (b)

Figure 5.7. Event Electromagnetic Fraction in mSUGRA LM1 (a) and in QCD (b) samples.

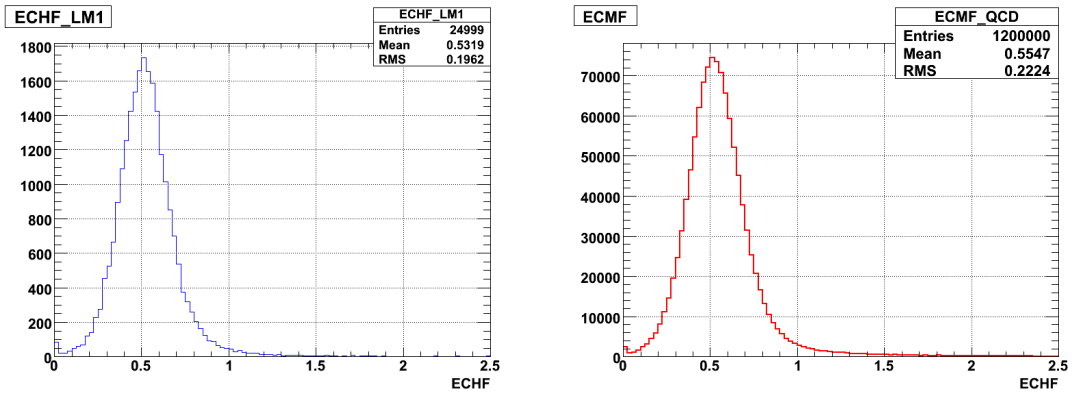
calculated from the calorimeter averaged over all the jets in an event.

$$ECHF = | < \frac{(\sum_i^{tracks} P_{Ti})_j}{P_{T\,j}} > |N_{jet} \tag{5.5}$$

where N_{jet} is the number of jets of cone 0.5 within η <1.7, $P_{T\,j}$ is the P_T of the jth jet and $(\sum_i^{tracks} P_{Ti})_j$ is the sum of the P_T of all the tracks matched with the jet. Figure 5.8 shows event charged energy fraction for the SUSY and QCD samples. After EEMF and ECHF cuts most of the beam halo and Cosmic Ray events are rejected.

5.4. Rejection of QCD Backgrounds

The main contribution to the high MET events in the QCD sample however comes from the effect of detector resolution and mis-measurement of jets. In a high P_T QCD di-jet event, the direction of missing E_T is aligned to one of the jets. Due to the large



(a) (b)

Figure 5.8. Event Charged Fraction in mSUGRA LM1 (a) and in QCD (b) samples.

production cross section of QCD events, a small fraction of events being mis-measured may contribute significantly to the tails of MET distribution.

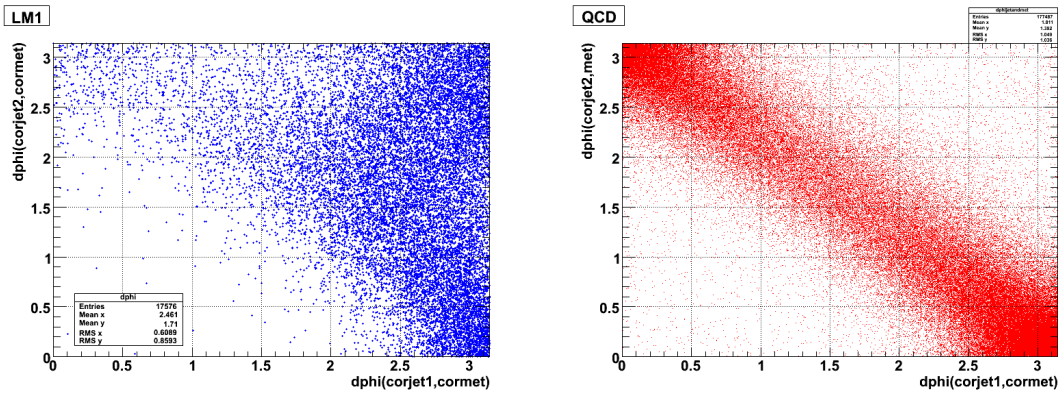
The angular distribution between the missing E_T direction and the first two leading jets in the transverse plane is shown in Figure 5.9 for the QCD and SUSY samples respectively. These two distributions clearly indicate the difference in shape of QCD and SUSY events. In these samples of high missing E_T events, there is a clear alignment of the missing E_T direction with the second leading jet in the QCD sample. A large fraction of these mis-measured events can be rejected by requiring the missing E_T direction not to be aligned to the second leading jet within 20°. There are however a small number of events where MET is aligned to the jet with the highest E_T. The correlation between the $\delta\phi(MET, 1^{st}Jet)$ and $\delta\phi(MET, 2^{nd}Jet)$ is shown in Figure 5.10. Clearly, the two quantities are highly correlated and can be combined to define the correlation variables R_{12} and R_{21}:

$$R_{12} = \sqrt{\delta\phi_1^2 + (\pi - \delta\phi_2)^2} \tag{5.6}$$

$$R_{21} = \sqrt{\delta\phi_2^2 + (\pi - \delta\phi_1)^2} \tag{5.7}$$

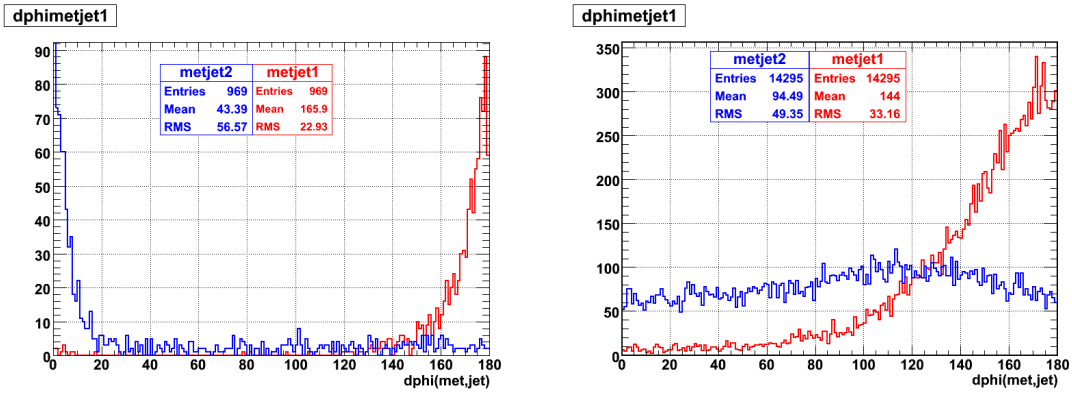
The residual QCD background can be further suppressed by rejecting events with R_{12}, $R_{21} < 0.5$. These cuts retain the signal events maximally.

There are many cuts used to reduce the SM backgrounds and survive the events in the signal sample in the SUSY search analysis. All used cuts in the jet+MET final state are given in the Table 5.2. In Table 5.2, H_T is defined as $H_T = MHT + E_t^{2.jet} + E_t^{3.jet} +$



(a) (b)

Figure 5.9. The correlation between first, second jet and E_T^{miss} in a (a) mSUGRA LM1 and (b) QCD sample.



(a) (b)

Figure 5.10. Distribution of $\delta\phi$ between MET and two leading jets , in the (a) QCD and in the (b) SUSY LM1 samples.

$E_t^{4.jet}$. After all cuts in Table 5.2 many background events of SM were rejected and some signal events were survived. Cumulative selection efficiency for LM1 and QCD events after each cut is given in Table 5.3. Figure 5.12 shows the Corrected MET and MHT distributions for SUSY signal sample and SM samples. Raw MET and MHT from raw jets distributions are shown in Figure 5.13. In both, corrected and raw MET distributions shown, used cuts can separate the signal shape from the SM backgrounds.

Table 5.2. The definition of event selection used in SUSY search analysis in the jets+MET.

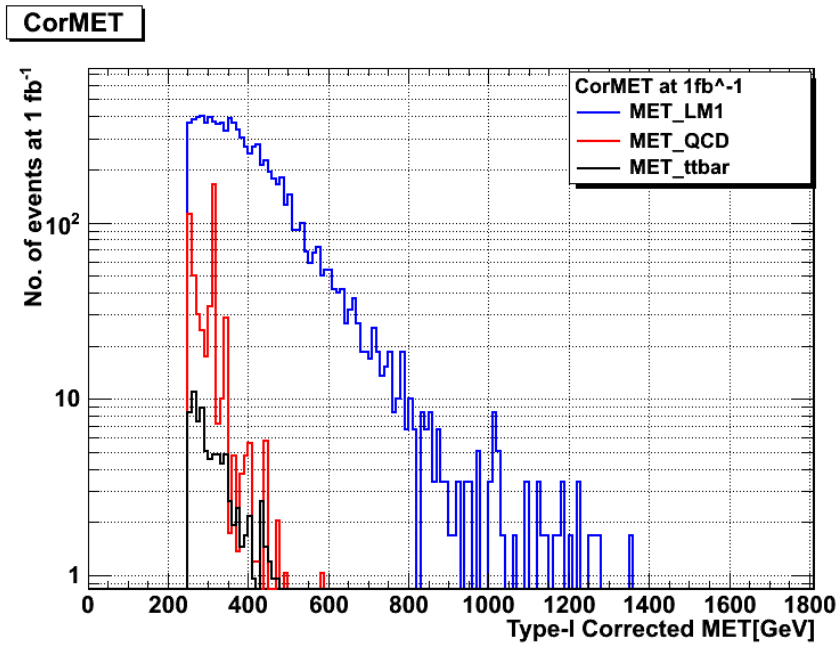
Label	Definition
HLT	CorMET>250 GeV
Event EMF fraction (EEMF)	≥ 0.175
Event charged fraction (ECHF)	≥ 0.1
Jets	$P_T^{CorJets} > 50$ GeV, $\|\eta^{jets}\| < 3.0$, $\|\eta^{1stJet}\| < 1.7$
$EMF_{Jet}^{1st} \& EMF_{Jet}^{2nd}$	<0.9
Jet multiplicity	≥ 3
Angular Cut(1)	$\delta\phi(met, jet2) > 20^\circ$
Angular Cut(2)	$R1 > 0.5 \& R2 > 0.5$
E_T^{1stJet}	> 180 GeV
E_T^{2ndJet}	> 110 GeV
HT	> 500 GeV

5.5. Result

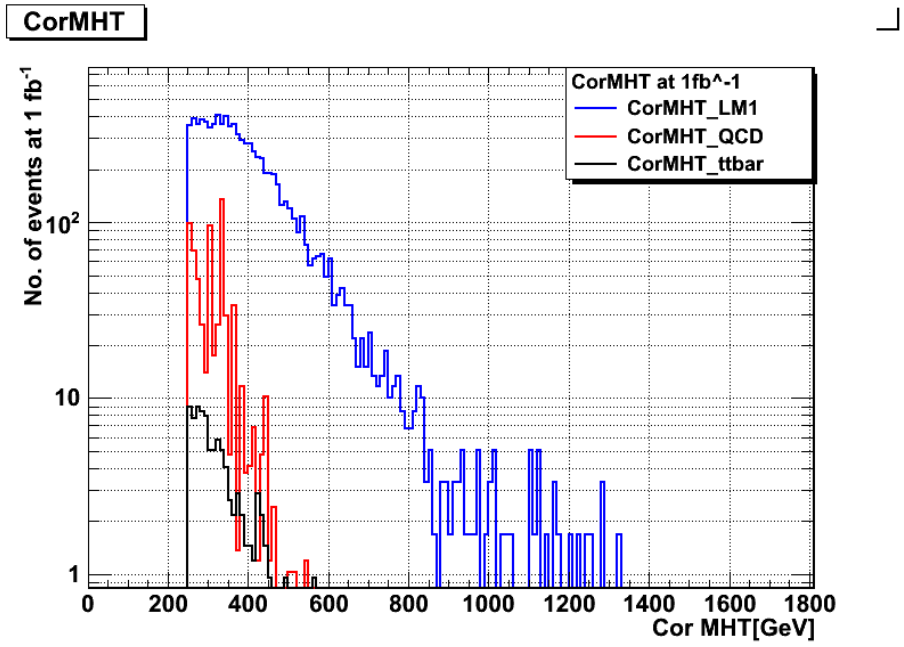
QCD and $t\bar{t}$ samples used as SM backgrounds and LM1 sample was a signal sample for SUSY search at CMS experiment. Different cuts were used to eliminate the events from various sources. Used cuts removed most of the background events and survived the signal events. Number of events that pass the cuts which were given in Table 5.2 are given in Table 5.4. The MET events with uncertainties are 4791±90 for LM1, 442±57 for QCD and 44±3 for $t\bar{t}$ samples. Signal significance (S) can be calculated from equation 5.8.

$$S = \frac{N_S}{\sqrt{N_B}} \tag{5.8}$$

where N_S is the measured signal number and N_B is measured background number. Signal significance for MET events is 217.

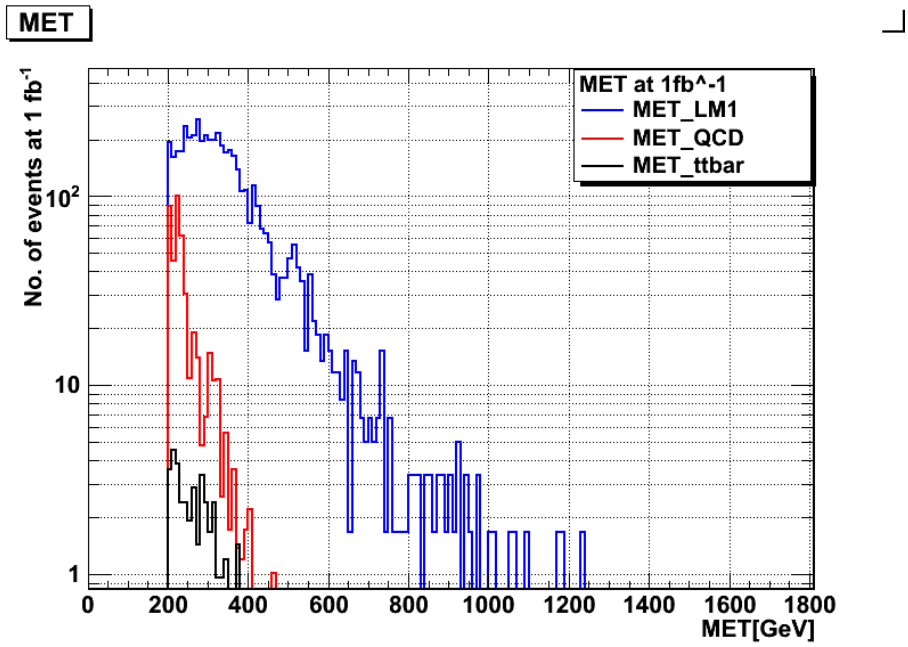


(a)

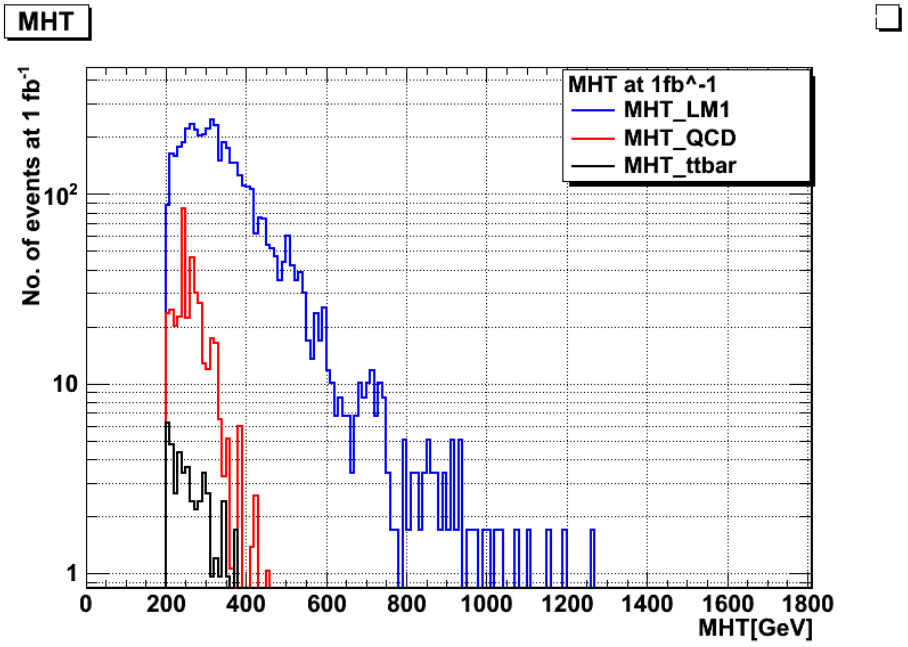


(b)

Figure 5.11. Corrected MET and MHT distributions in (a) and (b) for signal, QCD and $t\bar{t}$ samples.



(a)



(b)

Figure 5.12. MET in (a) and MHT in (b) distributions in signal (LM1), QCD and $t\bar{t}$ samples.

Table 5.3. Cumulative selection efficiency for LM1 and QCD samples at each selection step.

Selection Cut	LM1 (Signal) Sample	QCD Sample
All	100	100
HLT(MET>200 GeV)	47.2	0.6
$N_{jet} \geq 3$	32.9	0.4
$\lvert\eta^{1^{st}Jet}\rvert \leq 1.7$	28.5	0.3
EEMF≥0.175	28.5	0.3
ECHF≥0.1	28.4	0.3
QCD Angular	24.3	0.1
EMF(jet1), EMF(jet2)<0.9	23.5	0.1
$E_T^{1^{st}Jet} > 180$ GeV & $E_T^{2^{nd}Jet} > 110$ GeV	14.1	0.077
$H_T > 500$ GeV	12.1	0.073

Table 5.4. Number of events passed all cuts at 1 fb^{-1}.

Sample	Corrected MET (Raw MET)	Corrected MHT (Raw MHT)
LM1	8902 (4791)	8683 (4757)
QCD	515 (442)	648 (386)
$t\bar{t}$	91 (44)	95 (52)

6. DETERMINATION OF INVISIBLE Z BOSON+JETS BACKGROUND TO HADRONIC SUSY SEARCH

In this section how to estimate the invisible Z boson+jets background to hadronic SUSY search will be explained.

6.1. Estimation of Z+Jets Background

The Z boson+jets events where Z boson decays into neutrinos represent an irreducible background to SUSY search. The size of this background must be estimated and then subtracted from the final distributions. We propose a method to estimate this background by first measuring the amount of events with a Z boson decaying into muons and with multi-jets as required in the search for SUSY signal with jet+MET topology. This number of events is then scaled by the theoretical ratio of $\Gamma(Z->\nu\nu)$ and $\Gamma(Z->\mu\mu)$ to find the estimated size of the $\Gamma(Z->\nu\nu)$+jets background to SUSY signal.

6.2. Overview of the Procedure

We use the advantage of the fact that in the Standard Model the $Z->\nu\nu$+jets events have the same kinematic characteristic as the $Z->\mu\mu$+jets events and they only have different production rates. According to theoretical calculations, a Z boson decays into any pair of neutrinos 5.95 times more often than into a pair of muons. Therefore one can estimate N_μ, the number of events where Z boson decaying to muon pairs, and then multiply this number by the ratio of $\Gamma(Z->\nu\nu)$ and $\Gamma(Z->\mu\mu)$ to obtain an estimate of N_ν, the number of events where a Z boson decaying to neutrinos:

$$N_\nu = N_\mu \times \frac{\Gamma(Z->\nu\nu)}{\Gamma(Z->\mu\mu)} \tag{6.1}$$

We plan to determine N_μ from a data sample of events containing pairs of muons as selected by a muon trigger, and then retain only a subset of these events where the invariant mass of the pair of muons is consistent with the mass of the Z boson. Taking into account the trigger efficiency, ε_{trig}, and the Z boson identification efficiency, A_Z, we can express

N_μ in Equation 6.1 as follows

$$N_\mu = \frac{N_\mu^{'}}{\varepsilon_{trig} A_Z} \tag{6.2}$$

where $N_\mu^{'}$ is the number of events selected by the muon trigger, and that have a Z boson decaying to muons. Up to now, Equation 6.1 and 6.2 are written for number of events passing no particular requirements other than the trigger and Z boson selections. The equations can be generalized for events that pass additional requirements such as the full event selection used in the search for SUSY making the following transitions;

$$N_\nu \rightarrow N_\nu^{ES}, \quad N_\mu \rightarrow N_\mu^{ES}, \quad N_\mu^{'} \rightarrow N_\mu^{ES^{'}} \tag{6.3}$$

where N_μ^{ES} is the number of $Z \rightarrow \mu\mu$+jets events passing the full event selection used in the search for SUSY, N_ν^{ES} is the corresponding number of $Z \rightarrow \nu\nu$+jets events, and $N_\mu^{ES^{'}}$ is the subset of $Z \rightarrow \mu\mu$+jets events passing the muon trigger and Z boson selections. However, for early data when the amount of integrated luminosity is low, not many $Z \rightarrow \mu\mu$ events will pass the full event selection which retains N_μ^{SR} events in the muon data sample such that

$$N_\mu^{ES^{'}} = N_\mu^{SR} \times A_{SF} \tag{6.4}$$

where A_{SF} is a scale factor to be determined from Monte Carlo using events with at least three jets.

The number of events passing the light event selection, N_μ^{SR}, is estimated from the distribution of E_T^{miss} as follows. First, we fit the distribution in a control region (CR), and then we use the fit function, $f^{CR}(MET)$, extended in the signal region (SR) to represent the real E_T^{miss} distribution. The integral of $f^{CR}(MET)$ in region SR is an estimate of N_μ^{SR}, the number of events passing the light event selection. The procedure for estimating N_ν^{ES}, the size of the $Z \rightarrow \nu\nu$+jets background to the SUSY search is summarized in Equation 6.5.

$$N_\nu^{ES} = \frac{\Gamma(Z->\nu\nu)}{\Gamma(Z->\mu\mu)} \times \frac{A_{SF}}{\varepsilon_{trig} A_Z} \times \int_{SR} f^{CR}(MET) dMET \tag{6.5}$$

We choose the E_T^{miss} distribution to calculate the number of events as this distribution represents one of the figures of merit in which new physics in the form of SUSY can manifest itself and from which the amount of Standard Model processes such as $Z \rightarrow \nu\nu$+jets needs to be subtracted.

6.3. Samples and Event Selection

In this analysis we used $Z->\mu\mu$+jets events generated with ALPGEN and PYTHIA for various ranges of the tranverse momentum of the Z boson. Table 6.1 and 6.2 show the cross section and number of events per $Z->\mu\mu$+jets and Z+jets PYTHIA and ALPGEN samples used in this analysis. Selection of muons is very important in this analysis because Z boson is reconstructed from the muon pairs. Hence, we have to make sure that used muons decayed from the Z boson.

6.3.1. Muon Sources and Selection

Many interesting processes have one or more high-p_T muons in the final state at the LHC. This feature can be exploited in the online trigger and for the off-line selection by setting a threshold on the p_T of reconstructed muons. In the low-p_T region it is dominated by muons from K and π decays, while muons from b and c decays are dominant in the intermediate-p_T range. The contribution from W and Z decays becomes the most important above $p_T \sim 30$ GeV/c. 15-25 GeV/c p_T ranges the b, c component of muon rates is the largest source of background in the trigger. The rejection of these muons is difficult since they are real and prompt, *i,e.* produced close to the interaction point. A way to separate muons from b, c decays from those signal events relies on the fact that b and c quarks are produced in jets while muons from heavy object decays (like $W \rightarrow \mu\nu$) are *isolated-i.e.* not surrounded by other particles, except for those from pile-up collisions. Since non-isolated muons are accompanied by jets, while isolated ones have only uncorrelated soft particles from pile-up in their proximity, a muon can be defined as isolated by comparing the measurement of some quantity (*e.g.* the transverse energy deposited in the calorimeters or the sum of transverse momenta of tracks) in a cone around the muon with a predefined threshold. The cone axis is chosen according to the muon direction with a procedure that is tailored to the specific properties of each algorithm. The geometrical definition of the cone is given by the condition $\Delta R = \sqrt{\Delta\eta^2 + \Delta\phi^2}$, $\Delta\eta$, $\Delta\phi$ being the distances in pseudorapidity and azimuthal angle between the deposit and the cone axis. The muon itself contributes to the detector measurement inside the cone. This contribution

can be subtracted to improve the discriminating power of the isolation algorithm. Several quantities in the cone can be obtained from detector measurements. Calorimeter isolation, the transverse energy measured in the towers of the hadronic calorimeter (HCAL) are combined with the reconstructed transverse energy deposit in the electromagnetic calorimeter (ECAL) (Amapane,et al., 2002).

Table 6.1. Summary of the PYTHIA samples used in the analysis.

$Z \rightarrow \mu\mu$+jets		
$P_T^Z[GeV/c]$	Cross-section(pb)	Number of events
15-20	3.504E+2	15000
20-30	3.267E+2	15000
30-50	2.270E+2	15000
50-80	9.317E+1	15000
80-120	3.148E+1	15000
120-170	9.630	15000
170-230	2.920	15000
230-300	8.852E-1	15000
300-380	2.936E-1	15000
380-470	1.025E-1	15000
470-600	4.242E-2	15000
600-800	1.443E-2	15000
800-1000	2.859E-3	15000
1000-1400	9.400E-4	15000
1400-1800	9.536E-5	15000
1800-2200	1.232E-5	15000
2200-2600	1.839E-6	15000
2600-3000	2.881E-7	15000
3000-3500	4.764E-8	15000

The extraction of the energy deposits is done independently in the ECAL and the HCAL. In the case of ECAL the measured quantity is $\sum E_T$ in the crystals around the muon direction at the vertex. In the case of HCAL, whose segmentation is much coarser than that of ECAL, the cone axis is defined instead as the center of the tower to which the muon direction at the vertex points; the measured quantity is the $\sum E_T$ of the towers whose center belongs to the cone. This guarantees that the same number of towers contributes

Table 6.2. Summary of the ALPGEN samples used in the analysis.

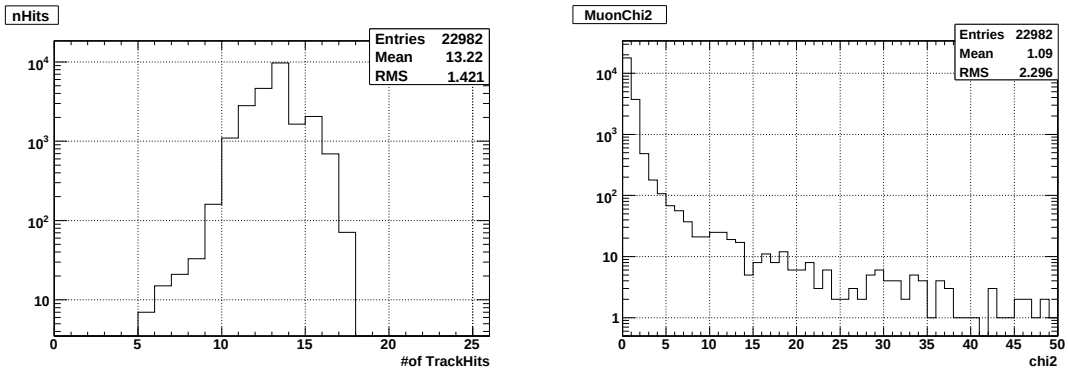
Sample	$P_T^Z(GeV/c)$	Cross-section(pb)	Number of events
$Z+0$-jets	n/a	4400	200,000
$Z+1$-jets	0-100	940	56000
$Z+1$-jets	100-300	30	25592
$Z+1$-jets	300-800	0.36	24000
$Z+1$-jets	800-1600	0.0021	12000
$Z+1$-jets	1600-3200	0.000017	18470
$Z+2$-jets	0-100	270	54000
$Z+2$-jets	100-300	28	26783
$Z+2$-jets	300-800	0.55	29431
$Z+2$-jets	800-1600	0.004	8000
$Z+2$-jets	1600-3200	0.00004	16752
$Z+3$-jets	0-100	68	26432
$Z+3$-jets	100-300	13	12000
$Z+3$-jets	300-800	0.4	20000
$Z+3$-jets	800-1600	0.0038	12419
$Z+3$-jets	1600-3200	0.000041	13368
$Z+4$-jets	0-100	14	14000
$Z+4$-jets	100-300	4.3	6000
$Z+4$-jets	300-800	0.2	24598
$Z+4$-jets	800-1600	0.0025	10000
$Z+4$-jets	1600-3200	0.000028	20955
$Z+5$-jets	0-100	8.8	9000
$Z+5$-jets	100-300	5	5000
$Z+5$-jets	300-800	0.45	20000
$Z+5$-jets	800-1600	0.0074	29379
$Z+5$-jets	1600-3200	0.000091	13762

to all cones of a given size at a given pseudorapidity. The actual isolation variable is constructed from both HCAL and ECAL deposits in the cones;

$$E_T^{Iso} = \sum E_T^{ECAL} + \sum E_T^{HCAL} \tag{6.6}$$

Equation 6.6 can be used to isolation of muons. Additionally, in order to select good muons some extra cuts can be applied and these cuts are kinematical and quality cuts. Kinematical cuts for muons are;

- at least two muons $P_T^{\mu} \geq 7$ GeV, and $|\eta_{\mu}| \leq 2.4$,



(a) (b)

Figure 6.1. Muon quality variables number of track hits (a) and global fit function (b)$\chi^2/ndof$.

- $|Zmass - 91.2|$ <20 GeV

and quality cuts are,

- $\chi^2/ndof$ <10,
- number of Hits (nHits)$\geq$ 10,
- $d0 < 0.25$

$\chi^2/ndof$ is a function matching between track muons and global muons and isolation cut is

- $\sum EtHcal + \sum EtEcal < 5$ GeV

Figure 6.1 shows the number of track hits and $\chi^2/ndof$ distributions for muons. Muons which are passing the quality cuts are used to reconstruct the Z boson mass. Two leading highest P_T muons are used in the events.

6.3.2. Event Selection

The event selection optimized for the SUSY mass point LM1 is detailed in Table 6.3. We define HT as the sum of the transverse energies of all jets in the event. Moreover, we use only the cuts listed in Table 6.4, together with the requirements for selecting muons and identifying Z-bosons. The indirect lepton veto cuts were not used because they do not have any effect on the $Z \rightarrow \nu\nu$. The angular cut(1) is removed because it is

not optimum for the SUSY search. In the case of angular cut(2), dropping it or not makes no difference in the event count as long as the angular cut(3) is maintained, and it was not used. We also drop the hard cuts on the E_T of the leading two jets and cut on HT because of the limited statistics of simulated $Z \rightarrow \mu\mu$+jets samples. The effect of the last three cuts on the final estimate of the $Z \rightarrow \nu\nu$+jets background samples is reproduced by the multiplication with a scale factor. This scale factor is computed from the $Z \rightarrow \mu\mu$+jets ALPGEN sample as the efficiency of these three last cuts with respect to the total number of events passing the other cuts. Due to the lack of trigger information in the samples used in this analysis, the events are not subject to any muon trigger requirement. However, we intend to use data selected with the relaxed muon trigger bit (Level1: $P_T^{\mu} \geq 7$ GeV/c, HLT: $P_T^{\mu} \geq 16$ GeV/c) which has an efficiency ε_{trig} =98.6% for the $Z \rightarrow \mu\mu$ sample.

Using the muons selected as explained in the previous section, we form pairs of negatively and positively charged muons and calculate their invariant mass. The Z-boson is identified as the pair of muons that has an invariant mass within 20 GeV/c^2 of the Z-boson mass pole of 91.2 GeV/c^2. If there are more pairs satisfying this criteria, the one that is the closest to the mass pole was used. Invariant mass and P_T of the di-muon is consistent with the mass and P_T of the Z boson. E_T^{miss} is calculated from generated and calorimeter level. These distributions are shown from the Z mass window for $Z(->\mu\mu)$+jets samples in the Figure 6.2. As we can see the patterns of distributions are not affected because of the Z mass window. Figure 6.3 shows the E_T^{miss} distributions for events with ≥ 3 jets and the *R*-cuts for the PYTHIA and ALPGEN samples.

Two regions were defined: the signal region (SR) as being composed of events passing the loose event selection listed in Table 6.4, and the control region (CR) which includes events with $100 \leq E_T^{miss} \leq 200$ GeV. Table 6.5 shows the number of events in PYTHIA and ALPGEN samples with different jet multiplities in two E_T^{miss} region.

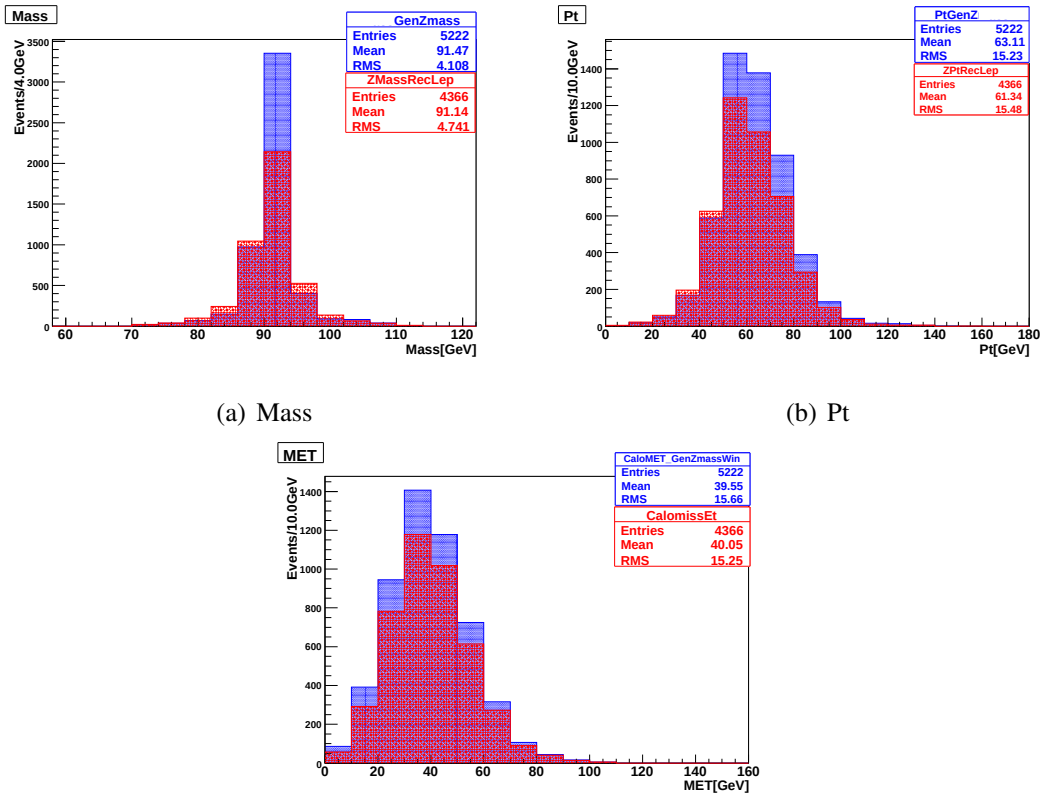
Table 6.4 shows also the cumulative efficiency for each step in the loose event selection as calculated in the $Z \rightarrow \mu\mu$+jets ALPGEN sample. In this sample the fraction of events passing the muon selection and Z-boson identification selection is A_Z=34.9$\pm$0.3%, and this number is used in Equation 6.5. From the events passing the loose event selection only A_{SF}=32.5$\pm$3.4% pass the last three requirements of the full event selection (Table 6.3).

6.4. Results of the Estimating Procedure

Using the $Z \rightarrow \mu\mu$+jets ALPGEN events passing the loose event selection (Table 6.4), we construct the E_T^{miss} distribution using only the calorimeter data. This distribution (circles) is shown in log scale in Figure 6.4, corresponding to an integrated luminosity of 1fb^{-1}. We use this distribution to estimate, N_μ^{SR}, the number of $Z \rightarrow \mu\mu$+jets events that will be rescaled to determine, N_ν^{ES}, the number of $Z \rightarrow \nu\nu$+jets background events to SUSY. We choose an exponential as the function $f^{CR}(MET)$ to fit the E_T^{miss} distribution in the control region CR. In addition to the distribution of E_T^{miss}, Figure 6.4 also shows the fitted function $f^{CR}(MET)$ (line) and the extrapolation of this function into the region SR (squares). Integrating the extension of the function $f^{CR}(MET)$ in the signal region SR, we obtain that the estimated number of $Z \rightarrow \mu\mu$+jets events in this region is N_μ^{SR}=150 for an integrated luminosity of 1 fb^{-1}, while we expect N_μ^{true}=194 events.

Table 6.3. The definition of the event selection used in the SUSY search analysis in the jets+E_T^{miss} final state.

Label	Definition
Level 1	Trigger efficiency parameterization
HLT	$E_T^{miss} \geq 200$ GeV
Primary Vertex	≥ 1
Event EM fraction	EEMF≥ 0.175
Event Charged Fraction	ECHF≥ 0.1
Jets	$E_T \geq 30$ GeV, $\|\eta\| \leq 3$, $\|\eta_1\| \leq 1.7$
Jet Multiplicity	≥ 3
Angular cut(1)	$\delta\phi_{min}(E_T^{miss}, jets) \geq 0.3$
Angular cut(2)	$\delta\phi(E_T^{miss}, 2^{nd}\, jet) \geq 20^\circ$
Angular cut(3)	$R_1 \geq 0.5$, $R_2 \geq 0.5$
Indirect lepton veto (1)	Iso_{trk}=0
Indirect lepton veto (2)	$Fraction_{EM}^{jet1,2} \leq 0.9$
$E_T^{1^{st}Jet}$	$\geq$180 GeV
$E_T^{2^{nd}Jet}$	$\geq$110 GeV
HT	$\geq$500 GeV



(a) Mass

(b) Pt

(c) E_T^{miss}

Figure 6.2. Mass, P_T and E_T^{miss} in $Z->\mu\mu$+jets samples (a) mass, (b)P_T, (c)E_T^{miss} from di-muon mass window.

6.5. Statistical Uncertainty

The statistical uncertainty on the estimate is determined using pseudo-experiments. The pseudo-experiments are formed by creating new E_T^{miss} distributions for region CR through random sampling of the function $f^{CR}(MET)$. The number of events in each pseudo-experiment is randomly set based on a Poisson probability with the mean equal to 677, the expected number of events in region CR. The E_T^{miss} distribution of each pseudo-experiment thus created to is fit to an exponential and then the newly obtained fit function is integrated in region SR to obtain new estimates. The distribution of the results from each pseudo-experiment is used to extract, $\delta N_\mu^{SR}(+)$ and $\delta N_\mu^{SR}(-)$, the asymmetrical statistical uncertainty on N_μ^{SR}.

Figure 6.5 shows the results of 10,000 pseudo-experiments corresponding to an integrated luminosity of 1 fb^{-1}. In this distribution, the smallest interval on the horizontal

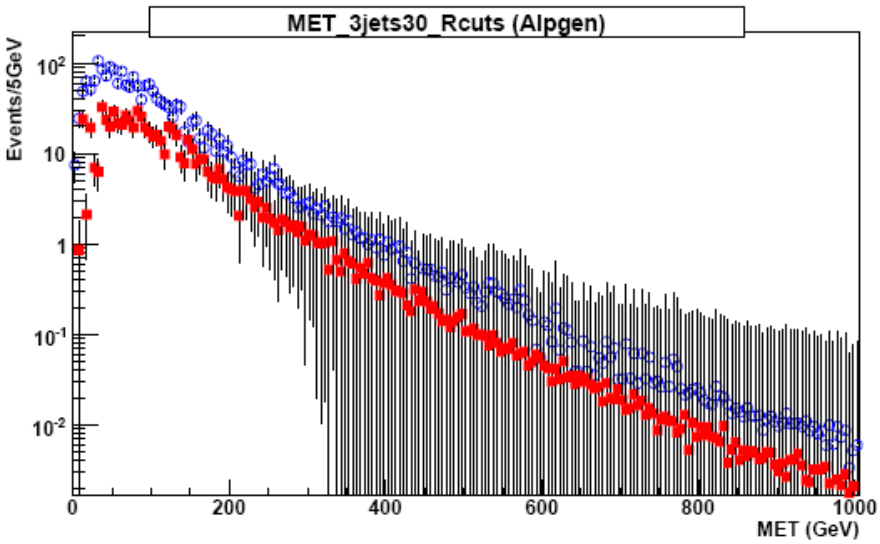


Figure 6.3. E_T^{miss} distribution for events with ≥3 jets and passing the R-cuts for the PYTHIA $Z \rightarrow \mu\mu$+jets sample (red) and for the ALPGEN sample (blue).

Table 6.4. The definition of the loose event selection used in the present analysis. For the combined $Z \rightarrow \mu\mu$+jets ALPGEN sample, the third column shows the cumulative efficiency at each selection step, while the fourth column shows the expected number of events for an integrated luminosity L=1 fb^{-1}

Label	Defin.	Eff. (%)	Evt. No. (1 fb^{-1})
Muon selection	$P_T \geq 7\ GeV/c$, $\lvert\eta\rvert \leq 2.4$	40.5	779739
Z-boson ID	$\lvert M_{\mu^+\mu^-} - 20\rvert \leq 91.2 GeV/c^2$	34.9	671751
HLT	$E_T^{miss} \geq 200$ GeV	0.0425	818
Primary Vertex	≥ 1	0.0425	818
Event EM fraction	EEMF≥ 0.175	0.0424	816
Event Charged Fraction	ECHF≥ 0.1	0.0356	686
Jets	$E_T \geq 30$ GeV, $\lvert\eta\rvert \leq 3$, $\lvert\eta_1\rvert \leq 1.7$	–	–
Jet Multiplicity	≥ 3	0.0122	235
Angular cut(3)	$R_1 \geq 0.5$, $R_2 \geq 0.5$	0.0101	194

axis that includes 68% of the total number of entries is chosen to represent the sum of $\delta N_\mu^{SR}(+)$ and $\delta N_\mu^{SR}(-)$. Since by construction this interval contains the maximum of the distribution, we define $\delta N_\mu^{SR}(+)(\delta N_\mu^{SR}(-))$ as the difference between the higher (lower) edge of the interval and the maximum of the distribution. We propose to use this Monte Carlo study to determine the correction factor (K) needed to remove the bias in the esti-

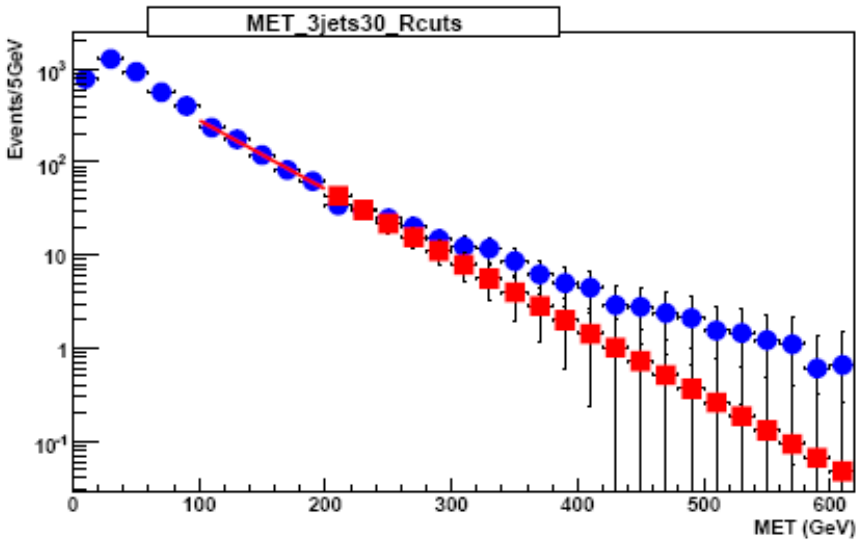


Figure 6.4. E_T^{miss} distribution (circles) from $Z \rightarrow \mu\mu$+jets ALPGEN events passing the loose event selection at 1 fb^{-1} luminosity. Also it is shown the fitted exponential $f^{CR}(MET)$ (line) and the extrapolation of this function into the region SR (squares).

Table 6.5. The numbers of events in PYTHIA and in ALPGEN samples with different jet multiplicities ($\geq$1jet, $\geq$ 2jets, and $\geq$3 jets) and for different E_T^{miss} regions ($\geq$ 200 GeV and 100$\rightarrow$200 GeV)

Number of Jets	Sample	E_T^{miss} $\geq$200 GeV	100$\leq$ E_T^{miss} $\leq$200 GeV
$\geq$1(no R-cuts)	PYTHIA	5025	651
$\geq$1(no R-cuts)	ALPGEN	5518	795
$\geq$2	PYTHIA	1264	242
$\geq$2	ALPGEN	1729	359
$\geq$3	PYTHIA	211	68
$\geq$3	ALPGEN	476	157

mated number of $Z \rightarrow \mu\mu$+jets events measured in the data. We define K to be $1 - \frac{N_\mu^{SR}}{N_\mu^{true}}$ (the ratio of the bias to correct number of events) and we determine it to be K=0.23.

6.6. Systematic Uncertainties

The systematic uncertainties on the estimated number of $Z \rightarrow \nu\nu$+jets events, N_ν, are mainly due to the statistical uncertainties on the factors entering Equation 6.5. The

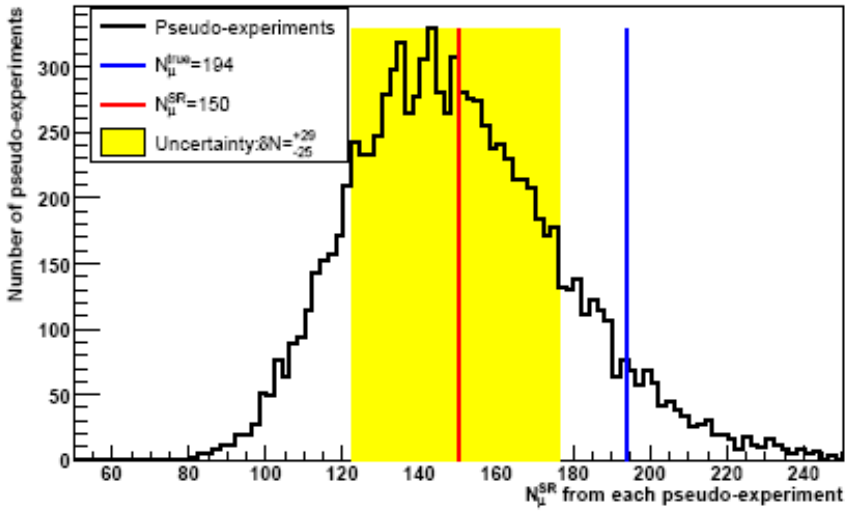


Figure 6.5. Estimation of number of $Z \rightarrow \mu\mu$+jets events passing the loose event selection from 10,000 pseudo-experiments (histo) corresponding to an integrated luminosity of 1 fb^{-1}. It is also shown the expectation (blue) from the $Z \rightarrow \mu\mu$+jets ALPGEN sample. The box (yellow) represents the uncertainty on the estimate (red).

theoretical absolute uncertainty on the ratio of the decay widths, $\Gamma(Z \rightarrow \nu\nu)/\Gamma(Z \rightarrow \mu\mu)$ is 0.03. The absolute statistical uncertainty on the Z boson identification efficiency, A_Z, is 0.003. The absolute statistical uncertainty on scale factor between the loose and full event selections, A_{SF}, is 0.034. Using the standard propagation of errors procedure, the combined effect of these uncertainties amounts to 10.5% of the estimated number of $Z \rightarrow \nu\nu$+jets events.

6.7. Result

We present in Figure 6.6 the final estimate of the number of $Z \rightarrow \mu\mu$+jets events, N_μ^{SR}, passing the loose event selection in the signal region SR, as a function of the integrated luminosity. For illustrative purposes, we choose an integrated luminosity of 500 pb^{-1} to quote the final estimation of invisible Z boson decay. At the given luminosity we estimate $N_\mu^{SR} = 97^{+27}_{-11}$. According to Equation 6.5 we estimate $N_\nu^{ES} = 547^{+151}_{-62}$ $Z \rightarrow \nu\nu$+jets events, where the uncertainty contains both statistical and systematic effects, passing the full event selection used in the search for SUSY.

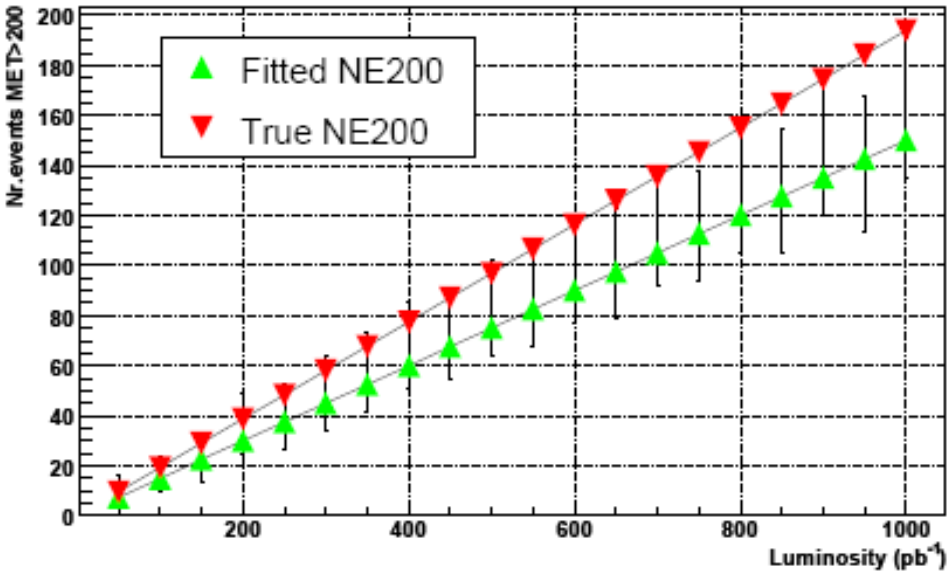


Figure 6.6. The estimated number of $Z \rightarrow \mu\mu$+jets events, N_{μ}^{SR}, passing the loose event selection in the signal rigion SR, as a function of the integrated luminosity.

7. CONCLUSION

The proton beams were injected to the LHC pipes and first events recorded in the detectors in the low center of mass energy. Reach to $\sqrt{s}$ =14 TeV center of mass energy will take some time but new era started for the particle physics. Many new physics theories were done with the MC studies. In order to understand the detector behavior test beam studies were done in various years. Most probably in a year real data will be available in high energies to compare with the results of the MC studies.

In this thesis presented studies were performed for the CMS experiment which was built on the LHC tunnel at CERN. In my thesis two subjects were studied.

In the first part, ECAL plus HCAL barrel energy response was compared with the result of the TB 2006 studies. Single pions were used for various energy ranges. CMS experiment uses GEometry ANd Tracking (GEANT) for simulation production. LHEP and QGSP are two main configurations of GEANT. LHEP and QGSP use different approaches to interactions of hadrons. A few percentage difference between MC and TB 2006 results was obtained. This discrepancy is coming from the simulation tools. The material between ECAL and HCAL may not simulate very well.

In the second part, SUSY discovery methods was explained for CMS experiment at $\sqrt{s}$ =14 TeV center of mass energy. SUSY theory will test with the MET and multijets events. If SUSY theory exists then LSPs do not interact with the detector material and SUSY particles will be seen as MET events. Multijets events are the result of the cascades of the SUSY and SM model particles. Some SM model particles also weakly interact with materials and they leave MET events in the detector. Hence, source of MET events must be well separated. For this purpose, some methods and cuts are defined by the analysis groups. These kind of cuts were used to reduce the background events which come from the SM events such as QCD and $t\bar{t}$ events. Signal significance is greater than 5 for QCD and $t\bar{t}$ events as backgrounds for SUSY search. Neutrinos and muons are weakly interacting particles and these particles leave MET like LSPs in the detectors. But muons can be detected in the CMS detector very well. Muons and neutrinos have the same kinematic properties and we can estimate MET events from neutrinos using the muons. Thus, MET events from neutrinos can be subtracted from the SUSY events for

SUSY estimation in the final state. Results of the analysis show that analysis methods can separate SUSY and SM events and if SUSY theory exists in TeV energy scale CMS experiment can discover the SUSY particles.

REFERENCES

ADAM, N., et al., Towards a measurement of the inclusive $W \rightarrow \mu\nu$ and $Z \rightarrow \mu^+\mu^-$ cross sections in pp collisions at $\sqrt{s}$=14 TeV, CMS-AN-2007/031.

ADAMS, T., 2008, "SUSY Searches at the Tevatron", arXiv:0808.0728v1.

AKCHURIN, N., et al., 2007, "The Response of CMS Combined Calorimeters to Single Hadrons, Electrons and Muons", CMS NOTE 2007/012.

ALVAREZ-GUAME, L., et al., 2004, Phys.Lett. B 592, 246.

AMAPANE, N., FIERRO, M., KONECKI, M., 2002, "High Level Trigger Algorithms for Muon Isolation", CMS NOTE 2002/040.

ANGELINI, L., et al.:2004, arXiv:0407214v2 [hep-ph]

BARGER, V. and PHILLIPS, R., 1987, Collider Physics, Addison-Wesley.

BELYAEV, A., 2004, "SUSY: Theory Status in the light of experimental constraints", arXiv:hep-ph/0410385v1.

BHATTI, A., LUNGU, G., TOPAKLI, H., "Determination of invisible Z boson+jets background to Hadronic SUSY search", CMS AN-2009/121.

BHATTI, A., et al., "Performance of the SISCone Jet Clustering Algorithm", CMS AN-2008/002.

BITYUKOV, S.I., and KRASNIKOV, N.V., 1998, Towards the Observation of Signal over Background in Future Experiments, arXiv:physics/9808016v1.

BOHR, N., 1913, "Philosophical Magazine", 26,1.

CHADWICK, C., 1932, Nature, 129, 312.

CMS HCAL COLLABORATIONS, "Design, Performance, and Calibration of CMS Hadron Endcap Calorimeters", CMS NOTE 2008/010.

CMS HCAL/ECAL COLLABORATIONS, "The CMS Barrel Calorimeter Response to Particle Beams from 2 to 350 GeV/c", CMS NOTE 2008/034.

DAWSON, S., 1997, "SUSY AND SUCH", arXiv:hep-ph/9612229v2.

DIRAC, P.A.M., 1927, Proc.R.Soc., London A114, 243, 710.

DITTMAR, M., 1999, "SUSY discovery strategies at the LHC", arXiv:hep-ex/9901004v1.

DREES, M., 1996, arXiv:hep-ph/9611409v1.

ESEN, S., LANDSBERG, G. et al., "Missing ET Performance in CMS", CMS AN-2007/041.

EVANS, L. and BRYANT, P., 2008, ”LHC Machine”, JINST 3 S08001.

FELCINI, M. 2008, for the CMS collaboration, The Trigger System of the CMS Experiment, CERN-CMS-CR-2008/030.

FERMI, E., 1934, Z.Phys.88, 161.

FEYNMAN, R.P., 1949, ”The Strange Theory of Light and Matter”, Princeton University Press, Princeton, New Jersey, 1985; ”Phys.Rev”. 76, p.749, 769.

FOLGER, G., et al., 2009, Progress in hadronic physics modeling in Geant4, Journal of Physics: Conference Series 160(2009) 012073.

GELL-MANN, M., 1964, Phys. Lett. 8, 214.

GLASHOW, S.L., 1961, Nucl.Phys., 22, 579.

GLASHOW, S.L., ILIOPOULOS, J. and MIANI, L., 1970, Phys.Rev.D 2, 1285.

GREEN, D., ”Calibrating the CMS Calorimeters Using 2004 Test Beam Data”.

HALZEN, F. and MARTIN, A., 1984, Quarks and Leptons: An Introductory Course in Modern Particle Physics, John Willey &Sons, Inc.

HOLLIK, W. 1998, plenary talk at the 29th International Conference on High-Energy Physics (ICHEP, 98), Vancouver, British Columbia, Canada, July, 23-30.

http://cms.web.cern.ch/cms/Detector/WhatCMS/index.html

http://www.geant4.org/geant4/support/proc_mod_catalog/physics_lists/referencePL.shtml

http://indico.cern.ch/materialDisplay.py?contribId=7&materialId=slides&confId=27417

http://indicobeta.cern.ch/conferenceDisplay.py?confId=39023

https://twiki.cern.ch/twiki/bin/view/CMS/WorkBook120JetAnalysis

KALINOWSKI, J. 2007, ”SUSY THEORY REVIEW”, ACTA PHYSICA POLONICA B.

KANE, G.L., 1983, Modern Elementary Particle Physics, Addison-Wesley.

KODOLOVA, O. et al. 2005, Jet Energy Correction with charged particle tracks in CMS, ”Eur Phys J C40,s02,33-42”.

KUMAR, A. 2005, ”Large P_T Processes in $p\bar{p}$ Collisions at 2 TeV”, PhD.Thesis.

LIU, C., NEUMEISTER, N. 2008, Reconstruction of Cosmic and Beam-Halo Muons, CMS NOTE-2008/01.

MARTIN, S.P. 2006, ”A Supersymmetry Premier”, hep-ph/9709356.

PERL, M.L., 2003, The Discovery of the Tau Lepton and the Changes in Elementary Particle Physics in 40 years, SLAC-PUB-10150.

PESKIN, M. and SCHROEDER, D., 1995, An Introduction to Quantum Field Theory, Westview Press.

PI, H., WUERTHWEIN, F., MNICH, J. 2006, Study of QCD background for W+jets with isolated lepton + jet + missing E_T signature, CMS IN-2006/108.

QUIGG, C., 1983, Gauge Theories of the Strong, Weak, and Electromagnetic Interactions, Addison-Wesley.

RUTHERFORD, E., 1911, "Philosophical Magazine", 21, 669.

SALAM, A., 1969, Elementary particle Theory, ed.N.Svartholm (Almquist and Wiksells, Stockholm) p.367.

SALAM, A. and WARD, J.C., 1964, Phys Lett 13, 168.

SHARMA, S., et al. 2009, "Prospect of SUSY Search in CMS Using the Jets+MET+ τ Channel", CMS AN-2009/043.

SMITH, W., 2008, Hadron Collider Physics Summer School at Fermilab, August 12-22.

SPIROPULU, M. 2008, SUSY@LHC.CERN.CH, arXiv:hep-ex/0801.0318v1.

SPIROPULU M., YETKIN, T. 2006, "Jet and Event Electromagnetic and Charged fraction in CMS", CMS IN-2006/010.

TATA, X. 1997, "What is Supersymmetry and how do we find it?",hep-ph/9706307 v1.

THE CMS COLLABORATION, 2006, CMS Physics Technical Design Report, Volume I, "CMS Detector Performance and Software CERN/LHCC 2006-001".

THE CMS COLLABORATION 2008, "The CMS experiment at the CERN LHC", JINST 3 S08004.

---------- , 2007, Nuclear and Particle Physics, "Journal of Physics G".

---------- , 1997, The CMS muon project, Technical Design Report, CERN-LHCC-97-032.

---------- , 2008, "Plans for Jet Energy Corrections at CMS", CMS PAS JME-07-002.

THE SUPER KAMIOKANDE COLLABORATION, 1998, Phys. Rev. Lett.81, 1562.

THOMSEN, J., "Search for Supersymmetric Particles based on large Missing Transverse Energy and High Pt Jets at the CMS Experiment", 2007.

THOMSON, J., 1897, "Philosophical Magazine", Vol.44, Series 5, 293.

TOPAKLI, H. 2009, "Determination of invisible Z boson+jets background to Hadronic SUSY search", CMS CR-2009/052.

_____ 2009, ”Determination of invisible Z boson+jets background to Hadronic SUSY search”, Balkan Physics Letters, volume 17.

UA1 COLLABORATION, 1983, Phys. Lett.B 122, 103.

_____ , 1983, Phys. Lett.B 126, 398.

UA2 COLLABORATION, 1983, Phys. Lett.B 122, 476.

_____ , 1983, Phys. Lett.B 129, 130.

WEINBERG, S., 1967, Phys. Lett. 19, 1264.

YAZGAN, E. 2007, PhD. Thesis, TS2007-011.

YETKIN, T. 2006, PhD. Thesis.

YUKAWA, Y., 1935, Proc. Phys. Math. Soc., Japan, 17, 48.

ZWEIG, G., 1964, CERN Report No.8182/TH401.

CURRICULUM VITAE

I was born on January 1, 1976, Mersin, Turkey. I finished my high school education in Mersin, 1993. I graduated from the Physics Department of Kocaeli University in 1999. I have worked in Gaziosmanpaşa University as a research assistant for one year. I got the MSc degree from the Çukurova University in 2003. I started my PhD studies in the field of high energy of particle physics in Çukurova University in 2003. I have been working as a research assistant in Çukurova University since 2003. I am married and have a son.